SEARCH FOR NEW STATES DECAYING INTO $J/\psi\pi^+\pi^-$ WITH THE ATLAS DETECTOR AT THE LARGE HADRON COLLIDER

by

Wei-Cheng Wong

| APPROVED BY SUPERVISORY COMMITTEE: |
|------------------------------------|
| |
| Xinchou Lou, Chair |
| |
| Robert Glosser |
| |
| John H. Hoffman |
| |
| Mustapha Ishak-Boushaki |
| |
| Kendall Reeves |

Copyright 2012

Wei-Cheng Wong

All Rights Reserved

SEARCH FOR NEW STATES DECAYING INTO $J/\psi\pi^+\pi^-$ WITH THE ATLAS DETECTOR AT THE LARGE HADRON COLLIDER

by

WEI-CHENG WONG, B.S., M.S.

DISSERTATION

Presented to the Faculty of
The University of Texas at Dallas
in Partial Fulfillment
of the Requirements
for the Degree of

DOCTOR OF PHILOSOPHY IN PHYSICS

THE UNIVERSITY OF TEXAS AT DALLAS

August 2012

ACKNOWLEDGMENTS

First and foremost, I would like to thank Dr. Xinchou Lou, my advisor and committee chair, for supporting my research. Dr. Lou guided me on the way to achieve the contribution at CERN and in all areas of my Ph.D. study. I would also like to thank the other members of my Ph.D. supervisory committee, Dr. Robert Glosser, Dr. John Hoffman, Dr. Mustapha Ishak-Boushaki, and Dr. Kendall Reeves for their time and effort in helping me finish the dissertation.

Secondly, I would like to thank Dr. Joseph M. Izen. During my studies at the High Energy Physics Group in The University of Texas at Dallas, Dr. Izen taught me a lot of knowledge of the experimental high energy physics, and always encouraged me on my studies.

I would like to thank Dr. Kendall Reeves once again, Dr. Mahsana Ahsan, and Harisankar Namasivayam, major members in the UTD High Energy Physics Group. During my recent studies, for more than three years, they helped me in many aspects to reach the goals efficiently. I would like to thank Marjorie D. Renfrow, who helped me into the big family of the Physics Department. She had made my life in Dallas much more enjoyable.

June 2012

SEARCH FOR NEW STATES DECAYING INTO $J/\psi\pi^+\pi^-$ WITH THE ATLAS DETECTOR

AT THE LARGE HADRON COLLIDER

Publication No. _

Wei-Cheng Wong, Ph.D The University of Texas at Dallas, 2012

Supervising Professor: Xinchou Lou

study.

Using pp collision data collected at $\sqrt{s} = 7$ TeV in 2010 and 2011 with the ATLAS detector (A Toroidal LHC ApparatuS), corresponding to an integrated luminosity of 2.44 fb⁻¹, the $J/\psi\pi^+\pi^$ combinations have been studied. The selection criteria have been developed, the detection efficiency of the $X_c(3872)$ signal has been evaluated, and the systematic errors have been identified. Both the $\psi(2S)$ and the $X_c(3872)$ signals are observed in the $J/\psi\pi^+\pi^-$ mass spectrum. The detection of the charmonium-like X, Y, Z states is feasible with the ATLAS detector at the Large Hadron Collider (LHC). Other than the $\psi(2S)$ and the $X_c(3872)$ signals, there is no evidence for any significant enhancement in the $I/\psi \pi^+\pi^-$ mass spectrum. This dissertation research establishes that ATLAS can detect $X_c(3872)$ like new particles in the $J/\psi \pi^+\pi^-$ final state, and with current data sample, no new states have been observed in this

 \mathbf{v}

TABLE OF CONTENTS

| ACKNOWLE | EDGMENTS | iv |
|-------------|--|----|
| ABSTRACT | | V |
| LIST OF TA | BLES | ix |
| LIST OF FIG | GURES | xi |
| CHAPTER 1 | INTRODUCTION | 1 |
| 1.1 | The Standard Model of Elementary Particle Physics | 1 |
| 1.2 | The Quark Model of Mesons and Baryons | 5 |
| 1.3 | The <i>X</i> , <i>Y</i> , <i>Z</i> States Discovered at the <i>B</i> Factories and at the Tevatron | 7 |
| CHAPTER 2 | CHARMONIA AND THEIR PRODUCTION AT HADRON COLLIDERS | 12 |
| 2.1 | Production of Charmonia at the Tevatron | 12 |
| 2.2 | Production of Charmonia at the Large Hadron Collider | 15 |
| 2.3 | The PYTHIA Predictions and the Cross-Sections of $pp \rightarrow ggX$ | 17 |
| 2.4 | Search for New Charmonium-like States | 20 |
| CHAPTER 3 | EXPERIMENTAL APPARATUS | 23 |
| 3.1 | The Large Hadron Collider | 23 |
| 3.2 | The ATLAS Detector | 25 |
| | 3.2.1 Overview | 25 |
| | 3.2.2 The Coordinate System | 26 |
| | 3.2.3 The Central Tracking System | 27 |

| | 3.2.4 The Magnet System |
|-----------|---|
| | 3.2.5 The Calorimeters |
| | 3.2.6 The Muon Spectrometers |
| 3.3 | The ATLAS Trigger and Data Acquisition Systems |
| | 3.3.1 The Level 1 Trigger |
| | 3.3.2 The Level 2 Trigger |
| | 3.3.3 The Event Filter |
| CHAPTER 4 | OFFLINE EVENT RECONSTRUCTION AND OBJECT IDENTIFICATION41 |
| 4.1 | The ATLAS Offline Computing System and Data Storage41 |
| 4.2 | Event Reconstruction |
| 4.3 | Track Measurement and Primary Vertex Reconstruction |
| 4.4 | Muon Reconstruction and Identification48 |
| CHAPTER 5 | MONTE CARLO SIMULATION PRODUCTION49 |
| 5.1 | Monte Carlo Simulation |
| 5.2 | The PYTHA Program and Event Generation50 |
| 5.3 | The Generator Filters and the Usage of the CKIN(3) Variable55 |
| 5.4 | Monte Carlo Samples |
| CHAPTER 6 | ANALYSIS METHODS AND USER PROGRAM |
| 6.1 | The Athena Framework and Data Analysis Packages59 |
| 6.2 | Reconstruction of the $X_c(m) \to J/\psi \pi^+ \pi^-$ Events |
| 6.3 | Background Suppression67 |
| CHAPTER 7 | MONTE CARLO STUDY OF $X_c(3872)$ EVENTS69 |

| | 7.1 | Event Generation and Filter Efficiency | .69 |
|------|--------|---|-----|
| | 7.2 | Event Selection | 73 |
| | 7.3 | Mass Spectra of Simulated $J/\psi\pi^+\pi^-$ Events | 86 |
| | 7.4 | Transverse Momenta | 88 |
| | 7.5 | Reconstruction Efficiencies | 92 |
| СНАР | TER 8 | DATA SAMPLE, DATA ANALYSIS, AND RERULTS | 98 |
| | 8.1 | Data Sample | 98 |
| | 8.2 | Mass Spectrum of $J/\psi \pi^+\pi^-$ Combinations | 102 |
| | 8.3 | Systematic Uncertainty | 105 |
| СНАР | TER 9 | CONCLUSIONS AND OUTLOOK | 121 |
| | 9.1 | Conclusions | 121 |
| | 9.2 | Outlook | 122 |
| APPE | NDIX 1 | PYTHIA JOB FILE FOR GENERATING $X_c(3872)$ EVENTS | 124 |
| APPE | NDIX 2 | PYTHIAB JOB FILE FOR GENERATING $B^+ \to X_c(3872)K^+$ EVENTS | 126 |
| APPE | NDIX 3 | JOB OPTION CODE FOR ANALYZING $J/\psi\pi^+\pi^-$ EVENTS | 128 |
| APPE | NDIX 4 | THE ROOT MACRO OF FITTING $J/\psi\pi^+\pi^-$ MASS | 133 |
| REFE | RENCE | ES | 136 |
| VITA | | | |

LIST OF TABLES

| 1.1 | Leptons (Spin 1/2). |
|-----|---|
| 1.2 | Quarks (Spin 1/2). |
| 1.3 | Mediators |
| 2.1 | List of charmonium states. The column (n ^{2S+1} L _J) lists the standard spectroscopic notation of principal quantum number and angular momenta. The column I ^G (J ^{PC}) lists the values of isospin, G-parity, spin, parity and charge conjugation. |
| 2.2 | Predicted cross-sections for various prompt vector quarkonium state production and decay into muons, with di-muon trigger thresholds $\mu 4\mu 4$ and $\mu 6\mu 4$ and the single muon trigger threshold $\mu 10$ (before trigger and reconstruction efficiencies). The last column shows the overlap between the di-muon m6m4 and single muon samples. The 'single' muon sample also requires that the second muon have a $p_T > 0.5$ GeV/c. |
| 2.3 | Predicted cross-sections for various muon and di-muon sources |
| 3.1 | Parameters of the Inner Detector |
| 3.2 | Expected track-parameter resolutions (RMS) at infinite transverse momentum, σ_X (∞), and transverse momentum, p_X , at which the multiple-scattering contribution equals that from the detector resolution. |
| 3.3 | Example of LVL1 trigger menu ($L = 10^{34} \text{ cm}^{-2} \text{s}^{-1}$) |
| 5.1 | Charmonium production subprocesses introduced in the PYTHIA, and their corresponding ISUB subprocess numbers |
| 5.2 | New MSEL subprocess menus available in the PYTHIA53 |
| 5.3 | Color-singlet/octet production subprocesses in the PYTHIA 6.403, and their corresponding ISUB subprocess numbers |
| 5.4 | Signal samples of ATLAS Monte Carlo events |
| 5.5 | Background samples of ATLAS Monte Carlo events |

| 6.1 | Codes list of accessing truth particles |
|-----|--|
| 7.1 | Number of events and filter efficiencies of the direct $pp \to X_c(3872)$ event generation70 |
| 7.2 | Number of events and filter efficiencies of the $B^+ \to X_c(3872)K^+$ event generation72 |
| 7.3 | List of events and the efficiencies passing the event selections |
| 7.4 | Summary of Monte Carlo study of the $X_c(3872) \rightarrow J/\psi \pi^+ \pi^-$ 86 |
| 8.1 | (Preliminary) Luminosities by periods, calculated with trigger EF_2mu4_Jpsimumu100 |
| 8.2 | (Preliminary) Summary of the $X_c(3872) \rightarrow J/\psi \pi^+ \pi^-$ |
| 8.3 | (Preliminary) Sources of systematic errors |
| 8.4 | (Preliminary) Summary of Monte Carlo study of $X_c(3872)$ detection efficiencies109 |
| 8.5 | (Preliminary) $X_c(3872)$ yields with mass resolution fixed at 12.0 MeV/ c^2 in the fit111 |
| 8.6 | (Preliminary) $X_c(3872)$ yields with mass resolution fixed at 10.6 MeV/ c^2 in the fit111 |
| 8.7 | (Preliminary) X_c (3872) yields with mass resolution fixed at 13.4 MeV/ c^2 in the fit111 |
| 8.8 | (Preliminary) Data $\psi(2S)$ yields, by periods, obtained from fits to $J/\psi\pi^+\pi^-$ mass distributions. |
| 8.9 | (Preliminary) Data $X_c(3872)$ yields, by periods, obtained from fits to $J/\psi\pi^+\pi^-$ mass distributions |

LIST OF FIGURES

| 1.1 | Mesons $(Q\bar{Q} \text{ states})$ 6 |
|-----|---|
| 1.2 | Baryons (QQQ states)6 |
| 1.3 | New resonances compared to the $c\bar{c}$ spectroscopy predicted by potential model. The horizontal axis is labeled with the J^{PC} quantum states, where J the total angular momentum, P the parity, and C the charge conjugation. (R. Mussa. Morriond QCD 2008) |
| 1.4 | The $X_c(3872)$ resonance $(J/\psi\pi^+\pi^-)$, and its comparison with $D^0\bar{D}^{*0}$ threshold9 |
| 1.5 | The $Y_c(4260)$ resonance state |
| 1.6 | The $Z_c^+(4433)$ resonance state |
| 2.1 | Differential cross-section of J/ψ production at the Tevatron with theoretical predictions for color-singlet and color-octet model production |
| 2.2 | Inclusive J/ψ production cross-section as a function of J/ψ transverse momentum in the four rapidity bins. Overlaid is a band representing the variation of the result under various spin-alignment scenarios representing a theoretical uncertainty. The equivalent results from CMS are overlaid. The luminosity uncertainty (3.4%) is not shown |
| 2.3 | The predictions for prompt J/ψ direct production at the LHC according to the color-octet model implemented in PYTHIA for the CTEQ PDF. Dotted line: CSM; dashed line: ${}^{1}S_{0}^{(8)} + {}^{3}P_{J}^{(8)}$ contributions; dot-dash line: ${}^{1}S_{1}^{(8)}$ contribution; solid line: all contributions. Notice that asymptotically the ${}^{1}S_{1}^{(8)}$ contribution becomes dominant, likely implying a transverse polarization of charmonium at high p_{T} . |
| 2.4 | Density of the J/ψ production cross-section as a function of the hardest and softer muon p_T of muons coming from the J/ψ . No cut was placed on the generated sample, but the overlaid lines represent the thresholds of observed events with trigger cuts applied18 |
| 2.5 | Combined plots of differential and integrated muon p_T spectra showing hardest muon rates for $bb \to \mu 6X$, $bb \to \mu 6\mu 4X$, $bb \to J/\psi(\mu 6\mu 4)X$, $cc \to \mu 6X$, direct J/ψ , and direct \Box processes (no charge correlation) |

| 2.6 | Combined plots of differential and integrated muon p_T spectra showing rates of the second hardest muon in event for $bb \rightarrow \mu 6\mu 4X$, $bb \rightarrow J/\psi(\mu 6\mu 4)X$, $cc \rightarrow \mu 6X$, direct J/ψ , and direct \Box processes (no charge correlation) |
|-----|--|
| 2.7 | $J/\psi \pi^+ \pi^-$ mass distribution measured by the LHCb experiment |
| 2.8 | $J/\psi \pi^+\pi^-$ mass distribution measured by the CMS experiment |
| 3.1 | The overall view of the LHC |
| 3.2 | The overall view of the ATLAS Detector |
| 3.3 | (Left) Cut-away view of the Inner Detector. (Right) Structural components traversed by a charged particle passing through the barrel region of the Inner Detector |
| 3.4 | Cross-section of one quadrant of the Inner Detector |
| 3.5 | The ATLAS Magnet System |
| 3.6 | The LAr Calorimeters and the Tile Calorimeters |
| 3.7 | The Muon Spectrometers |
| 3.8 | Schematic representation of the ATLAS Trigger System |
| 3.9 | The event rates and processing times of the ATLAS trigger system |
| 4.1 | The ATLAS computing model |
| 4.2 | The Grid computing system in the ATLAS |
| 4.3 | The reconstruction processing pipeline |
| 4.4 | Tracking reconstruction chain. The boxes on the top represent data object, whilst the boxed on the bottom show the algorithms which work on them. The arrows show the direction of data flow |
| 5.1 | Flow-Chart of the ATLAS Full Chain Monte Carlo Simulation and data analysis. Main data formats are shown as ovals, computing/conversion steps shown as rectangles |
| 5.2 | PYTHIA job file for generating direct $X_c(3872)$ events |
| 5.3 | Partial PYTHIA job file for generating the $X_c(3872)$ events from the B^+ decay |

| 5.4 | Example PYTHIA codes for applying kinematics cuts |
|------|--|
| 6.1 | The Athena component model |
| 6.2 | Analysis codes for finding Monte Carlo truths in the $X_c(m)$ events |
| 7.1 | Log record of the direct $pp \to X_c(3872)$ event generation (1 st sub-job)70 |
| 7.2 | Log record of the $B^+ \to X_c(3872)K^+$ event generation (1 st sub-job) |
| 7.3 | Mass distributions of $J/\psi \to \mu^+\mu^-$ events. (a) The direct $pp \to X_c(3872)$ sample. (b) The $B^+ \to X_c(3872)K^+$ sample73 |
| 7.4 | (a) The muon p_T distribution, and the p_T cut at 4.0 GeV/c. (b) The mass distribution of $J/\psi \to \mu^+\mu^-$ events of the direct $pp \to X_c(3872)$ sample74 |
| 7.5 | (a) The muon p_T distribution, and the p_T cut at 4.0 GeV/c. (b) The mass distribution of $J/\psi \to \mu^+\mu^-$ events of the $B^+ \to X_c(3872)K^+$ sample74 |
| 7.6 | (a) Number of pixel hits distribution of muon tracks, (b) number of SCT hits distribution of muon tracks, (c) mass distribution of $J/\psi \to \mu^+\mu^-$ of the direct $pp \to X_c(3872)$ sample75 |
| 7.7 | (a) Number of pixel hits distribution of muon tracks, (b) number of SCT hits distribution of muon tracks, (c) mass distribution of $J/\psi \to \mu^+\mu^-$ of the $B^+ \to X_c(3872)K^+$ sample75 |
| 7.8 | Invariant mass distributions of $J/\psi \to \mu^+\mu^-$ of (a) the direct $pp \to X_c(3872)$ sample, and (b) the $B^+ \to X_c(3872)K^+$ sample76 |
| 7.9 | The four-track invariant mass distribution of $J/\psi\pi^+\pi^-$. (a) The direct $pp \to X_c(3872)$ sample. (b) The $B^+ \to X_c(3872)K^+$ sample78 |
| 7.10 | Simulated invariant mass distributions of $X_c(3872) \rightarrow J/\psi \pi^+ \pi^-$ of (a) the direct $pp \rightarrow X_c(3872)$ sample, and (b) the $B^+ \rightarrow X_c(3872)K^+$ sample |
| 7.11 | (a) Pion track p_T distribution, and the cut at 0.6 GeV/c. (b) The mass distribution of $X_c(3872) \rightarrow J/\psi \pi^+ \pi^-$ of the direct $pp \rightarrow X_c(3872)$ sample |
| 7.12 | 2(a) Pion track p_T distribution, and the cut at 0.6 GeV/c. (b) The mass distribution of $X_c(3872) \rightarrow J/\psi \pi^+ \pi^-$ of the $B^+ \rightarrow X_c(3872) K^+$ sample |

| pio | Number of pixel hits distribution of pion tracks, (b) number of SCT hits distribution of n tracks, (c) mass distribution of $X_c(3872) \rightarrow J/\psi \pi^+ \pi^-$ of the direct $pp \rightarrow X_c(3872)$ apple |
|--------------|---|
| pio | Number of pixel hits distribution of pion tracks, (b) number of SCT hits distribution of tracks, (c) mass distribution of $X_c(3872) \rightarrow J/\psi \pi^+\pi^-$ of the $B^+ \rightarrow X_c(3872)K^+$ apple |
| 7.15 An | alysis codes for fitting the vertex of the $X_c(m) \to J/\psi \pi^+ \pi^-$ events |
| | ass distributions of $X_c(3872) \rightarrow J/\psi \pi^+ \pi^-$. (a) The direct $pp \rightarrow X_c(3872)$ sample. (b) $e^+ B^+ \rightarrow X_c(3872)K^+$ sample |
| (Me | Mass distribution of $X_c(3872) \rightarrow J/\psi \pi^+ \pi^-$ before vertex fitting. ($\sigma_{\text{no-fit}} = 48.6 \pm 1.8 \text{ eV/c}^2$)). (b) Mass distribution of $X_c(3872) \rightarrow J/\psi \pi^+ \pi^-$ after vertex fitting. ($\sigma_{\text{fit}} = 12.8 \pm (\text{MeV/c}^2)$) of the direct $pp \rightarrow X_c(3872)$ sample |
| (Me | Mass distribution of $X_c(3872) \rightarrow J/\psi \pi^+ \pi^-$ before vertex fitting. $(\sigma_{\text{no-fit}} = 48.6 \pm 2.3 \text{ eV/c}^2)$). (b) Mass distribution of $X_c(3872) \rightarrow J/\psi \pi^+ \pi^-$ after vertex fitting. $(\sigma_{\text{fit}} = 12.7 \pm (\text{MeV/c}^2))$ of the direct $pp \rightarrow X_c(3872)$ sample |
| | Prob(χ^2) distribution of $\mu^+\mu^-\pi^+\pi^-$ combination, (b) mass distributions of $X_c(3872) \rightarrow b\pi^+\pi^-$ of the direct $pp \rightarrow X_c(3872)$ sample. |
| | Prob(χ^2) distribution of $\mu^+\mu^-\pi^+\pi^-$ combination, (b) mass distributions of $X_c(3872) = b\pi^+\pi^-$ of the $B^+ \to X_c(3872)K^+$ sample. |
| $7.21 \ X_c$ | $(3872) \rightarrow J/\psi \pi^+ \pi^-$ mass distribution of the direct $pp \rightarrow X_c(3872)$ sample |
| $7.22 X_c$ | $(3872) \rightarrow J/\psi \pi^+ \pi^-$ mass distribution of the $B^+ \rightarrow X_c(3872)K^+$ sample |
| $7.23 X_c$ | $(3872) \rightarrow J/\psi \pi^+ \pi^-$ mass distribution of combined samples |
| 7.24 Tra | ansverse momentum distribution of muons of the direct $pp \to X_c(3872)$ sample89 |
| 7.25 Tra | ansverse momentum distribution of pions of the direct $pp \to X_c(3872)$ sample89 |
| 7.26 Tra | ansverse momentum distribution of the J/ψ of the direct $pp \to X_c(3872)$ sample89 |
| 7.27 Tra | ansverse momentum distribution of the $X_c(3872)$ of the direct $pp \to X_c(3872)$ sample90 |
| 7.28 Tra | ansverse momentum distribution of muons of the $B^+ \to X_c(3872)K^+$ sample90 |

| 7.29 | Transverse momentum distribution of pions of the $B^+ \to X_c(3872)K^+$ sample91 |
|------|---|
| 7.30 | Transverse momentum distribution of the J/ψ of the $B^+ \to X_c(3872)K^+$ sample91 |
| 7.31 | Transverse momentum distribution of the $X_c(3872)$ of the $B^+ \to X_c(3872)K^+$ sample91 |
| 7.32 | Reconstruction efficiency of muons of the direct $pp \to X_c(3872)$ sample. (a) reconstruction efficiency vs. muon p_T , (b) muon p_T distribution, (c) reconstruction efficiency vs. muon η , (d) muon η distribution |
| 7.33 | Reconstruction efficiency of pions of the direct $pp \to X_c(3872)$ sample. (a) reconstruction efficiency vs. pion p_T , (b) pion p_T distribution, (c) reconstruction efficiency vs. pion η , (d) pion η distribution |
| | Reconstruction efficiency of the J/ψ of the direct $pp \to X_c(3872)$ sample. (a) reconstruction efficiency vs. J/ψ p _T , (b) J/ψ p _T distribution, (c) reconstruction efficiency vs. J/ψ η, (d) J/ψ η distribution |
| 7.35 | Reconstruction efficiency of the $X_c(3872)$ of the direct $pp \to X_c(3872)$ sample. (a) reconstruction efficiency vs. $X_c(3872)$ p _T , (b) $X_c(3872)$ p _T distribution, (c) reconstruction efficiency vs. $X_c(3872)$ η, (d) $X_c(3872)$ η distribution |
| 7.36 | Reconstruction efficiency of muons of the $B^+ \to X_c(3872)K^+$ sample. (a) reconstruction efficiency vs. muon p_T , (b) muon p_T distribution, (c) reconstruction efficiency vs. muon η , (d) muon η distribution96 |
| 7.37 | Reconstruction efficiency of pions of the $B^+ \to X_c(3872)K^+$ sample. (a) reconstruction efficiency vs. pion p_T , (b) pion p_T distribution, (c) reconstruction efficiency vs. pion η , (d) pion η distribution |
| | Reconstruction efficiency of the J/ψ of the in $B^+ \to X_c(3872)K^+$ sample. (a) reconstruction efficiency vs. J/ψ p _T , (b) J/ψ p _T distribution, (c) reconstruction efficiency vs. J/ψ η, (d) J/ψ η distribution |
| 7.39 | Reconstruction efficiency of the $X_c(3872)$ of the $B^+ \to X_c(3872)K^+$ sample. (a) reconstruction efficiency vs. $X_c(3872)$ p _T , (b) $X_c(3872)$ p _T distribution, (c) reconstruction efficiency vs. $X_c(3872)$ η, (d) $X_c(3872)$ η distribution |
| 8.1 | (Preliminary) Inclusive $J/\psi \pi^+\pi^-$ mass distribution |
| 8.2 | (Preliminary) Raw yield distribution of the fitted $X_c(3872)$ vs. p_T |

| 8.3 | (Preliminary) Reconstruction efficiencies of the $X_c(3872)$ vs. p_T , of the combined Monte Carlo sample. (a) Without the N_{fit} / N_D correction. (b) With the N_{fit} / N_D correction110 |
|------|---|
| 8.4 | (Preliminary) Mass distributions of $J/\psi\pi^+\pi^-$, fitted with a single Gaussian signal, the mass mean values fixed at 3,872.0 MeV/c ² with resolution 12.0 MeV/c ² , in p _T intervals112 |
| 8.5 | (Preliminary) Mass distributions of $J/\psi \pi^+\pi^-$, fitted with a single Gaussian signal, the mass mean values fixed at 3,872.0 MeV/c ² with resolution 10.6 MeV/c ² , in p _T intervals113 |
| 8.6 | (Preliminary) Mass distributions of $J/\psi \pi^+\pi^-$, fitted with a single Gaussian signal, the mass mean values fixed at 3,872.0 MeV/c ² with resolution 13.4 MeV/c ² , in p _T intervals114 |
| 8.7 | (Preliminary) $J/\psi\pi^+\pi^-$ mass distribution with fitting the $\psi(2S)$ mass |
| 8.8 | (Preliminary) Data $\psi(2S)$ yields per 1fb ⁻¹ for each period |
| 8.9 | (Preliminary) $J/\psi \pi^+ \pi^-$ mass distribution with fitting the $X_c(3872)$ mass |
| 8.10 | (Preliminary) Data $X_c(3872)$ yields per 1fb ⁻¹ for each period |
| 9.1 | LHC Schedule Assumptions |

CHAPTER 1

INTRODUCTION

1.1 The Standard Model of Elementary Particle Physics

The Standard Model is the central paradigm for high energy physics and the fundamental basis for all of physics. It conceptualizes objects as being fundamentally composed of leptons and quarks. The interactions of leptons and quarks are described by the exchange of mediators, called bosons.

The constituents of the Standard Model are classified as leptons, quarks, and mediators. The leptons and quarks have spin 1/2 and are called fermions, which are particles with half-integral spins (1/2, 3/2, ...). They obey Fermi-Dirac statistics. On the other hand, the mediators are called bosons which are particles with integral spins (0, 1, 2, ...). They obey the Bose-Einstein statistics. In addition, there is an antiparticle corresponding to every fundamental particle.

Six leptons, listed in Table 1.1, are arranged in three families of doublets. The leptons are electron (e), electron neutrino (v_e), muon (μ), muon neutrino (v_μ), tau (τ), and tau neutrino (v_τ). The electron, muon, and tau have a charge of -1 e (+1.6 × 10⁻¹⁹C) and react to the electromagnetic force, weak force, and gravitation. The electron neutrino (v_e), muon neutrino (v_μ), and tau neutrino (v_τ) are all charge neutral and only react to gravitation and the weak force. The

absence of the decay $\mu \to e\gamma$ serves as an experimental base for a family identity called lepton number and its conservation. Each lepton carries a lepton number of 1 specific to its family that is conserved in all interactions. Each lepton has an associated antiparticle with an opposite charge and lepton number. Leptons are point like particles with no internal structures, in other words, without radius.

Table 1.1. Leptons (Spin 1/2) [1].

| | Particle | Charge (e) | Mass (MeV/C ²) | Lifetime (Second) | Principal Decays | Electron Number (L _e) | $\begin{array}{c} Muon \\ Number \\ (L_{\mu}) \end{array}$ | $\begin{array}{c} \text{Tau} \\ \text{Number} \\ (L_{\tau}) \end{array}$ |
|------------|---------------|------------|-------------------------------|------------------------|---|---|--|--|
| First | e | -1 | 0.511 | ∞ (Stable) | N/A | 1 | 0 | 0 |
| Generation | $\nu_{\rm e}$ | 0 | < 3 × 10 ⁻⁶ | 8 | N/A | 1 | 0 | 0 |
| Second | μ | -1 | 105.66 | 2.197×10^{-6} | $ev_{\mu}(v_e)$ | 0 | 1 | 0 |
| Generation | $ u_{\mu}$ | 0 | < 0.19 | 8 | N/A | 0 | 1 | 0 |
| Third | τ | -1 | 1777.0 | 3.3×10^{-13} | $\mu \nu_{\tau}(\nu_{\mu})$, $e \nu_{\tau}(\nu_{e})$, $\rho \nu_{\tau}$ | 0 | 0 | 1 |
| Generation | ν_{τ} | 0 | < 18.2 | ∞ | N/A | 0 | 0 | 1 |

The muon (μ) and tau (τ) are heavier unstable versions of the electron. Muon (μ) was discovered as a component of cosmic radiation in 1937. Muons are the decay products of short-lived mesons, which are integral-spin particles produced in the upper atmosphere by primary cosmic ray protons from space. The tau lepton (τ) was first observed in an accelerator experiment in 1975. These three 'flavors' of charged lepton, electron, muon, and tau, are paralleled by three flavors of neutral lepton (neutrino). The upper limits to the neutrino masses are all small in comparison with those of the corresponding charged leptons, with which they are produced in partnership in weak interactions.

Table 1.2. Quarks (Spin 1/2) [1].

| | Particle | Charge (e) | Mass (MeV/C ²) | Baryon Number (B) | Down (D) | Up (U) | Strangeness (S) | Charm (C) | Bottom (B) | Top (T) |
|------------|----------|---------------|-------------------------------|-------------------------|-------------|-----------|-----------------|--------------|------------|------------|
| First | d | -1/3 | 5 to 8.5 | 1/3 | -1 | 0 | 0 | 0 | 0 | 0 |
| Generation | u | 2/3 | 1.5 to 4.5 | 1/3 | 0 | +1 | 0 | 0 | 0 | 0 |
| Second | S | -1/3 | 80 to 155 | 1/3 | 0 | 0 | -1 | 0 | 0 | 0 |
| Generation | С | 2/3 | 1000 to 1400 | 1/3 | 0 | 0 | 0 | +1 | 0 | 0 |
| Third | b | -1/3 | 4000 to 4500 | 1/3 | 0 | 0 | 0 | 0 | -1 | 0 |
| Generation | t | 2/3 | 174,300 ± | 1/3 | 0 | 0 | 0 | 0 | 0 | +1 |
| | | | 5100 | | | | | | | |

Referring to Table 1.2, the names of the quark types are up, down, strange, charm, bottom, and top. The first letter of these names symbolizes the quarks, such as u and d quarks. A bar over the quark symbol denotes an antiquark (\bar{u} , \bar{d} , etc). They fall into doublets called families. The up, charm, and top quarks have an electric charge of 2/3 e (+1.6 × 10⁻¹⁹C). The down, strange, and bottom quarks have an electric charge of -1/3 e (+1.6 × 10⁻¹⁹C). Each quark carries a baryon number of 1/3, a cumulative quantum number that is conserved in all interactions. Quarks react to all four fundamental interactions.

Quarks do not exist as free particles and thus the definition of mass is somewhat arbitrary, as it must depend on the magnitude of the potential binding of the quarks together in, for example, a proton. The effective mass of quarks in baryons and in mesons may be different. They have to be observed in baryons states or in mesons states to be measured or defined.

Two types of quark combinations are established as existing in nature. First, every baryon is composed of three quarks, and every antibaryon is composed of three antiquarks. (Baryon = QQQ, Antibaryon = $\bar{Q}\bar{Q}\bar{Q}$) Second, every meson is composed of a quark and an antiquark. (Meson = $Q\bar{Q}$) [2].

These strongly interacting quark composites are collectively referred to as hadrons. As we shall see, the fact that two, and only two, types of quark combination occur are successfully accounted for in the theory of interquark forces, called quantum chromodynamics (QCD).

Table 1.3. Mediators [1].

| Interaction | | Mediator | Charge (e) | Mass | Spin |
|-------------|-----------------|--------------------|------------|--------------------------------------|------|
| Strong | | Gluon, G | 0 | 0 | 1 |
| Electroweak | Electromagnetic | Photon γ | 0 | $< 2 \times 10^{-16} \text{ eV/C}^2$ | 1 |
| | Weak | \mathbf{W}^{\pm} | ± 1 | $80.423 \pm 0.039 \text{ GeV/C}^2$ | 1 |
| | | Z^0 | 0 | $91.1876 \pm 0.0021 \text{ GeV/C}^2$ | 1 |
| Gravity | | Graviton, g | 0 | 0 | 2 |

In quantum field theory, interactions between particles are carried out by the exchange of field quanta known as bosons. There are four known fundamental interactions between matters: gravitational, electromagnetic, strong, and weak, listed in Table 1.3. Each of these interactions has its own intermediate field bosons. The gravitational force is thought to be carried by the graviton, which acts on objects with mass or energy. The electromagnetic force results from the interchange of an intermediate photon. It only acts between particles with electrical charge or other photons. The strong force is carried by the gluon, which has a color charge resembling the electric charge of the electron. There are three color states named after the primary colors red (r), blue (b), and green (g), with opposite charge like state of antired (\bar{r}) , antiblue (\bar{b}) , and antigreen (\bar{g}) . The strong interaction is confined to small distance $\sim 10^{-15}$ m in nature [2].

The weak force is felt at distances $< 10^{-15}$ m. It is transmitted by massive particles known as the W^+ , the W^- , and the Z^0 bosons. The weak force is a quark identity or flavor changing interaction. Some examples of decays of subatomic particles due to the weak force are the neutron beta decay, or the muon decay.

1.2 The Quark Model of Mesons and Baryons

Hadrons are composite particles made of quarks in a colorless state, or white color state. A hadron can be either a baryon or a meson. Baryons, illustrated in Figure 1.2, are formed from three quarks each with one color charge of red, blue, or green. This mixture of primary color-like charges results in an overall color1ess (white) baryon. Mesons, illustrated in Figure 1.1, are composed of quarks and antiquarks of opposite colors such as red and antired again forming a colorless state. If single free quarks were found in nature, they would have an observable color charge. As a result of there being no color charge observed it is interpreted that single free quarks cannot be found in nature but only in combination with other quarks.

The color force, unlike the electromagnetic or gravity, does not decrease with distance. Rather the color potential increases with distance. As quark pairs are separated the increasing potential energy creates an additional quark pair. This occurs when the potential exceeds the rest mass of a quark antiquark pair. Applying more energy to separate a quark antiquark pair only creates more quark antiquark pairs. These quark pairs, following their creation, go into the formation of additional hadrons. This application of more energy produces jets of hadrons produced in e^+e^- or p^+p^- collisions. Because of this increasing color potential applying more energy to separate and isolate free quarks cannot be succeeded.

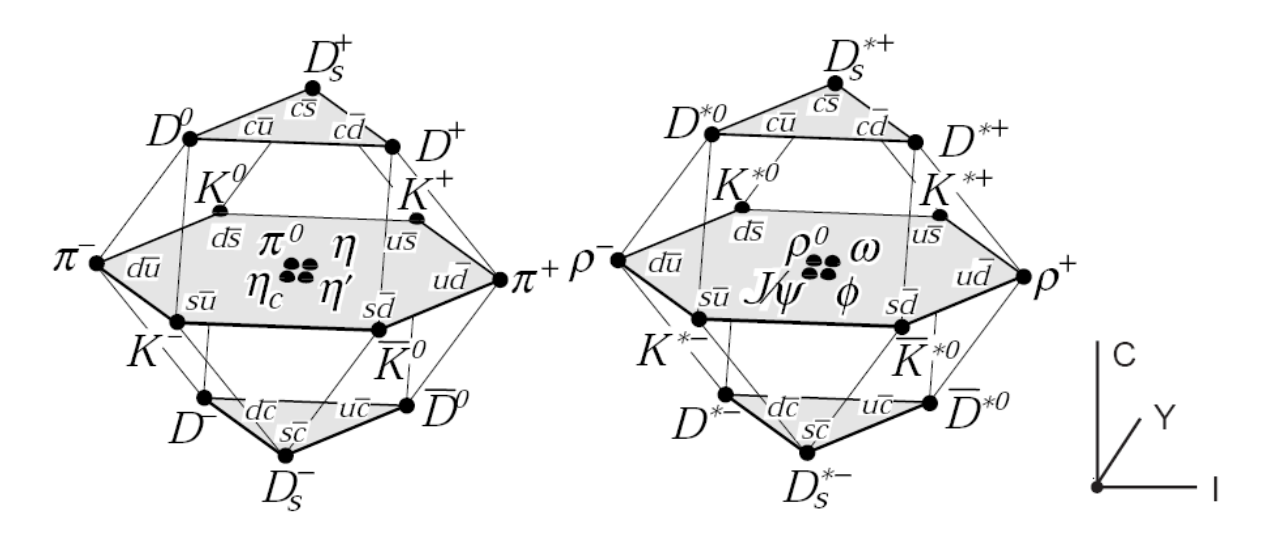


Figure 1.1. Mesons ($Q\bar{Q}$ states) [3].

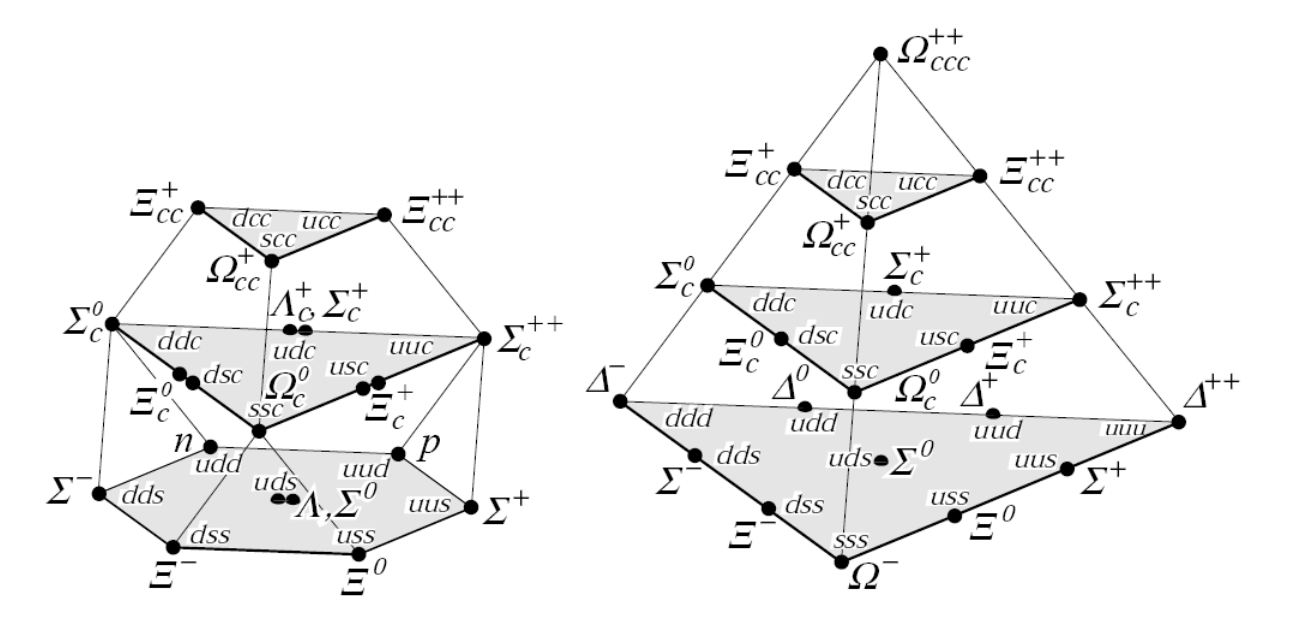


Figure 1.2. Baryons (QQQ states) [3].

1.3 The *X*, *Y*, *Z* States Discovered at the *B* Factories and at the Tevatron

The *B* factories -- the BaBar experiment at the Stanford Linear Accelerator Center (SLAC) in California and the Belle experiment at the High Energy Accelerator Research Organization (Kō Enerugī Kasokuki Kenkyū Kikō, KEK) in Japan -- produce *B* mesons and their decay products for physicists to study. The spectrum of quarkonia states, charmonia and bottomonia, were well-explained by the theoretical standard model of mesons and baryons. Since 2003, these experiments have discovered new states that do not fit into the original quark model [4]. The abnormal states were also confirmed by the CLEO detector at the Cornell Electron Storage Ring (CESR), the DØ experiment and the CDF (Collider Detector at Fermilab) detector at the Tevatron. The puzzle of the new states continues without a satisfactory explanation.

The quark model of low-lying charmonia and bottomonia works very well. The $X_c(3872)$ state, first observed by the Belle experiment in 2003 [5], and the $Y_c(4260)$ state, first observed by the BaBar experiment in 2005 [6], and the $Z_c^+(4433)$ state, first observed by the Belle experiment in 2007 [7], do not fit into the mass spectroscopy of the Quark Model. They all have the $c\bar{c}$ as a constituent and decay into charmonium states, such as the J/ψ , and other descendants. The new states have a very small mass width, and some of them have non-zero charge. Figure 1.3 illustrates the new resonances compared to the $c\bar{c}$ spectroscopy predicted by potential model.

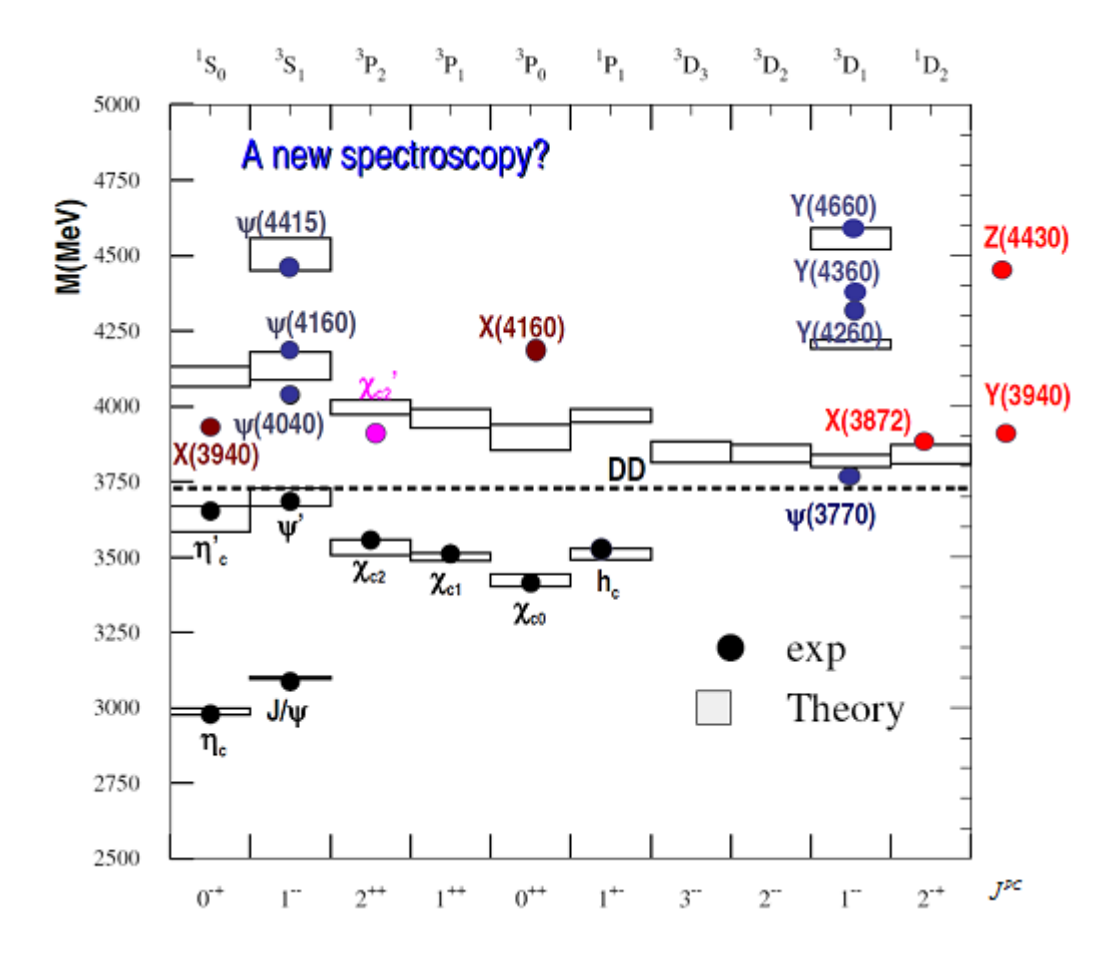


Figure 1.3. New resonances compared to the $c\bar{c}$ spectroscopy predicted by the potential model. The horizontal axis is labeled with the J^{PC} quantum states, where J is the total angular momentum, P the parity, and C the charge conjugation. (R. Mussa. Morriond QCD 2008)

Theorists have hypothesized that these new states may be new forms of aggregation mediated by strong interaction.

Some of the possible explanations are:

- Hybrids state of $q\bar{q}$ + gluons
- Tetraquark state of $[\bar{q}\bar{q}'][qq']$
- Molecules state of $[q\overline{q}][q'\overline{q'}]$

These explanations are speculative. More experimental information is needed to reach a definitive answer to explain these new states which have been discovered.

$X_c(3872)$

The $X_c(3872)$ state (Figure 1.4), observed as the charmonium-like state in $B^+ \to K^+ J/\psi \pi^+ \pi^-$ process, is a narrow resonance state with mass 3,872 ± 0.6 (stat) ± 0.5 (sys)

MeV/c², decaying to $J/\psi \pi^+ \pi^-$. The Belle detector is installed on an electron-positron collider with a center-of-mass system energy of 10.58 GeV at the KEKB collider in Japan [5]. The Belle experiment also reported the observation of $X_c(3872) \to \gamma J/\psi$ and $\omega J/\psi$ decays, confirming the even charge conjugation of the X_c state [4]. The possible quantum numbers of the $X_c(3872)$ state are $J^{PC}=1^{++}$ and 2^{++} , where J is the total angular momentum, P is the parity, and C is the charge conjugation. The observed properties of the $X_c(3872)$ state are consistent with the $D^0 \overline{D}^{*0}$ bound state, as in the molecular model. The $X_c(3872)$ state was confirmed, in the $J/\psi \pi^+ \pi^-$ decay mode, by the CDF and the DØ detectors at the Tevatron, and at the BaBar experiment at SLAC.

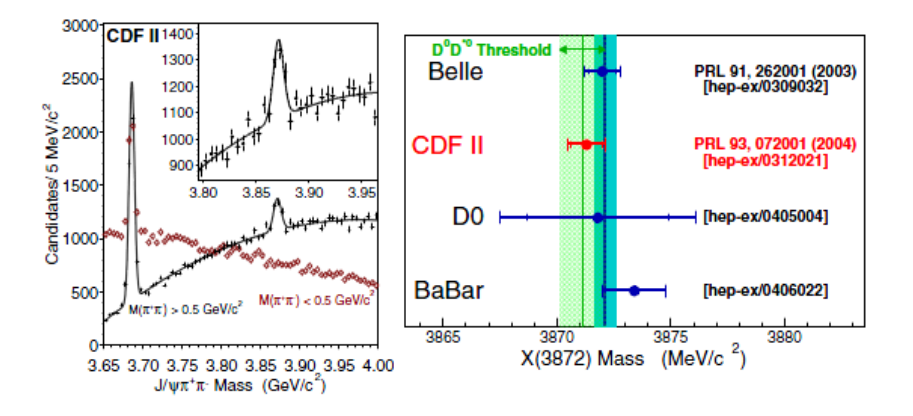


Figure 1.4. The $X_c(3872)$ resonance state mass $(J/\psi\pi^+\pi^-)$, and its comparison with $D^0\overline{D}^{*0}$ threshold.

$Y_c(4260)$

The $Y_c(4260)$ state (Figure 1.5), observed as the charmonium-like state in the $e^+e^- \to \gamma_{ISR}\pi^+\pi^-J/\psi$ decay mode, is a narrow resonance state with mass $4,263\pm 8$ MeV/c², where the ISR stands for Initial State Radiation. The BaBar detector operates at an electron-positron collider with center-of-mass system energy of 10.58 GeV at SLAC in California [6]. The $Y_c(4260)$ state was also confirmed by the CLEO-c, the CLEO-III and the Belle collaborations. In addition to $Y_c(4260) \to \pi^+\pi^-J/\psi$ decay mode, the CLEO detector also observed $Y_c(4260) \to \pi^0\pi^0J/\psi$, $Y_c(4260) \to K^+K^-J/\psi$, where the CLEO detector operated at the CESR e^+e^- collider at $\sqrt{s}=3.97$ -4.26 GeV [8]. The quantum numbers of the $Y_c(4260)$ state are $J^{PC}=1^{--}$, because it is produced by the single photon annihilation.

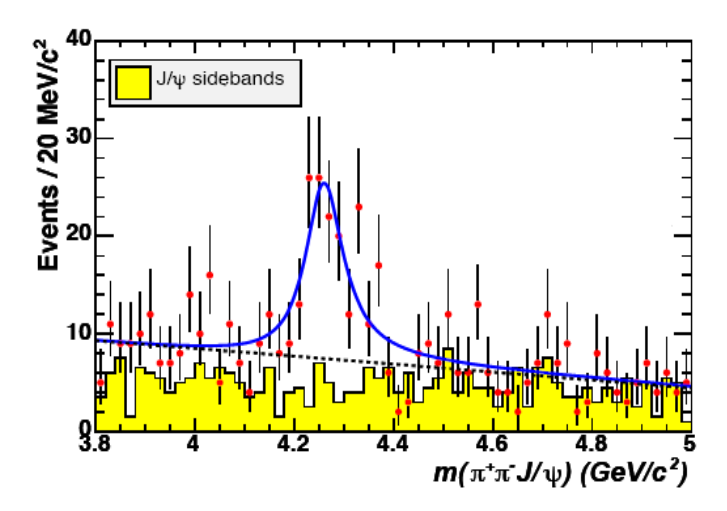


Figure 1.5. The $Y_c(4260)$ resonance state.

$Z_c^+(4433)$

The new resonance-like state $Z_c^+(4433)$ (Figure 1.6), first observed by the Belle Collaboration, has a mass $4{,}433 \pm 4$ (stat) ± 2 (sys) MeV/c². Its decay mode is $\psi(2S)\pi^+$ and has a narrow width of 44 MeV/c² [7] [9]. The natural interpretation of $Z_c^+(4433)$ is that of di-quark-di-antiquark state with flavors $[cu][\bar{c}\bar{d}]$, charged tetraquark bound state with charge +1. The spin parity is $J^{PC}=1^{+-}$, assuming S-wave decay.

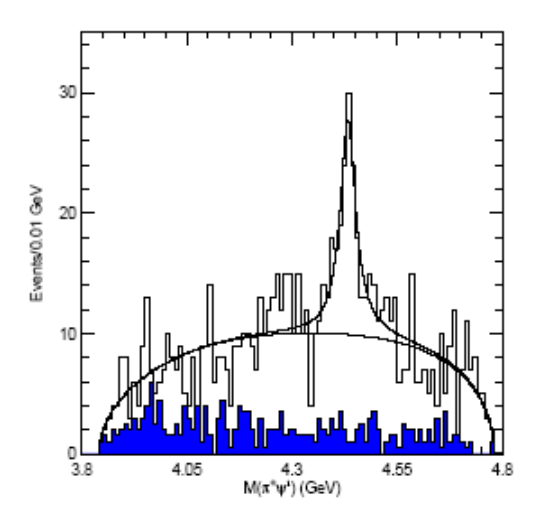


Figure 1.6. The $Z_c^+(4433)$ resonance state.

CHAPTER 2

CHARMONIA AND THEIR PRODUCTION AT HADRON COLLIDERS

This chapter will begin with a discussion of the production of charmonia in hadron collisions at the Tevatron, to be followed by a discussion of charmonium production rates and properties at the Large Hadron Collider (LHC). We will then consider the implementation of charmonium production in pp collisions with the Monte Carlo generator PYTHIA, before closing with a discussion of the manner in which signal events are selected.

2.1 Production of Charmonia at the Tevatron

The charmonium states can be modeled as a charm quark and an anti-charm quark moving in a central potential, leaving the form of the potential to be fitted to data. The charmonium states can be characterized by S as the total spin, L as the orbital angular momentum, and J as the total angular momentum, where J is equal to L+S. Charge conjugation $C = (-1)^{L+S}$ and parity $P = (-1)^{L+1}$ also contain information of the charmonium states. In addition, the notation $I^G(J^{PC})$ represents the isospin (I) and the G-parity (G), respectively. Table 2.1 lists the masses and other properties of the charmonium states. In particular, the $J^{PC} = 1^{+-1}$ states have the same quantum numbers as the photon, which can be produced as resonances in e^+e^- annihilations.

The DØ Detector and the CDF Detector, two major detectors operated at the Tevatron at FNAL, were the leading-edge experiments before the start of experiments at the LHC.

Charmonium production from proton anti-proton collisions was studied by the DØ and the CDF experiments. Figure 2.1 shows the measurement of direct J/ψ production at the Tevatron. The Color Singlet Model (CSM) is the simplest model describing the charmonium production. It shares the benefit of all non-perturbative aspects being absorbed into the wave function of the quarkonium state. In addition, the Color Octet Model (COM) could be used for solving the infrared divergences in the production cross-sections of P-wave states in the CSM, correlating to the non-perturbative color-octet parameter. In Figure 2.1, the COM shows excellent agreement in p_T -dependence with the data at high p_T .

Table 2.1. List of the charmonium states. The column $(n^{2S+1}L_J)$ lists the standard spectroscopic notation of principal quantum number and angular momenta. The column $I^G(J^{PC})$ lists the values of isospin, G-parity, spin, parity and charge conjugation [3].

| Meson Name | $n^{2S}+1L_{J}$ | $I^{G}(J^{PC})$ | Mass(MeV) | Full Width |
|----------------------|-----------------|-----------------|-----------------|---------------|
| η _c (1S) | 1^1S_0 | 0+(0-+) | 2,980.3±1.2 | 25.5±3.4 MeV |
| J/ψ(1S) | 1^3S_1 | 0+(1) | 3,096.916±0.011 | 93.4±2.1 keV |
| h _c (1P) | $1^{1}P_{1}$ | $0^+(1^{+1})$ | 3,525.93±0.27 | |
| χ _{c0} (1P) | $1^{3}P_{0}$ | $0^{+}(0^{++})$ | 3,414.75±0.31 | 10.4±0.7 MeV |
| χ _{c1} (1P) | 1^3P_1 | 0+(1++) | 3,510.66±0.07 | 0.89±0.05 MeV |
| χ _{c2} (1P) | $1^{3}P_{2}$ | 0+(2++) | 3,556.20±0.09 | 2.06±0.12 MeV |
| η _c (2S) | $1^{1}S_{0}$ | 0+(0-+) | 3637±4 | |
| ψ(2S) | 2^3S_1 | 0-(1) | 3,686.09±0.04 | 337±13 keV |
| ψ(3770) | $1^{3}D_{1}$ | 0-(1) | 3,772.92±0.35 | |

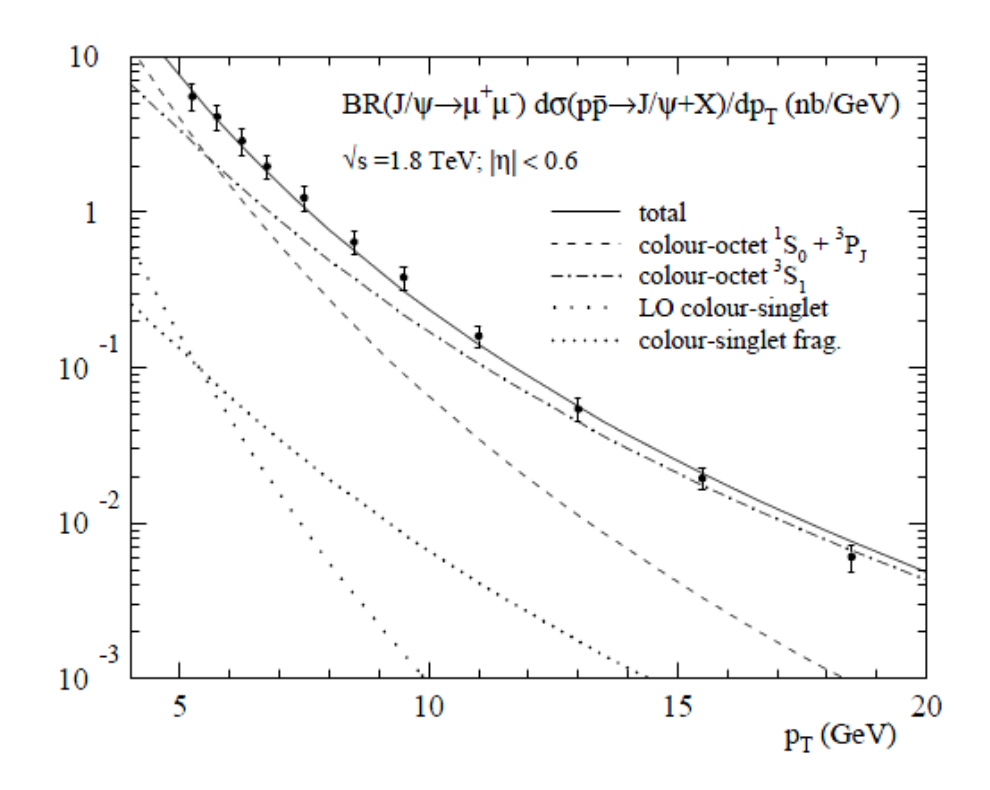


Figure 2.1. Differential cross-section of J/ψ production at the Tevatron with theoretical predictions for color-singlet and color-octet model production [10].

Color singlet: $(r\bar{r} + b\bar{b} + g\bar{g})/\sqrt{3}$

Color octet:
$$(r\bar{b} + b\bar{r})/\sqrt{2}$$
 $-i(r\bar{b} - b\bar{r})/\sqrt{2}$ $(r\bar{g} + g\bar{r})/\sqrt{2}$ $-i(r\bar{g} - g\bar{r})/\sqrt{2}$ $(b\bar{g} + g\bar{b})/\sqrt{2}$ $-i(b\bar{g} - g\bar{b})/\sqrt{2}$ $(r\bar{r} - b\bar{b})/\sqrt{2}$ $(r\bar{r} + b\bar{b} - 2g\bar{g})/\sqrt{6}$

2.2 Production of Charmonia at the Large Hadron Collider

In addition to the ATLAS (A Toroidal LHC Apparatus) experiment, the CMS (Compact Muon Solenoid) experiment and the LHCb (Large Hadron Collider beauty) experiment can perform quarkonium studies at the LHC. There are several challenges for charmonia detection at the LHC, including the triggering of events and the combinatorial background. For the ATLAS detector and this analysis, charmonium states are measured in the di-muon decay channel which benefits from the excellent muon detection capabilities for $|\eta| < 2.5$ and $p_T > 3$ GeV/c, provided by the muon spectrometers. For the J/ψ production, there will be about 17,000 J/ψ per 1 pb⁻¹, produced [11].

The ATLAS experiment at the LHC is able to check the predictions of charmonium models in detail. The ATLAS detector can measure the p_T and η distributions of charmonium states in a wide range, the degree of polarization, associated hadronic activity, and so on [12]. The performance of the ATLAS detector can be modeled by Monte Carlo simulation. The PYTHIA 6.403 generator is used for producing necessary models, including the CSM and the COM, with parameters fixed through a combination of theoretical and experimental constraints [13]. The Monte Carlo samples are used to study the acceptance and efficiency of the ATLAS detector to detect all required particles and measure their parameters across the whole range of the phase space. The large cross-section of J/ψ production and the lack of transverse polarization in the J/ψ decays will be examined by the LHC.

Figure 2.2 shows the inclusive J/ψ cross-sections for charmonium production at the LHC, $\sqrt{s} = 7$ TeV, measured with an integrated luminosity 2.2 pb⁻¹. The equivalent results from CMS are overlaid [14]. In addition, J/ψ production is observed by the LHCb experiment [15]. Figure

2.3 shows the predictions for prompt J/ψ direct production at the LHC using the CTEQ PDF, where CTEQ stands for the Coordinated Theoretical-Experimental Project on QCD, and PDF stands for the Parton Distribution Functions. In changing the choice for the PDF there are noticeable changes on the production rate by about 50% in certain regions of p_T .

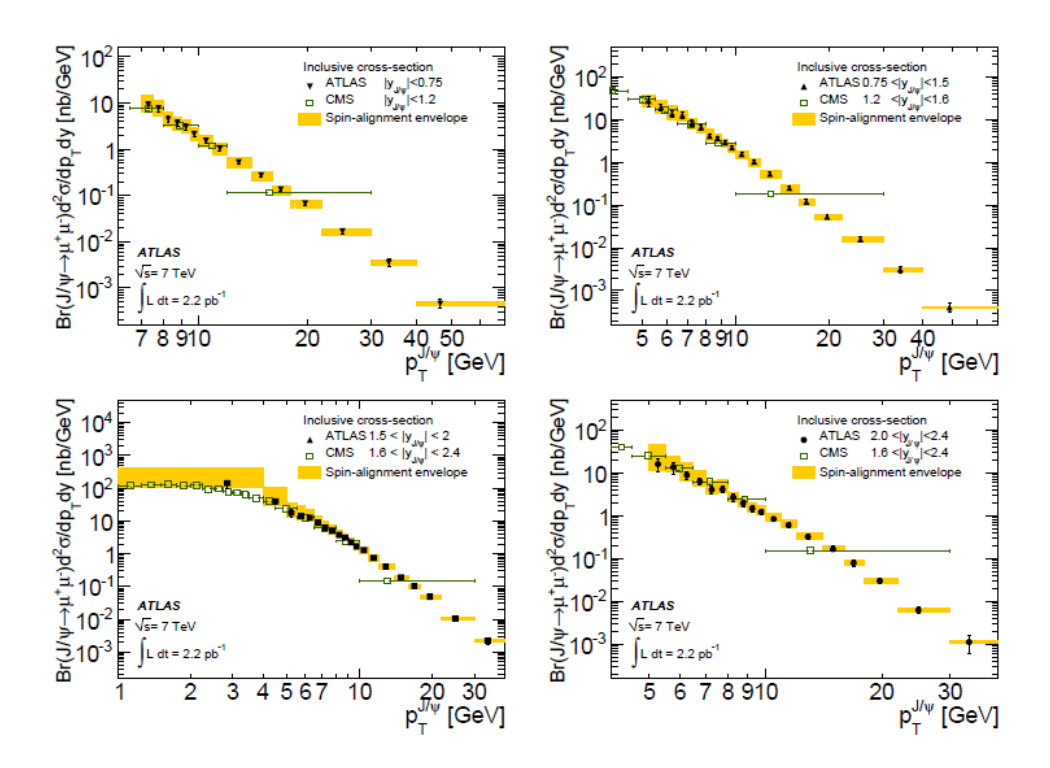


Figure 2.2. Inclusive J/ψ production cross-section as a function of J/ψ transverse momentum in four rapidity bins. Overlaid is a band representing the variation of the result under various spin-alignment scenarios representing a theoretical uncertainty. The equivalent results from CMS are overlaid. The luminosity uncertainty (3.4%) is not shown [14].

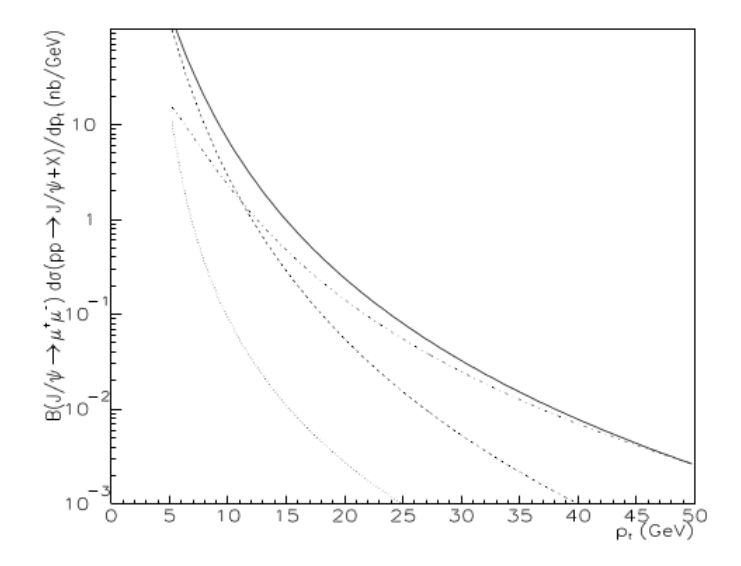


Figure 2.3. The predictions for prompt J/ψ direct production at the LHC according to the color-octet model implemented in the PYTHIA for the CTEQ PDF. Dotted line: CSM; dashed line: ${}^{1}S_{0}^{(8)} + {}^{3}P_{J}^{(8)}$ contributions; dot-dash line: ${}^{1}S_{1}^{(8)}$ contribution; solid line: all contributions. Notice that asymptotically the ${}^{1}S_{1}^{(8)}$ contribution becomes dominant, likely implying a transverse polarization of charmonium at high p_{T} [12].

2.3 The PYTHIA Predictions and the Cross-Sections of $pp \rightarrow ggX$

The physics processes under study are produced by Monte Carlo simulation generators. The PYTHIA generator [13] has been used to generate samples of quarkonium events for studying quarkonium production at ATLAS. The PYTHIA predictions of cross-sections for $pp \to J/\psi \to \mu^+\mu^- X$ are calculated for a number of p_T thresholds on the di-muon trigger. Table 2.2 shows the PYTHIA predictions for di-muon p_T thresholds and one single muon trigger.

Figure 2.4 illustrates the distribution of cross-sections across the values of the muon p_T from quarkonium decay. The lines on the plots represent the harder and softer di-muon trigger cuts, 6+4 GeV/c (μ 6 μ 4), 4+4 GeV/c (μ 4 μ 4), and 10+0.5 GeV/c, respectively. Most of the J/ψ cross-section bulk lies near the 4+1 GeV/c region, and it is far from the low- p_T muon trigger

thresholds used by ATLAS. There is a small increase in the accessible cross-section by lowering the cut on the harder muon from 6 GeV/c to 4 GeV/c.

Table 2.2. Predicted cross-sections for various prompt vector quarkonium state production and decay into muons, with di-muon trigger thresholds $\mu 4 \mu 4$ and $\mu 6 \mu 4$ and the single muon trigger threshold $\mu 10$ (before trigger and reconstruction efficiencies). The last column shows the overlap between the di-muon $\mu 6 \mu 4$ and single muon samples. The "single" muon sample also requires that the second muon has a $p_T > 0.5~GeV/c$.

| Quarkonium | Cross-section, nb | | | | | |
|----------------|-------------------|------|----------|----------|--|--|
| Quarkonium | μ4μ4 | μ6μ4 | μ 10 | µ6μ4∩µ10 | | |
| J/ψ | 28 | 23 | 23 | 5 | | |
| ψ' | 1.0 | 0.8 | 0.8 | 0.2 | | |
| $\Upsilon(1S)$ | 48 | 5.2 | 2.8 | 0.8 | | |
| Υ(2S) | 16 | 1.7 | 0.9 | 0.3 | | |
| Y(3S) | 9.0 | 1.0 | 0.6 | 0.2 | | |

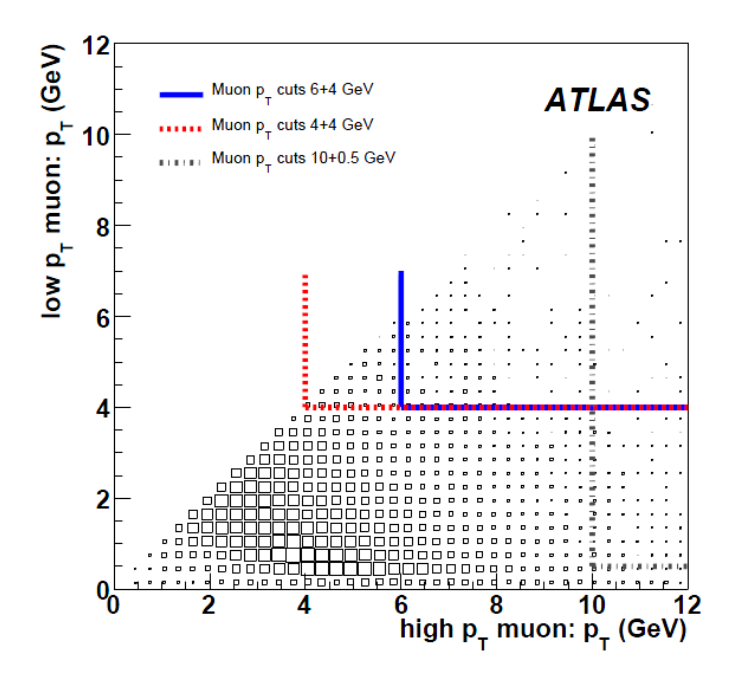


Figure 2.4. Density of the J/ψ production cross-section as a function of the hardest and softer muon p_T of muons coming from the J/ψ . No cut was placed on the generated sample, but the overlaid lines represent the thresholds of observed events with trigger cuts applied.

The official document, published by the European Organization for Nuclear Research (CERN), gives the estimations of expected rates and composition of inclusive low p_T muons from decays of the B-hadrons, inclusive charm and direct heavy quarkonia, for the 14 TeV run in ATLAS. Event generation was performed using the PYTHIA 6.403, and no consideration of detector effects is taken into account except for the fiducial cuts of the ATLAS detector volume. Referring to Figure 2.5, the plot of hardest muon p_T combines the muon rate summary plots for all interested physics processes, without charge correlation required for the second muon. In Figure 2.6, the plot combines the second hardest muon p_T spectra for physics processes with a dimuon trigger. Both the differential and integrated cross-section spectra are presented in each case and the relevant processes have been overlaid to allow for quick comparison. Table 2.3 shows the summary of the predicted rates for both thresholds.

Table 2.3. Predicted cross-sections for various muon and di-muon sources.

| Process (μ6 threshold) | Cross-section | Process (μ4 threshold) | Cross-section |
|-------------------------------------|---------------|--------------------------------------|---------------|
| $bb \rightarrow \mu 6X$ | 6.14 μb | $bb \rightarrow \mu 4X$ | 19.3 μb |
| $cc \rightarrow \mu 6X$ | 7.9 µb | $cc \rightarrow \mu 4X$ | 26.3 μb |
| $bb \rightarrow μ6μ4X$ | 110.5 nb | $bb \rightarrow \mu 4\mu 4X$ | 212.0 nb |
| $cc \rightarrow \mu 6\mu 4X$ | 248.0 nb | $cc \rightarrow \mu 4\mu 4X$ | 386.0 nb |
| $pp \rightarrow J/\psi(μ6μ4)X$ | 21.7 nb | $pp \rightarrow J/\psi(\mu 4\mu 4)X$ | 27.0 nb |
| $pp \rightarrow \Box (\mu 6\mu 4)X$ | 4.57 nb | $pp \rightarrow \Box (\mu 4\mu 4)X$ | 43.0 nb |
| bb \rightarrow J/ψ(μ6μ4)X | 11.06 nb | $bb \rightarrow J/\psi(\mu 4\mu 4)X$ | 12.5 nb |

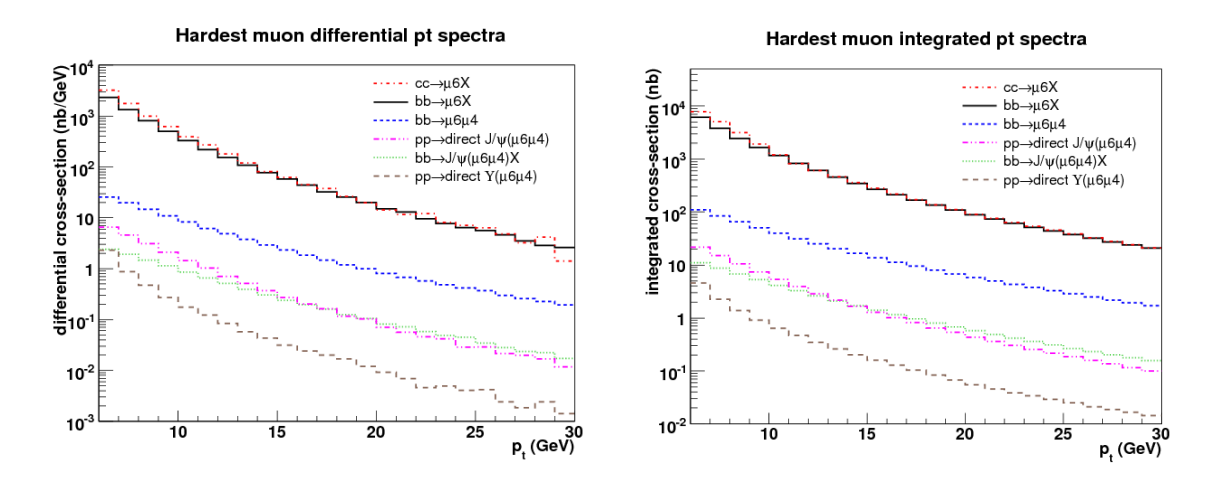


Figure 2.5. Combined plots of differential and integrated muon p_T spectra showing hardest muon rates for $bb \to \mu 6X$, $bb \to \mu 6\mu 4X$, $bb \to J/\psi(\mu 6\mu 4)X$, $cc \to \mu 6X$, direct J/ψ , and direct \Box processes (no charge correlation).

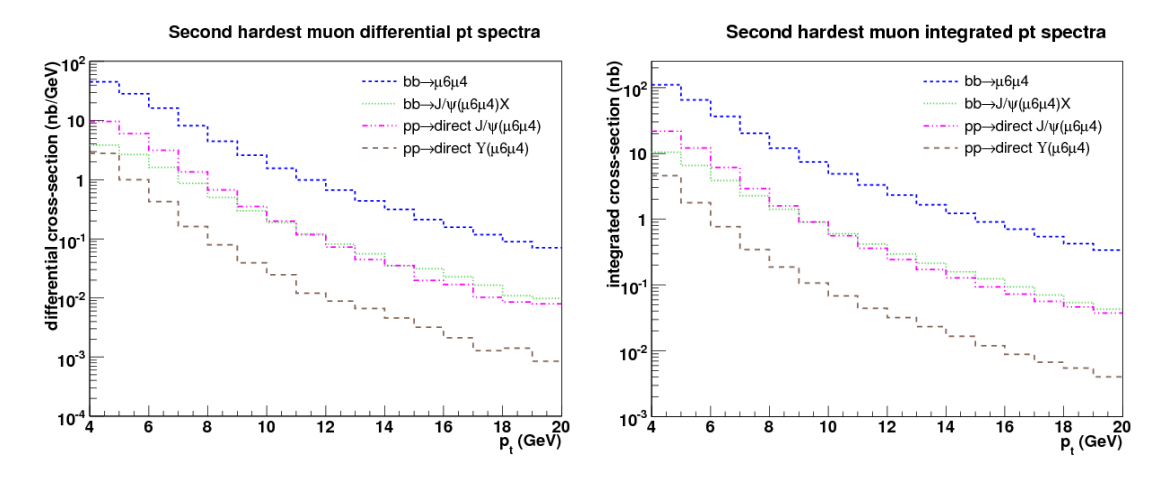


Figure 2.6. Combined plots of differential and integrated muon p_T spectra showing rates of the second hardest muon in the event for $bb \rightarrow \mu 6\mu 4X$, $bb \rightarrow J/\psi(\mu 6\mu 4)X$, $cc \rightarrow \mu 6X$, direct J/ψ , and direct \Box processes (no charge correlation).

2.4 Search for New Charmonium-like States

This dissertation describes the search for new charmonium-like states, X_c , Y_c with the ATLAS detector at the LHC, where the X_c and Y_c states will be reconstructed via their decays to

 $J/\psi \pi^+\pi^-$. The charmonium-like states discovered at the B factories, at the Tevatron, and at the CLEO_c, seem to point to a breakdown in the Quark Model of hadrons as described in Chapter 1. The Quark Model cannot correctly predict the masses of these states as well as the J^{pc} quantum numbers. It is imperative that more of these X_c , Y_c states be discovered to help reveal the underlying physics. The high rate of charmonium production at the LHC provides an excellent and unique place for searching for new X_c , Y_c states.

The X_c and Y_c states can be found and reconstructed through their decays to $J/\psi\pi^+\pi^-$ decay, where the J/ψ will be detected in its decay to a $\mu^+\mu^-$ pair. The search is conducted inclusively, where signals from all production mechanisms will be included, for the maximum chance to detect these states. The observed decay modes from the B factories, the Tevatron, and the CLEO_c, include: $X_c(3872) \to J/\psi\pi\pi$, $X_c(3872) \to \gamma J/\psi$, $X_c(3872) \to \omega J/\psi$, $Y_c(4260) \to J/\psi\pi\pi$, and $Y_c(4260) \to J/\psi KK$ modes. In this dissertation, the $J/\psi\pi^+\pi^-$ decay mode is analyzed with the ATLAS data.

The $X_c(3872) \rightarrow J/\psi \pi^+ \pi^-$ is observed by the LHCb and the CMS experiments. Figure 2.7 shows the $J/\psi \pi^+ \pi^-$ mass distribution measured by the LHCb experiment, with an integrated luminosity $34.7 \pm 1.2 \text{ pb}^{-1}$. Both $\psi(2S)$ and $X_c(3872)$ are observed [16]. Figure 2.8 shows the $J/\psi \pi^+ \pi^-$ mass distribution measured by the CMS experiment, with integrated luminosities 40 pb⁻¹ in 2010 data and 896 pb⁻¹ in 2011 data, respectively. Both $\psi(2S)$ and $X_c(3872)$ are observed [17].

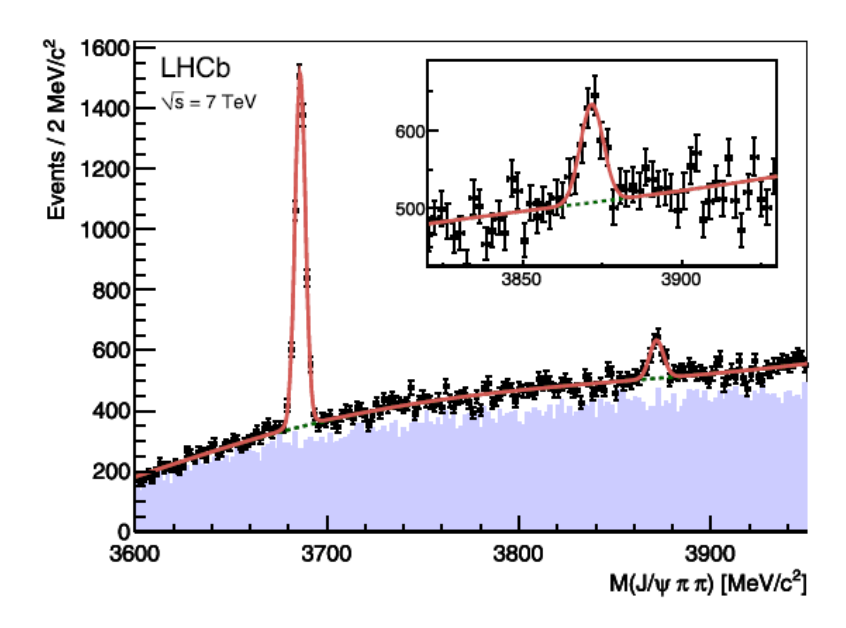


Figure 2.7. $J/\psi \pi^+\pi^-$ mass distribution measured by the LHCb experiment [16].

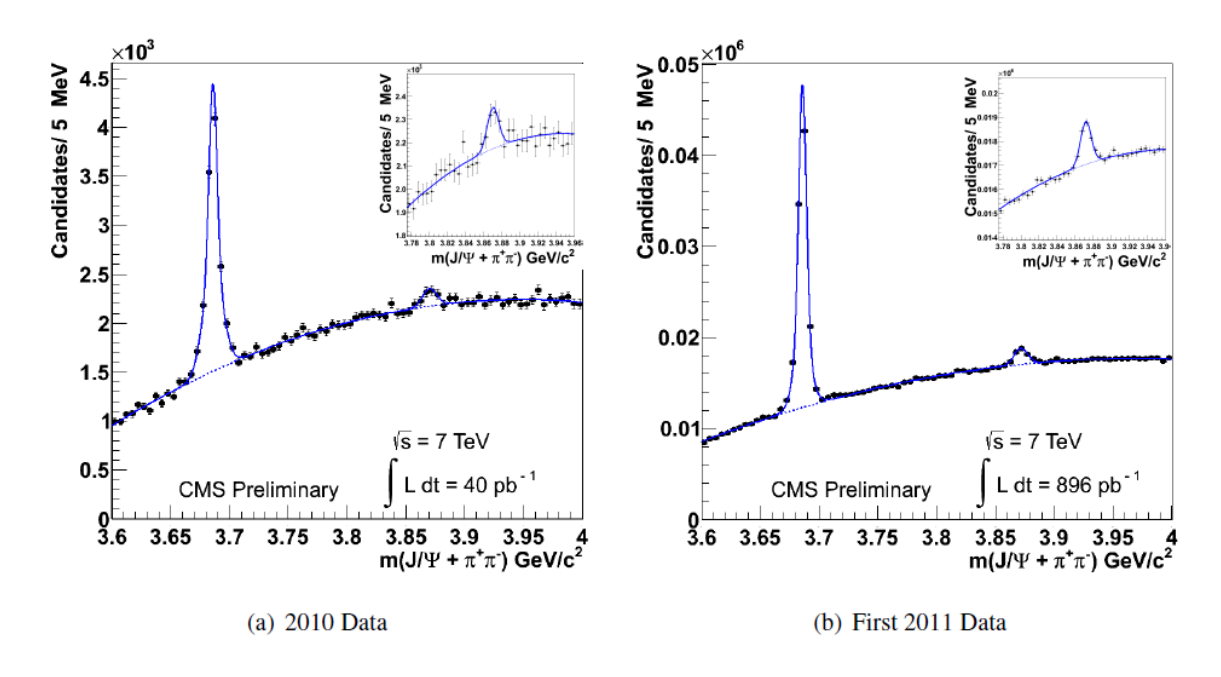


Figure 2.8. $J/\psi \pi^+\pi^-$ mass distribution measured by the CMS experiment [17].

CHAPTER 3

EXPERIMENTAL APPARATUS

3.1 The Large Hadron Collider

The Large Hadron Collider (LHC) (Figure 3.1), operated by CERN, is a proton-proton synchrotron accelerator located at Meyrin, on the Swiss-French border. The LHC ring is built in the former 27 km circumference Large Electron-Positron Collider (LEP) tunnel. The LHC is designed to produce protons beams with a final energy of 7 TeV, circulating in both the clockwise and counterclockwise directions. Ultimately the LHC will reach 14 TeV in the center-of-mass system with luminosity of 10³⁴ cm⁻²s⁻¹ and proton bunches separated 25 ns apart, delivering collisions at four interaction points along the LHC beam line. The beams are designed to be structured in 2808 bunches with 10¹¹ protons each, and to make 40,000,000 bunch-bunch collisions per second [18].

The acceleration of proton beam is performed in several stages. Protons are initially injected and accelerated to 50 MeV in a linear accelerator. The protons are then accelerated in the 1.4 GeV Proton Synchrotron booster and the 26 GeV Proton Synchrotron (PS). Subsequently, the protons are injected into the Super Proton Synchrotron (SPS). The energy of the protons is 450 GeV before being injected into the LHC.

Due to the incident involving superconducting electrical connections on September 19, 2008, the LHC was shut down and repaired for one year. The LHC restarted at 900 GeV in

November, 2009, and was then ramped up to 2.36 TeV (center-of-mass system) collisions in December, 2009. The proton collision data were collected a few weeks before the winter break. The LHC energy has been boosted to run at 7 TeV (center of mass system) since the end of February, 2010.

Figure 3.1 shows the locations of the four main experiments (ALICE (A Large Ion Collider Experiment), ATLAS, CMS (Compact Muon Solenoid), and LHCb (Large Hadron Collider beauty)) that take place at the LHC. Located between 50 m and 150 m underground, huge caverns have been excavated to house the giant detectors. The SPS, the final link in the preacceleration chain, and its connection tunnels to the LHC are also shown.

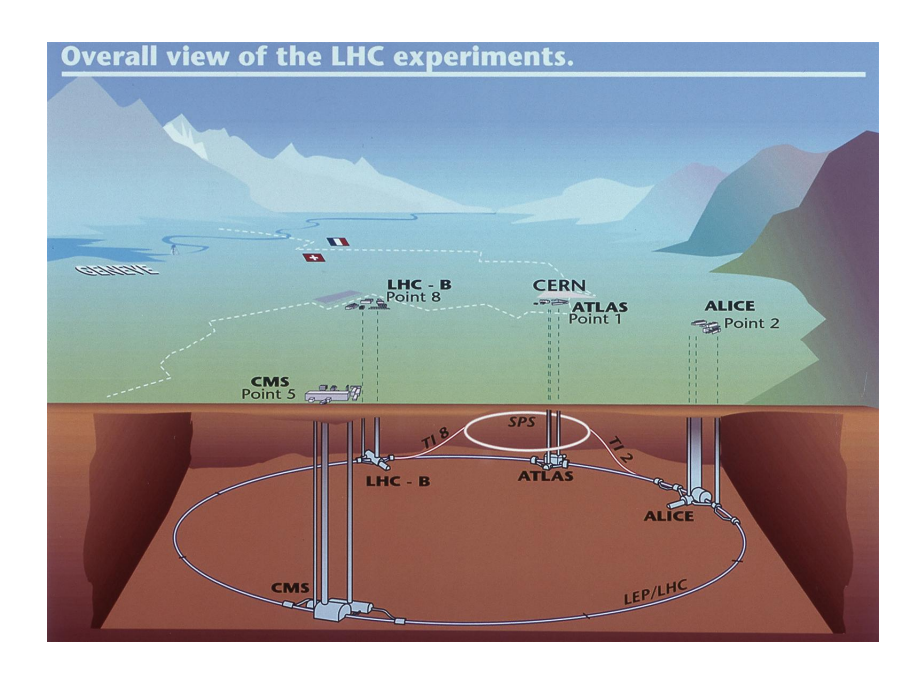


Figure 3.1. The overall view of the LHC.

3.2 The ATLAS Detector

3.2.1 Overview

The ATLAS Detector (A Toroidal LHC ApparatuS) (Figure 3.2) which is one of two general purpose detectors at the LHC is situated at Point 1, directly opposite the CERN main entrance. The construction of the ATLAS detector had been finished in 2008, and it detected the first beam in September. The ATLAS detector is designed as a cylinder with a total length of 42 m, a radius of 11 m, and weighs approximately 7,000 tons [19].

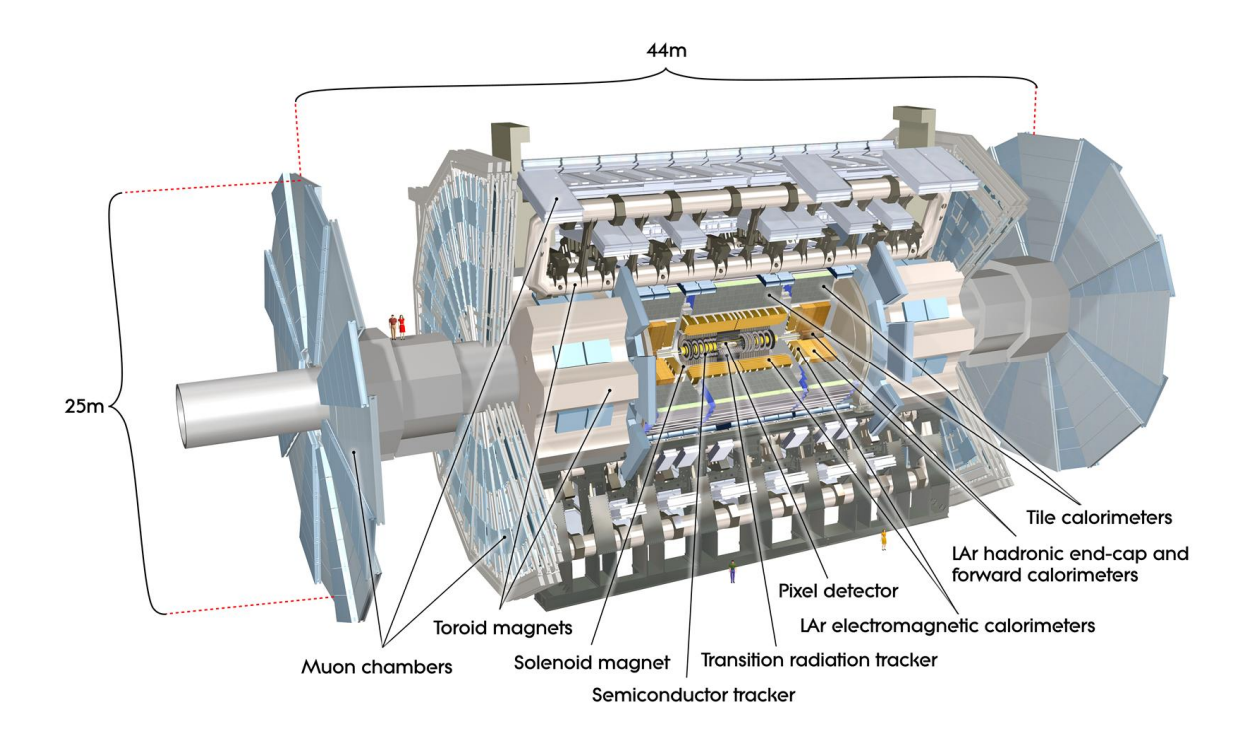


Figure 3.2. The overall view of the ATLAS Detector.

The ATLAS detector consists of four major components, including the Inner Detector, the Calorimeters, the Muon spectrometer, and the Magnet system. The Inner Detector which is the

tracking system of ATLAS, tracks charged particles and measures their momenta precisely. The Calorimeters measure the energies of particles. The Muon spectrometer identifies and measures the momenta of muons. The Magnet system, including the inner solenoid magnet and the outer toroidal magnets, bends charged particles in the Inner Detector and the Muon spectrometer, respectively.

3.2.2 The Coordinate System

The Coordinate System of the ATLAS detector is a right-handed system with the direction of the z-axis following the beam direction and the x-y plane transverse to the beam direction. The positive z direction is towards detector side A, the direction of Geneva Airport, with a slope of -1.23%. The negative z direction is towards detector side C. The x-axis points to the center of the LHC ring, and the y-axis goes upwards. The transverse momentum p_T of a detected particle is defined as its momentum in the x-y plane [19].

The azimuthal angle ϕ is measured around the z-axis, and the range is $[-\pi, +\pi]$. The angle $\phi=0$ corresponds to the positive x-axis and ϕ increases clock-wise looking into the positive z direction. The polar angle θ is measured from the positive z axis. The pseudorapidity, η , is defined by

$$\eta = -\log\left(\tan\frac{\theta}{2}\right)$$

The distance in the pseudorapidity azimuthal angle space is given by

$$\Delta R = \sqrt{\Delta \eta^2 + \Delta \emptyset^2}$$

3.2.3 The Central Tracking System

The Inner Detector (ID) (Figure 3.3), the central tacking system of the ATLAS detector, provides high-precision measurements of charged particle tracks, where the number of tracks per event is roughly 1000.

It consists of three parts: a barrel part and two end cap parts. The barrel part is arranged in concentric circles around the beam axis. The two identical end caps are mounted on disks which are perpendicular to the beam axis covering the rest of the cylindrical cavity. The Inner Detector is composed of three components, the Pixel Detector, the Semiconductor Tracker (SCT), and the Transition Radiation Tracker (TRT). The Pixel Detector is used for reconstructing the primary and second vertices, and the decay length, the SCT plays the role of precisely measuring the particle momenta, and the TRT is used to ease the pattern recognition. The Inner Detector surrounds the LHC beam-pipe, which has a radius of 36 mm, and is immersed in a 2 Tesla magnetic field generated by the central solenoid magnet [20]. Figure 3.4 shows the layout of the Inner Detector, and Table 3.1 gives the relevant parameters. The details of each component of the ID will be described later.

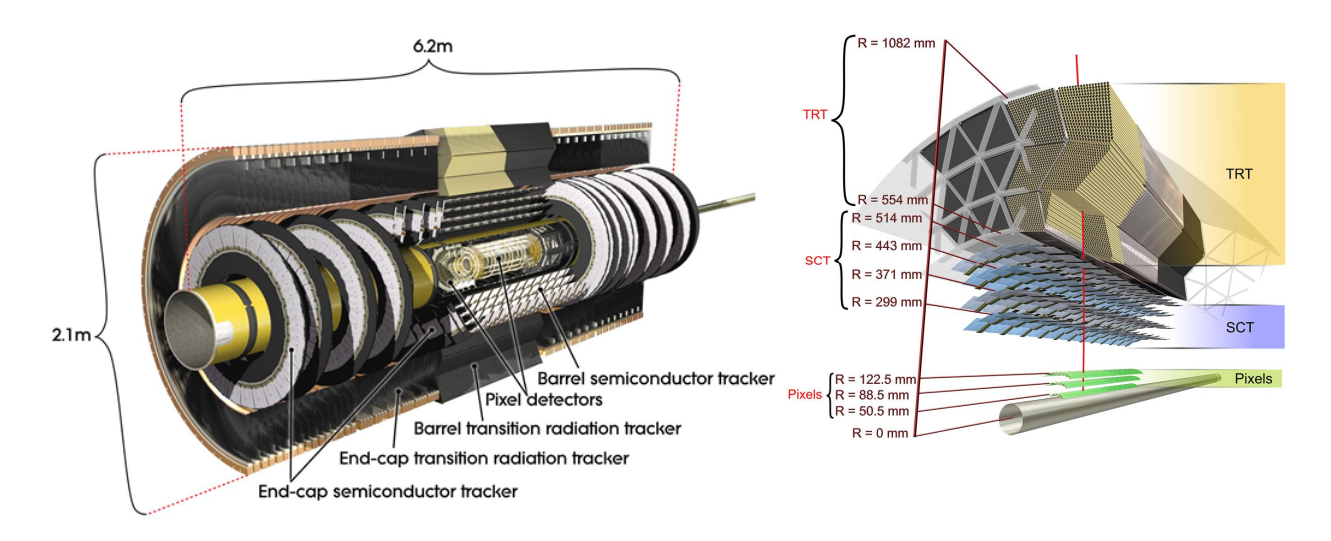


Figure 3.3. (Left) Cut-away view of the Inner Detector. (Right) Structural components traversed by a charged particle passing through the barrel region of the Inner Detector.

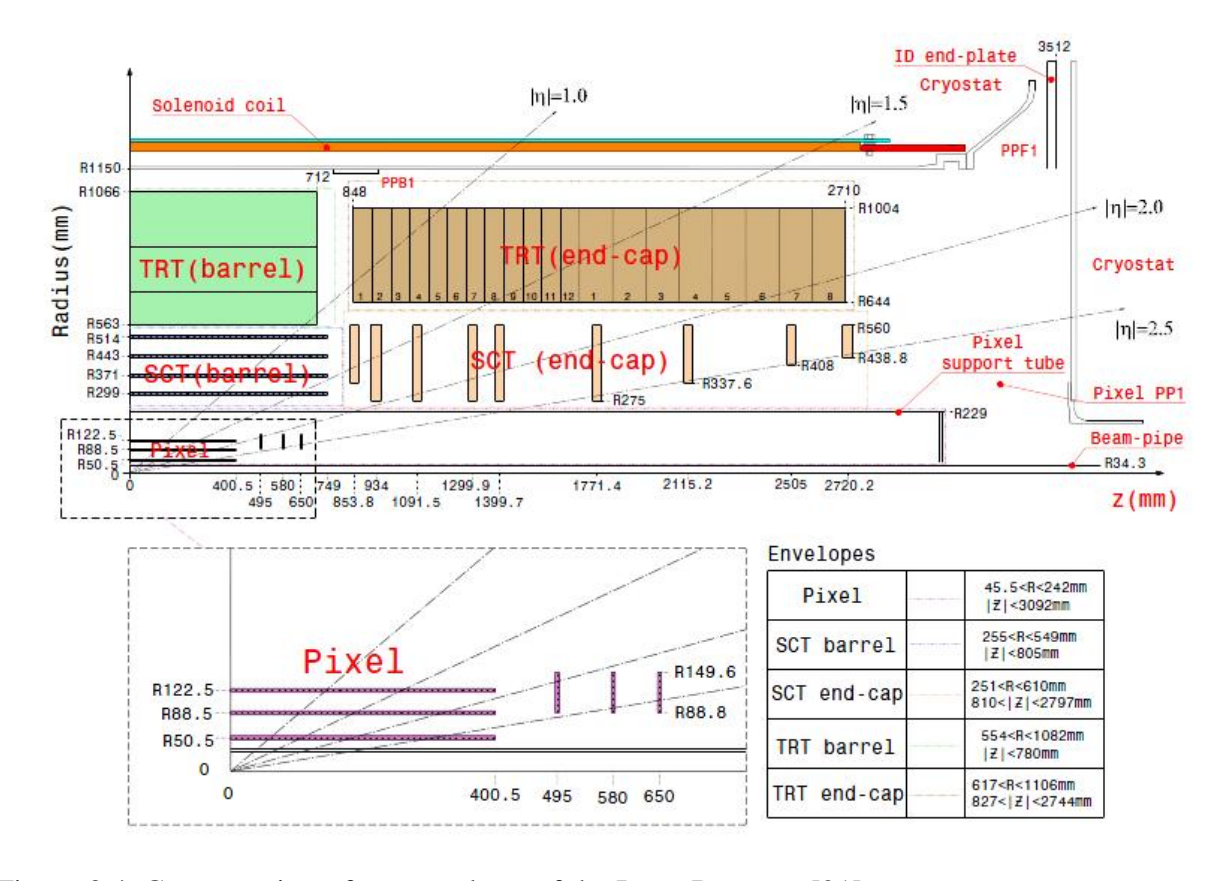


Figure 3.4. Cross-section of one quadrant of the Inner Detector [21].

| Item | | Radial extension (mm) | Length (mm) |
|----------------------|-------------------|---|---|
| Pixel | Overall envelope | 45.5 < R < 242 | 0 < z < 3092 |
| 3 cylindrical layers | Sensitive barrel | 50.5 < R < 122.5 | 0 < z < 400.5 |
| 2×3 disks | Sensitive end-cap | 88.8 < R < 149.6 | 495 < z < 650 |
| SCT | Overall envelope | 255 < R < 549 (barrel) 251 < R < 610 (end-cap) | $\begin{vmatrix} 0 < z < 805 \\ 810 < z < 2797 \end{vmatrix}$ |
| 4 cylindrical layers | Sensitive barrel | 299 < R < 514 | 0 < z < 749 |
| 2×9 disks | Sensitive end-cap | 275 < R < 560 | 839 < z < 2735 |
| TRT | Overall envelope | 554 < R < 1082 (barrel) 617 < R < 1106 (end-cap) | $\begin{vmatrix} 0 < z < 780 \\ 827 < z < 2744 \end{vmatrix}$ |
| 73 straw planes | Sensitive barrel | 563 < R < 1066 | 0 < z < 712 |
| 160 straw planes | Sensitive end-cap | 644 < R < 1004 | 848 < z < 2710 |

Table 3.1. Parameters of the Inner Detector [21].

The tracking performance of the Inner Detector is important for reconstructing single particles, unstable particles, and particles in jets. The tracking performance of the Inner Detector is characterized by the track resolution

$$\sigma_X(p_T) = \sigma_X(\infty) \left(1 \oplus \frac{p_X}{p_T}\right)$$

 σ_x : the resolution of a track in the x-y plane.

 $\boldsymbol{\sigma}_{\boldsymbol{X}}(\infty)$: the asymptotic resolution expected at infinite momentum

 $\boldsymbol{p}_{_{\boldsymbol{X}}}$: transverse momentum (the constant representing the value of $\boldsymbol{p}_{_{\boldsymbol{T}}}\!)$

Table 3.2. Expected track-parameter resolutions (RMS) at infinite transverse momentum, σ_{X} (∞), and transverse momentum, p_{X} , at which the multiple-scattering contribution equals that from the detector resolution [21].

| Track parameter | $0.25 < \eta < 0.50$ | | $1.50 < \eta < 1.75$ | |
|--|------------------------|-------------|-------------------------|-------------|
| | $\sigma_X(\infty)$ | p_X (GeV) | $\sigma_X(\infty)$ | p_X (GeV) |
| Inverse transverse momentum (q/p_T) | 0.34 TeV ⁻¹ | 44 | 0.41 TeV^{-1} | 80 |
| Azimuthal angle (ϕ) | 70 μ rad | 39 | 92 μ rad | 49 |
| Polar angle $(\cot \theta)$ | 0.7×10^{-3} | 5.0 | 1.2×10^{-3} | 10 |
| Transverse impact parameter (d_0) | 10 μm | 14 | $12 \mu m$ | 20 |
| Longitudinal impact parameter $(z_0 \times \sin \theta)$ | 91 μm | 2.3 | $71 \mu \mathrm{m}$ | 3.7 |

Pixel Detector

The Pixel Detector contains 3 layers of pixel modules, both in the barrel part and the end cap parts. In the barrel part, the 3 cylindrical layers are located at the radial positions of 50.5 mm, 88.5 mm, and 122.5 mm, and there are 22, 38, and 52 staves in each layer, respectively. The layers are made of identical staves inclined with an azimuthal angle of 20 degrees, and each stave is composed of 13 pixel modules. The end caps are located in the forward regions. Each layer is a disk with 8 sectors, and 6 modules in each sectors. There are 16 front-end (FE) chips and one Module Control Chip (MCC) on each module. Each FE chip contains 160 rows and 18 columns, 2880 channels in total. The pixel sensor is a 16.4×60.8 mm wafer of silicon with 46,080 pixel read out channels, 50×400 microns, in the modules. Overall, there are 1744 modules in the Pixel Detector providing just over 80 million channels [22].

Semi-Conducting Tracker (SCT)

The Semiconducting Tracker (SCT) and the Pixel Detector work in a similar manner. The SCT is used to provide eight precision measurements per track in the intermediate radial range, contributing to the measurement of momentum, impact parameter and vertex position. In the barrel part of the SCT, 8 layers of silicon microstrip detectors provide precision points in the r- ϕ and z coordinates. Each silicon detector is 6.36×6.40 cm² in size with 768 readout strips of 80 micron pitch. The barrel modules are mounted on carbon-fiber cylinders at radii of 30.0, 37.3, 44.7, and 52.0 cm. The end-cap modules are very similar in construction but use tapered strips with one set aligned radially [22].

Transition Radiation Tracker (TRT)

The Transition Radiation Tracker (TRT), outside of the precision detectors (SCT and Pixel), distinguishes between different types of particles. The TRT is made up of straws, 4 mm in diameter, filled with Xenon gaseous mixture and possesses a gold plated wire at the center to serve as an anode. The barrel consists of 52,544 axial straws, 150 cm in length at radii between 56 cm and 107 cm, each divided into two at the center, and the end caps consist of 319488 radial straws at radii between 64 cm and 103 cm (inner end-caps), 48 cm and 103 cm (outer end-caps), respectively. There are altogether 420,000 readout channels in the TRT. The TRT provides on average 36 two-dimensional measurement points (r- ϕ) with a 0.170 mm resolution for charged particle tracks with $|\eta| < 2.5$ and $p_T > 0.5$ GeV. When a charged particle passes through the straws, electrons are produced. An electron, for example, ionizes the gas and produces more photons, which in turn produce more electrons, and thus more current is measured at the gold plated wire. In addition, the ionization rate by a pion is less than that by an electron, so the electrons can also be identified. The momentum of the charged particle can then be calculated [221].

3.2.4 The Magnet System

The Magnet System (Figure 3.5) of the ATLAS detector consists of 3 superconducting sub-systems: 1 Solenoid magnet, 1 Barrel Toroid, and 2 End-Cap Toroids, providing magnetic field configuration for charged particle bending around the sub-detectors. The Central Solenoid, made as a single layer coil, is 5.3 m in length and 45 millimeters in thickness with a bore of 2.4 m. It provides a 2 Tesla magnetic field in the central tracking volume with a peak value of 2.6

Tesla. The solenoid shares the cryostat with the liquid argon calorimeter to reduce the material budget [23] [24].

The Barrel Toroid consists of 8 flat superconducting race-track coils, each 25 meters long and 5 meters wide, grouped in a torus shape. It provides a magnetic field of between 3 - 8 Tesla, at the central region of muon spectrometer. The two End-Cap Toroids, 11 meters in diameter and 5 meters in width each, are inside the Barrel Toroid at both ends of the Central Solenoid. They provide a magnetic field of between 3 - 8 Tesla in the forward regions of the ATLAS detector across a radial span of 1.7 to 5 meters. The coils of the End-Cap Toroids are rotated by 22.5° with respect to the Barrel Toroid coils, causing the radial overlap and the optimization of the magnetic bending power in the interface region of the toroids. The Barrel Toroid and the End-Cap Toroids are electrically connected in series, operated at a current of 20,500 amperes providing a peak field of 4 Tesla [23].

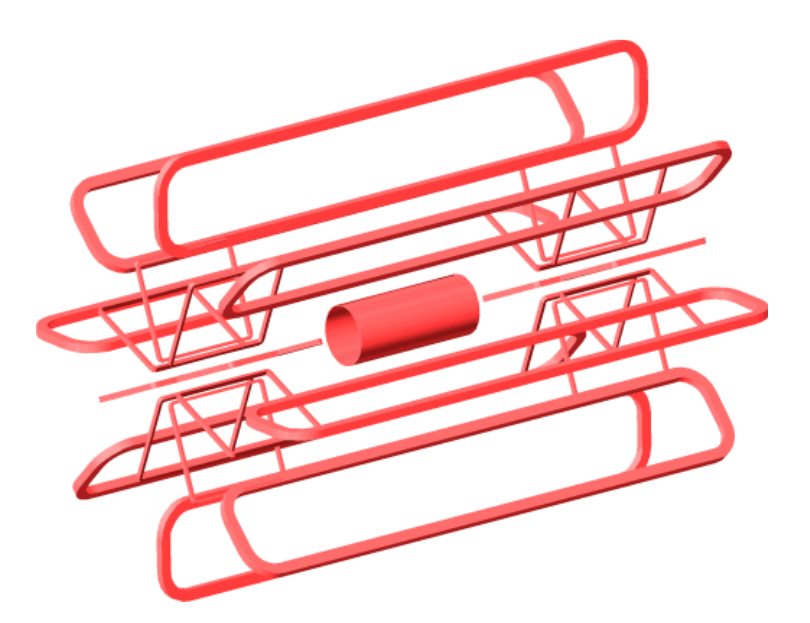


Figure 3.5. The ATLAS Magnet System.

3.2.5 The Calorimeters

The Calorimeters (Figure 3.6), surrounding the Inner Detector and the Solenoid, are used to measure the energies of particles. They consist of two major parts: the Liquid Argon (LAr) Calorimeter (Electromagnetic Calorimeter (ECAL)), measuring energies of electrons and photons, and the Tile Calorimeter (Hadronic Calorimeter (HCAL)), measuring the energies of hadrons. Including calorimeters in the forward region, they cover the pseudorapidity region within $|\eta| < 4.9$.

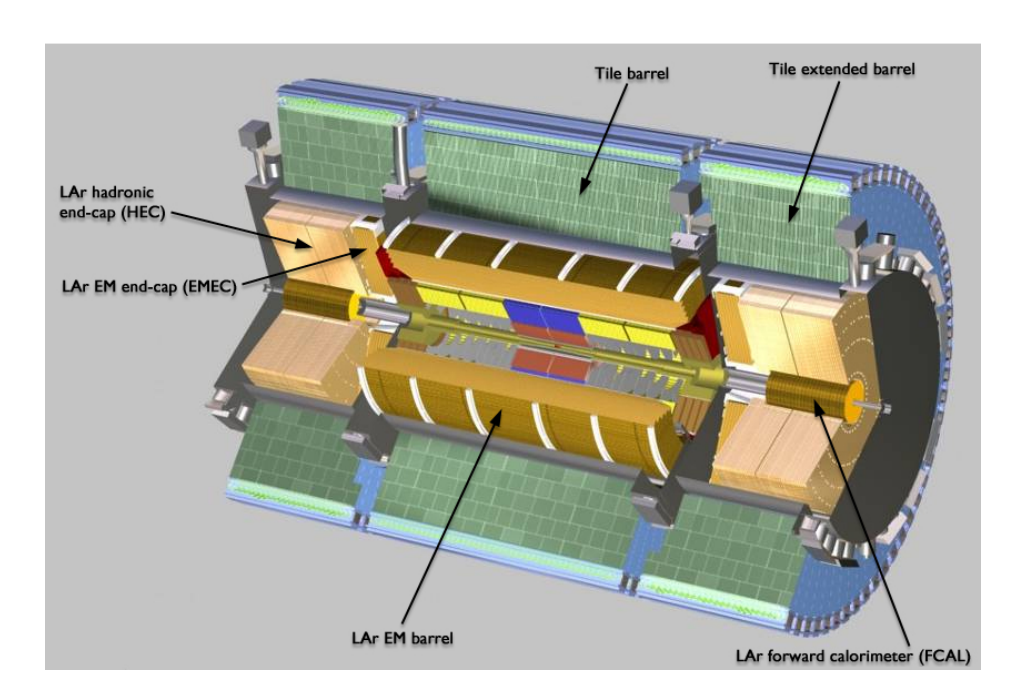


Figure 3.6. The LAr Calorimeters and the Tile Calorimeters.

Liquid Argon (LAr) Calorimeter (Electromagnetic Calorimeter (ECAL))

The Liquid Argon (LAr) Calorimeter, divided into several components, covers the pseudorapidity within $|\eta| < 3.2$. The barrel component, the electromagnetic sampling

calorimeter with 'accordion-shaped' lead electrodes, covers $|\eta| < 1.475$ with an inner radius of 2.8 m and an outer radius of 4.0 m. Two endcaps, with inner and outer disks using flat copper electrodes, cover $1.375 < |\eta| < 3.2$, and two forward calorimeters, made of copper and tungsten, are close to the beam pipe. In addition, there are presamplers which are used to correct for the energy loss occurring, in front of the LAr Calorimeter.

The LAr Calorimeter, measuring the energy of electrons and photons, is composed of layers of lead and stainless steel. The liquid argon, filled in the layers, is used to absorb electrons and photons at -185°C, and the copper grids, immersed in the liquid argon, are the electrodes. High energy electrons or photons will shower in the liquid argon to produce photons and electron-positron pairs in lower energy, respectively. Showers from low energy particles pass into liquid argon and ionize the atoms to create additional electrons and positive ions. The ionized electrons would be attracted toward the copper electrode, and the energies of traversing particles are measured from the charge deposited at the electrode. 100,000 detector channels are operated by the analog pipeline and readout system of the LAr Calorimeter [25].

Tile Calorimeter (Hadronic Calorimeter (HCAL))

The Tile Calorimeter, covering the central range $|\eta| < 1.7$, outside the LAr Calorimeter, is a cylindrical structure with an inner radius of 2,280 mm and an outer radius of 4,230 mm. It is subdivided into a 5,640 mm long central barrel, covering $|\eta| < 1.0$, and two 2,910 mm extended barrels, covering $0.8 < |\eta| < 1.7$. The large hadronic sampling calorimeter uses steel as the absorber and scintillating plates read out by wavelength shifting (WLS) fibers as the active medium. The scintillating tiles of the Tile Calorimeter are placed in planes perpendicular to the colliding beams and are staggered in depth. The thickness of the calorimeter is sufficient to stop

punch-through of hadrons into the outer muon spectrometers.

The energies of hadrons, including neutrons, protons, and mesons are measured in the Tile Calorimeter. The high energy hadrons passing through the interleaved steel interact with the atomic nuclei. Many particles would then be produced by the nuclear interactions, and induce further interactions to make showers of particles. The showered particles enter the scintillator to emit light which would be collected by optical fibers, and the energy is determined [26].

3.2.6 The Muon Spectrometers

The Muon Spectrometers (Figure 3.7), used to identify muons, are the outermost layer of the ATLAS detector. After *pp* collisions, muons are produced and pass through the Inner Detectors, the Solenoid, and the Calorimeters. Muons are minimum ionizing particles and do not shower in the calorimeters. The energy deposited in the calorimeters is small and can be neglected. While other long-lived charged particles are contained by the calorimeters, the muons traverse to reach the muon spectrometers before decaying. The muon spectrometers, portions of the ATLAS tracking systems, are used to reconstruct the tracks of muons at the outermost radii of the ATLAS detector [27].

The muon spectrometer is composed of the Monitored Drift Tube Chambers (MDT), the Cathode Strip Chambers (CSC), the Resistive Plate Chambers (RPC), and the Thin Gap Chambers (TGC). The MDT and CSC chambers have a total of 240 chambers, and 32 chambers, respectively, and are used for precision tracking. The RPC chambers in the barrel and the TGC chambers in the end caps are used for triggering. The muon chambers consist of aluminum tubes filled with Ar-CO₂ gas. The size of the aluminum tube is 3 cm in diameter. The pressure of Ar-

CO₂ gas inside is 3 bars. When muons pass through the Ar-CO₂ gas, trails of charged electrons and ions are left behind. The time taken by the charges to drift from the starting point gives the position of the muon to better than 0.1 mm [28].

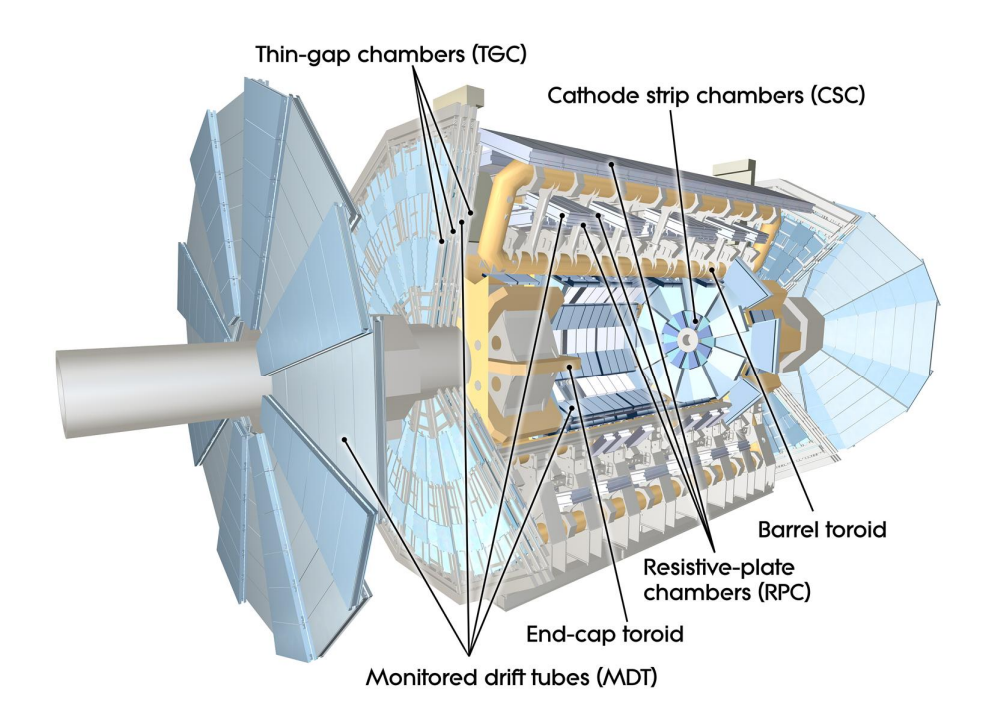


Figure 3.7. The Muon Spectrometers.

3.3 The ATLAS Trigger and Data Acquisition Systems

The LHC operations produce a peak luminosity of 10³⁴ cm⁻²s⁻¹. The rate of events produced in the LHC is up to 10⁹ interactions per second. The ATLAS Trigger and Data Acquisition systems are used to select physics processes with high efficiency while rejecting background processes. At nominal luminosity, each bunch crossing contains about 23 interactions. The event storage rate is limited to approximately 100 Hz. The ATLAS Trigger and Data Acquisition systems contain three levels of subsystems (Figure 3.8). They are the level-1

trigger (LVL1), the level-2 trigger (LVL2), and the Event Filter (EF). The LVL2 and the EF are together known as the High-Level Trigger (HLT). The ATLAS trigger system is designed to reduce the 40 MHz initial bunch crossing rate to ~200 Hz (about 300 MB/s) for offline storage and processing. The accepted rates at each level are given in Figure 3.9. The trigger selections will adapt to the changing beam conditions while preserving the interesting physics and satisfying varying detector requirements [29].

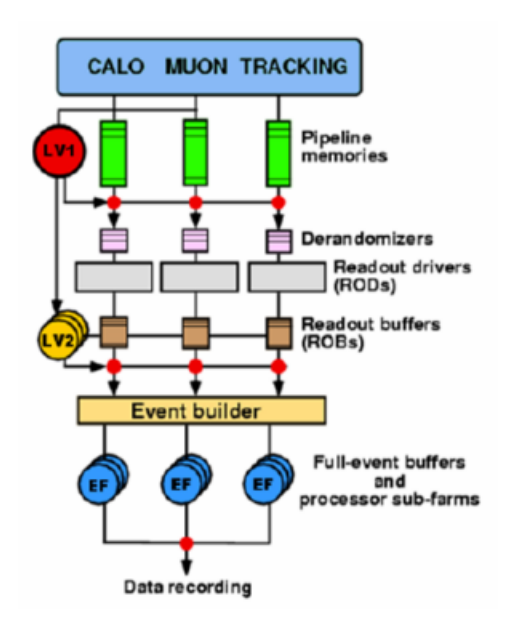


Figure 3.8. Schematic representation of the ATLAS Trigger System.

Event rate and decision stages

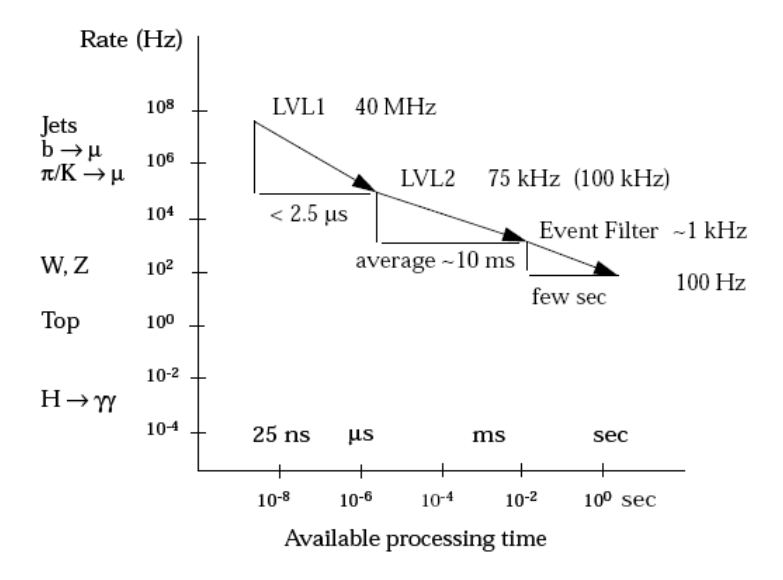


Figure 3.9. The event rates and processing times of the ATLAS trigger system.

3.3.1 The Level 1 Trigger

The LVL1 trigger, composed of electronics and firmware, receives data at the full LHC bunch-crossing rate of 40 MHz. The output rate is limited by the capabilities of the front-end systems to 75 kHz with 2.5 μ s latency. The LVL1 trigger accesses data from the calorimeter and muon chambers. The LVL1 calorimeter trigger decision is based on the multiplicities and energy thresholds of the following objects observed in the ATLAS Liquid Argon and Tile Calorimeter sub-system: Electromagnetic (EM) clusters, taus, jets, missing transverse energy (E_T), total transverse energy (E_T) in calorimeter, and total transverse energy of observed L1 jets (E_T). These objects are measured by the LVL1 algorithms using a set of trigger towers of E_T 0.1 granularity in E_T 1 granularity in E_T 2 granularity in E_T 3 granularity in E_T 4 granularity in E_T 5 granularity in E_T 6 granularity in E_T 7 granularity in E_T 8 granularity in E_T 9 granularity in E

3.3.2 The Level 2 Trigger

The LVL2 is a software algorithm that runs in large processor farms. The LVL2 combined with the EF will give a reduction factor of order 10^3 , where LVL2 is expected to provide a reduction of a factor of about 100 resulting in an input rate to the EF of the order of 1 kHz. The average execution time in the LVL2 is 10 μ s. The average processing time available for the LVL2 algorithm is 40 ms which includes the time for data transfer. During this time, the LVL2 reduces the output rate from 40 kHz to 1 kHz during startup operation, and from 75 kHz to 2 kHz during nominal operation.

The LVL 2 is software based on detector sub-regions, referred to as Regions of Interest (ROI). The full detector granularity in ROIs is used with fast tracking and calorimetry. A seed is constructed for each trigger accepted by the LVL1 that consists of a p_T threshold and an $\eta - \phi$ position. It is used to construct an ROI window around the seed position. The LVL2 algorithm uses the determined ROI to access, unpack, and analyze the associated detector in the $\eta - \phi$ position. The LVL2 algorithm is executed to compute event features for each LVL1 ROI. A coherent set of selection criteria are applied on the derived features to determine if the candidate object has passed [29].

3.3.3 The Event Filter

The EF is seeded by the LVL2 and uses the full detector granularity with potential full event access to offline algorithms. The rate of receiving is 1 kHz during the startup operation, and 2 kHz during the nominal operation. The average execution time in EF is 1 s with an output rate of 200 Hz. The accepted LVL2 signature is used to seed a sequence of EF algorithms [29].

The trigger cut on different particles is shown in Table 3.3 below which has been taken from the "Atlas level 1- Technical Design Report".

Table 3.3. Example of LVL1 trigger menu ($L = 10^{34} \text{ cm}^{-2} \text{s}^{-1}$) [30].

| Trigger | Rate (kHz) |
|--|------------|
| Single muon, $p_{\rm T} > 20~{\rm GeV}$ | 4 |
| Pair of muons, $p_{\rm T} > 6~{\rm GeV}$ | 1 |
| Single isolated EM cluster, $E_{\mathrm{T}} > 30~\mathrm{GeV}$ | 22 |
| Pair of isolated EM clusters, $E_{\mathrm{T}} > 20~\mathrm{GeV}$ | 5 |
| Single jet, $E_{\rm T}$ > 290 GeV | 0.2 |
| Three jets, $E_{\mathrm{T}} > 130~\mathrm{GeV}$ | 0.2 |
| Four jets, $E_{\Gamma} > 90 \text{ GeV}$ | 0.2 |
| Jet, E_{T} > 100 GeV AND missing E_{T} > 100 GeV | 0.5 |
| Tau, $E_{\mathrm{T}} > 60~\mathrm{GeV}$ AND missing $E_{\mathrm{T}} > 60~\mathrm{GeV}$ | 1 |
| Muon, $p_{\rm T}$ > 10 GeV AND isolated EM cluster, $E_{\rm T}$ > 15 GeV | 0.4 |
| Other triggers | 5 |
| Total | ~40 |

CHAPTER 4

OFFLINE EVENT RECONSTRUCTION AND OBJECT IDENTIFICATION

4.1 The ATLAS Offline Computing System and Data Storage

The ATLAS offline computing system uses the Athena framework [31] [32] which is installed in the Unix/Linux environment to perform data analysis. The Athena framework is constructed by ATLAS working groups. Several computing packages are built in the Athena framework. The analysis source codes, written in C++, with correlated headed files, should be compiled in the package to process the data. The additional job description codes, written in Python, are used to perform the analysis work [33].

In order to handle data in a fully distributed environment, CASTOR (CERN Advanced STORage manager), a hierarchical storage management (HSM) system, has been developed and provided by CERN. CASTOR manages disk cache(s) and the data on tertiary storage or tapes. There are by now more than 130 million files and 21 petabyte of data stored in CASTOR. From the Unix/Linux environment at CERN, files can be stored, listed, retrieved, and accessed in CASTOR [34].

Figure 4.1 shows the ATLAS computing model for how the RAW data are stored, converted, and distributed into the Grid computing system [35]. The ATLAS Grid computing system provides the facilities of distributed data management system, distributed production system, and the frameworks for distributed analysis. The Grid computing system is implemented

as sites denoted as Tier-0, Tier-1, Tier-2, and Tier-3, with different functions as depicted, in Figure 4.2. The Tier-0 server, located at CERN, is used for copying RAW data to CERN CASTOR Mass Storage System tape for archive, copying RAW data to Tier-1s for storage and subsequent reprocessing, and distributing reconstruction output (ESDs, AODs, & TAGs) to Tier-1s. There are 10 Tier-1 sites, located world-wide, used for permanently storing and taking care of a fraction of RAW data, running calibration, alignment, and reconstruction, distributing reconstruction output to Tier-2s, and keeping current versions of ESDs and AODs for analysis. There are about 70 Tier-2 sites under the distributions of Tier-1 sites, used for running analysis jobs, running simulation, and keeping AODs for analysis. Tier-3 sites, linked with Tier-2s, are for users' accessing Grid resources and local storage for end-user data, and contributing CPU cycles for simulation and analysis. The UTD cluster is one of the Tier-3 sites, linked with the Tier-2 site at UT-Arlington, and the Tier-1 site at Brookhaven National Laboratory. In order to retrieving data for analysis, the users can access datasets using the ATLAS Metadata Interface (AMI), deployed at CCIN2P3 (French Tier-1), through a web browser [36]. From the UTD HEP cluster, we use DQ2 (Don Quijote 2), the Data Management System, to query datasets, to retrieve data, and to create data selections, over the Grid. The PanDA (Production ANd Distributed Analysis) system [37], developed by an ATLAS working group, is provided for users' analysis over the Grid, so we can submit our analysis or simulation jobs to the Grid, from the UTD HEP cluster.

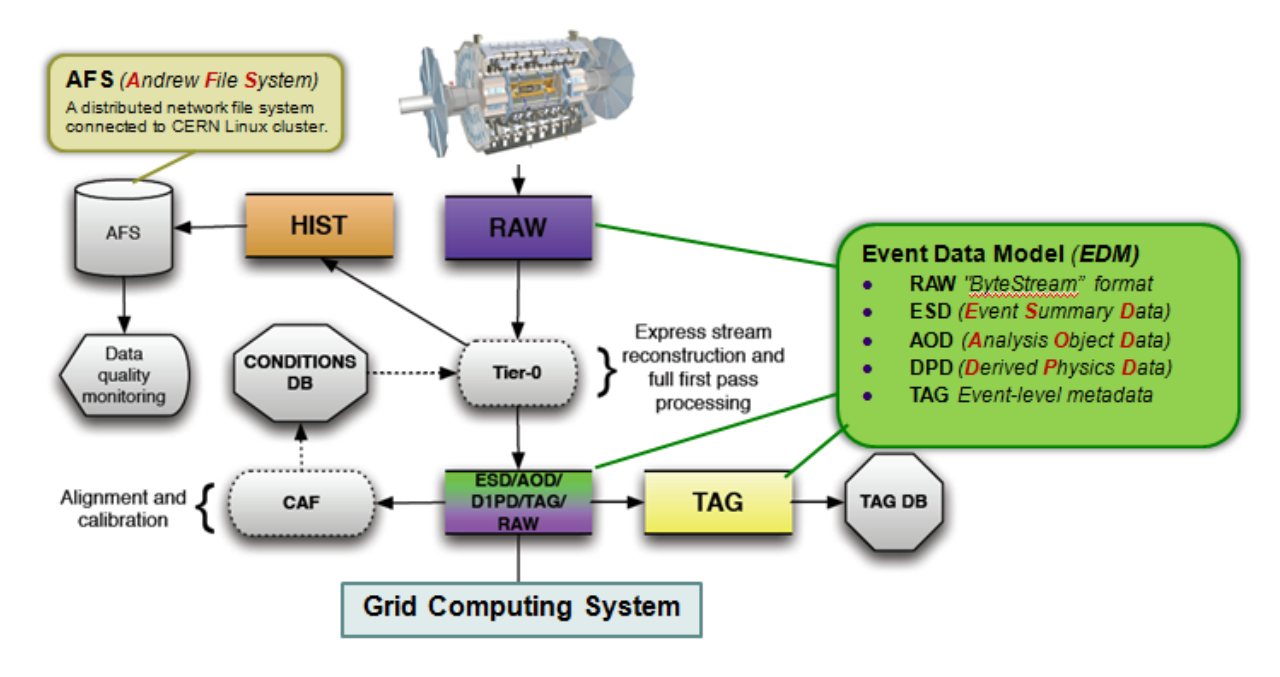


Figure 4.1. The ATLAS computing model.

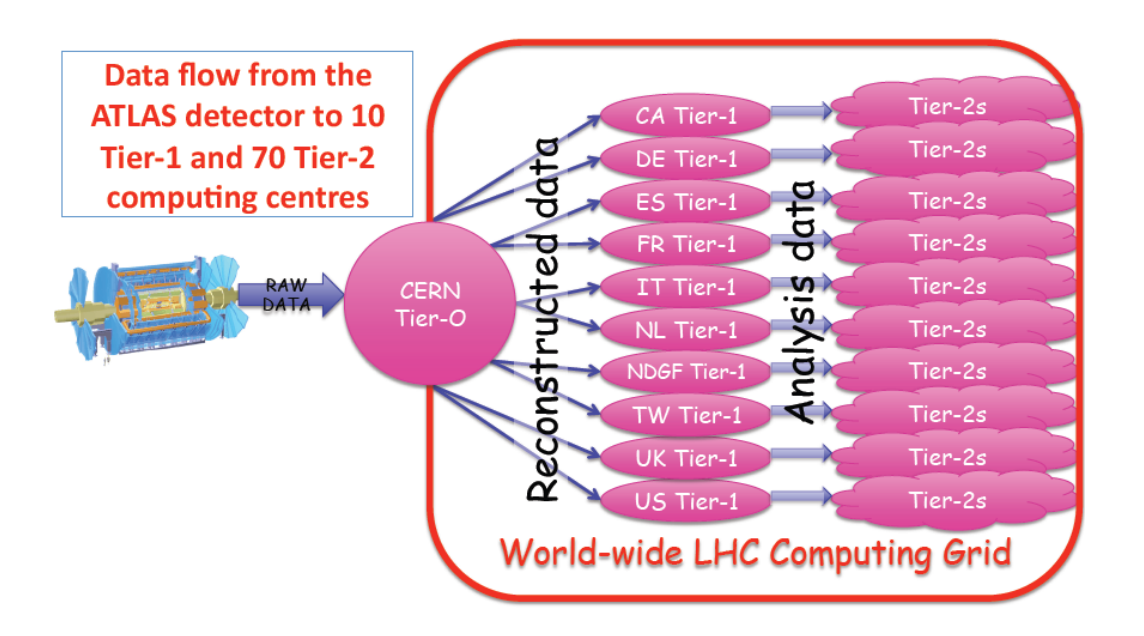


Figure 4.2. The Grid computing system in the ATLAS.

4.2 Event Reconstruction

The raw data from the ATLAS detector and Monte Carlo simulation data are produced approximately 3 PB per year. Several types of datasets and the different stages of reconstruction are established for physics analysis. The Byte-stream Data is a persistent presentation of the event data flowing from the High Level Trigger, and the Raw Data Object Data (RDO) is a C++ object representation of the byte-stream information. The Event Summary Data (ESD) contains the detailed output of the detector reconstruction and is produced from the raw data or the digitized data from simulation. Sufficient information stored in the ESD could be used for particle identification, track re-fitting, jet calibration etc., thus allowing for the rapid tuning of reconstruction algorithms and calibrations. The Analysis Object Data (AOD), storing the containers of event information, track information, Monte Carlo information, etc., is a summary of the reconstructed event, and contains sufficient information for common analyses. The AOD can be produced from the ESD for analysis, and the containers in the AOD are retrieved by the analysis codes.

Figure 4.3 illustrates the reconstruction processing pipeline which can be decomposed into several stages. The stage of data acquisition is to retrieve the raw data from the detector, as the first step in particle identification. The output of this stage, called "Reconstruction" is stored and defines the content of the ESD. The stage of analysis preparation includes the reconstruction of complex objects, and reduces the information to an acceptable size for wide distribution. The output defines the AOD content, and furthermore the event tags are created from the AOD [33].

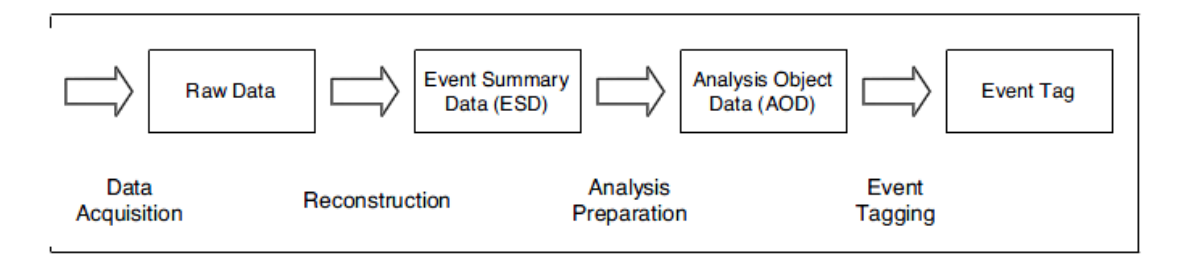


Figure 4.3. The reconstruction processing pipeline [33].

4.3 Track Measurement and Primary Vertex Reconstruction

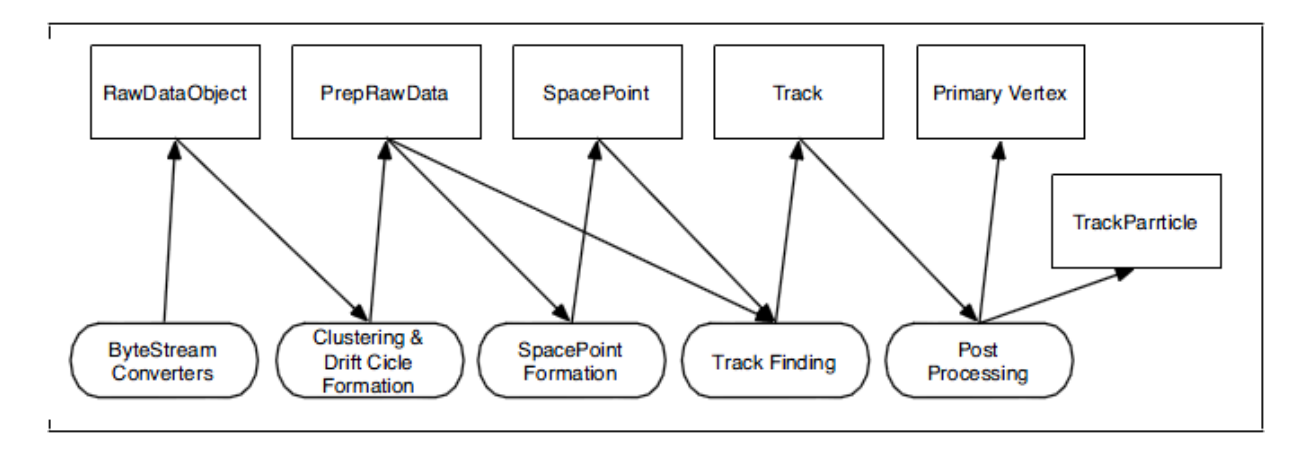


Figure 4.4. Tracking reconstruction chain. The boxes on the top represent data object, whilst the boxed on the bottom show the algorithms which work on them. The arrows show the direction of data flow [33].

The tracking systems, including the pixel detector, silicon detector, transition radiation straws, muon chambers, and drift tubes, are utilized by the common tracking software for the tracks in the Event Data Model (EDM). A common track class is instituted, and the EDM needs standard definitions of track parameters on various surfaces found along the track, and the interfaces to hit-clusters, drift circles. Tracking must handle many different coordinate frames, as a track can span the entire detector and have measurements on many different surfaces, i.e. discs, planes, cylinders, and so on. The tracking system reconstruction chain is summarized in Figure

4.4. Generalized tools allow tracking to work on both the Inner Detector and the Muon Spectrometer tracks.

Byte-stream converters take the data from the detector and form the raw data objects. These are then used to create prepared raw data (PrepRawData), i.e. clusters from the pixel detector or drift circles from the muon monitored drift tubes. The PrepRawData, along with the SpacePoints, can then be used to find tracks. Finally, the tracks can be used to find vertices, and to create the TrackParticles for physics analysis at the AOD level.

Clusters are searched for in the silicon tracker, and tracks are then searched with independent pattern recognition algorithms, sharing a number of common tools. The tracks in the silicon tracker are extrapolated and validated in the straw tracker. A dedicated algorithm examines tracks found, and keeps the one with the highest number of hits in case of duplication. A primary vertex is computed, and a set of track parameters extrapolated to the primary vertex constructed. For muon track measurement, muon track segments in the Muon Spectrometers are found from a combinatorial search of the single-station track segments. A conversion vertex is reconstructed using the pair of tracks produced by the converted candidates. Reconstruction of the conversion vertex is different from finding the primary interaction vertex, because with conversions additional constraints can be applied. The vertex fit is based on the fast-Kalman filtering method. Different robust versions of the fitting functional can also be set up in order to reduce the sensitivity to outlying measurements. The vertex fitting procedure uses the full 3D information from the input tracks including the complete error matrices.

In B-Physics Analysis Tools, two classes, named Vertex and VertexAndTracks, are extensively used in the analysis algorithms and the tools. The Vertex class is a data structure that

collects results from the vertex fit, using data members natural for analysis. The VertexAndTracks class is designed to represent a composite particle candidate, keeping the relevant reconstructed, Monte Carlo truth and genealogy information.

The Vertex class in the B-physics analysis code does not inherit from any of the ATLAS vertex classes, but instead is a simple class containing the full numerical output from the two vertexing programs, CDF and VKalVrt [38] [39] [40]. It is returned directly by the interfaces to these two fitters. In the BPhysAnalysisTools package, the CTVMFT vertex fitting algorithm, applied in the CDFVertexing class, is a FORTRAN based fitter developed by the CDF collaboration, extended by an interface to Athena. On the other hand, the VKalVrt uses Kalman filter method for the vertexing. However, VKalVrt does not yet have simultaneous multi-vertex fitting which is supported by the CDF fitter. Both the fitters are capable of complex mass, pointing, e.g. to the primary vertex, and conversion vertex type constraints. VKalVrt works with the detailed map of the ATLAS inner detector magnetic field, in contrast to the CTVMFT fitter which uses a constant field approach.

In this analysis, the CDF fitter is used to find a J/ψ candidate which is reconstructed from a $\mu^+\mu^-$ pair tracks, and the J/ψ candidate is selected in a given mass window. For finding a new particle, $X_c(3872)$ for examples, the VKalVrt fitter is used with a mass constraint for the J/ψ particle. The vertex of the $X_c(3872)$ candidate should be confirmed from the common vertex of a $\mu^+\mu^-$ pair tracks and a $\pi^+\pi^-$ pair tracks, and the invariant mass of the $X_c(3872)$ candidate is calculated from the four tracks and a given J/ψ particle mass.

4.4 Muon Reconstruction and Identification

The reconstruction of muons is based on the combined use of data from three subdetectors: Inner Detector, Calorimeters, and Muon Spectrometers. The measurement and identification of muons depends on different p_T scenarios [27] [28].

High-p_T muons, with p_T greater than 100 GeV/c, are measured by extrapolating the muon-spectrometer track inward through the calorimeters and inner tracker to the interaction point. The extrapolation of the muon trajectory to the inner-tracker track allows computation of the energy loss through the intervening material. Energy-loss parametrizations can be applied to correct the track momenta, and direct measurement of catastrophic energy loss can be used to correct muon momenta.

For muons with p_T between 6 - 100 GeV/c, momentum determination is performed by both tracker systems. The muon spectrometer provides a flag that uniquely identifies the muon. For momenta below 30 GeV/c, the measurement resolution derives mostly from the inner tracker as the muon-spectrometer resolution is dominated by multiple Coulomb scattering.

For p_T between 3 and 6 GeV/c, muons lose most energy in the calorimeters, so that they could not cross the full muon spectrometer. Muon tracks are formed in the inner tracker system and extrapolated to hit segments in the spectrometer.

CHAPTER 5

MONTE CARLO SIMULATION PRODUCTION

5.1 Monte Carlo Simulation

Monte Carlo simulation is indispensable for the ATLAS experiment. The ATLAS detector has more than 87 million readout channels, and the ATLAS trigger system is designed to reduce the 40 MHz bunch crossing rate to ~ 200 Hz for offline storage and processing. Monte Carlo simulation is critical for the studies of complicated detector performance and the trigger efficiency. For physics analysis, the study of Monte Carlo simulation is used to study the reconstruction of events, rejection of background, and to guide the real data analysis.

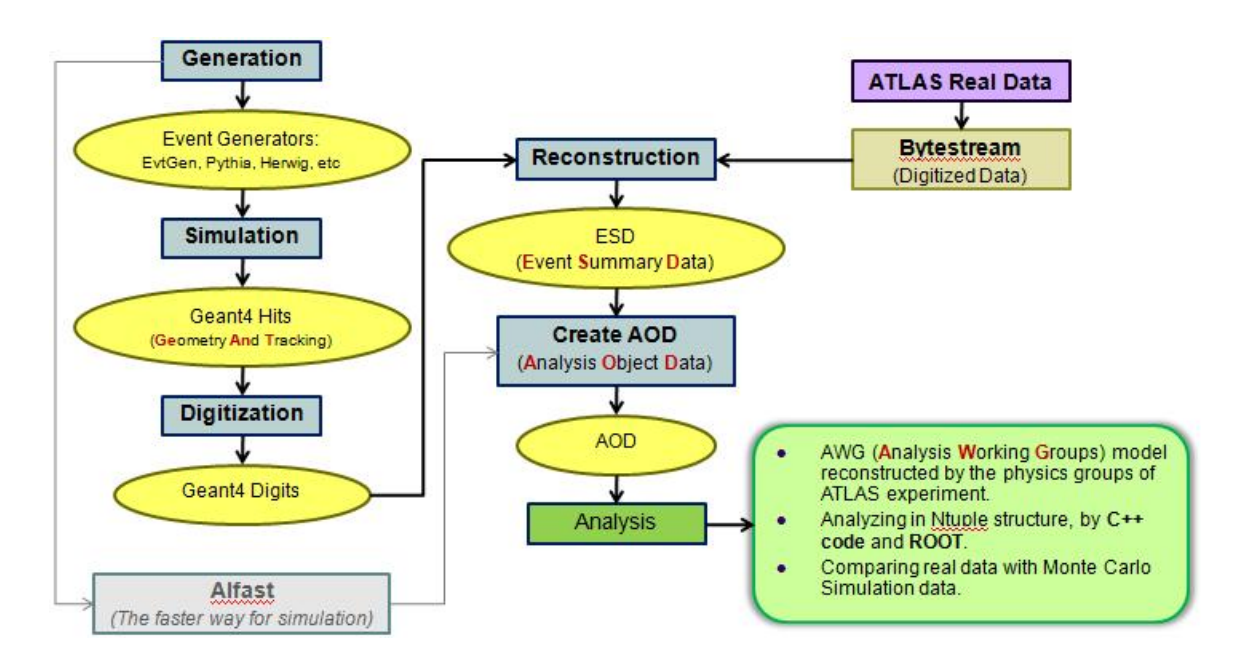


Figure 5.1. Flow-Chart of the ATLAS Full Chain Monte Carlo simulation and data analysis. Main data formats are shown as ovals, computing/conversion steps shown as rectangles.

Referring to Figure 5.1, the production and reconstruction of ATLAS Monte Carlo events are composed of several steps in a "Full Chain" simulation, from the event generation to the production of the Analysis Object Data (AOD). The simulated data would be finally reconstructed and converted into analysis ntuple data. At the generation stage, generators such as Pythia, Herwig, and EvtGen are run to produce Monte Carlo physics events. At the simulation stage, the created physics events interact with the ATLAS detector, and Geant4 (Geometry And Tracking) [41] is used to simulate the whole ATLAS detector. The detailed interactions between particles and the detector would then be digitized at the digitization stage. The data would be reconstructed at the reconstruction stage, and the ESD (Event Summary Data) files are produced. Finally, the AOD files are created from the ESD, which contain the particles and detector information for the purpose of physics analysis.

On the other hand, Atlfast provides a fast simulation of the whole chain by taking the generated events and smearing them to produce AOD files directly, without running Geant4.

5.2 The PYTHIA Program and Event Generation

The PYTHIA program [13] can be used to generate high energy physics events, i.e., sets of outgoing particles produced in the interactions between two incoming particles (*pp*). The objective is to provide as accurate as possible a representation of event properties in a wide range of reactions, within and beyond the Standard Model. This is implemented with emphasis on those events where strong interactions play a role, directly or indirectly, and therefore multihadronic final states are produced. The program is based on a combination of analytical results and various QCD-based models.

The usage of PYTHIA 6.403 for generation of heavy quarkonium events is established within the ATLAS computer framework.

The Generation of Physics Events

```
X_c(3872) \to J/\psi \pi^+ \pi^-, \ J/\psi \to \mu^+ \mu^-, \text{ is via "pp} \to gg \to c\bar{c} \ (J/\psi, \ replaced \ by \ X_c(3872)) \ g,
X_c(3872) \to J/\psi \pi^+ \pi^-, \ J/\psi \to \mu^+ \mu^-".
```

Figure 5.2 lists the job file, edited in Python, used to generate direct $X_c(3872)$ physics process using PYTHIA. By default, proton beams of 7 TeV moving in opposite directions collide to produce subsequent physics processes.

Figure 5.2. PYTHIA job file for generating direct $X_c(3872)$ events.

The common block "PYSUBS" is used for selecting the generation of processes or the combination of processes, and it is allowed to restrict the generation to specific incoming partons/particles in the hard interaction. The "MSEL" type of PYSUBS is a switch to select between full user control and some preprogrammed alternatives. The default value of MSEL type

is "1" which provides specific productions depending on incoming particles. In our case, the MSEL type is selected as "0" which leaves the opportunities of desired subprocesses to be switched on in MSUB, i.e., full user control. The "MSUB" type of PYSUBS is an array to be set to choose which subset of subprocesses to include in the generation. "ISUB" code is used in MSUB to select subprocess. If MSUB(ISUB) = 0, the subprocess is excluded. If MSUB(ISUB) = 1, the subprocess is included.

For generating quarkonium subprocesses, PYHIA provides different ways to produce the J/ψ and other hidden heavy flavors. Referring to Table 5.1, for MSEL = 0, the traditional 'color singlet' approach is encapsulated in the above processes in the range 86 – 108. Furthermore, several existing color-singlet processes are repeated in the new heavy quarkonium framework so as to provide a coherent way of defining wave function and matrix element normalizations for both singlet and octet modes. The new MSEL values which combine several quarkonium production channels together are presented in Table 5.2. A summary of all the available color singlet and color-octet production subprocesses available in PYTHIA is given in Table 5.3.

Table 5.1. Charmonium production subprocesses introduced in PYTHIA, and their corresponding ISUB subprocess numbers.

| MSEL = 0 | | | |
|----------|--|--|--|
| ISUB | subprocesses | | |
| 86 | $gg \rightarrow J/\psi g$ | | |
| 87 | $gg \rightarrow \chi_{0c} g$ | | |
| 88 | $gg \rightarrow \chi_{1c} g$ | | |
| 89 | $gg \rightarrow \chi_{2c} g$ | | |
| 104 | $gg \rightarrow \chi_{0c}$ | | |
| 105 | $gg \rightarrow \chi_{2c}$ | | |
| 106 | $gg \rightarrow J/\psi \gamma$ | | |
| 107 | $g\gamma \rightarrow J/\psi g$ | | |
| 108 | $\gamma\gamma \longrightarrow J/\psi \gamma$ | | |

| Table 5.2. New MSEL | subprocess menus | available in | PYTHIA. |
|------------------------|--------------------|--------------|---------------------|
| 1401C 3.2. INCW 1913EL | subblocess inclius | avanabic in | 1 1 1 1 1 1 1 1 1 . |

| MSEL value | Switches on | ISUB |
|------------|---------------------------|---------------------|
| 61 | all charmonim processes | 421-439 |
| 62 | all bottomonium processes | 461-479 |
| 63 | both of the above | 421-439 and 461-479 |

Table 5.3. Color-singlet/octet production subprocesses in PYTHIA 6.403, and their corresponding ISUB subprocess numbers.

| Colour-singlet/octet production in PYTHIA | | | |
|---|---|--------------------------|---|
| Charmonium subprocesses | | Bottomonium subprocesses | |
| 421 | $g+g\rightarrow c\bar{c}[^3S_1^{(1)}]+g$ | 461 | $g + g \rightarrow b\bar{b}[^{3}S_{1}^{(1)}] + g$ |
| 422 | $g+g\to c\bar{c}[{}^3S_1^{(8)}]+g$ | 462 | $g + g \rightarrow b\bar{b}[^{3}S_{1}^{(8)}] + g$ |
| 423 | $g+g \to c\bar{c}[{}^{1}S_{0}^{(8)}]+g$ | 463 | $g + g \rightarrow b\bar{b}[{}^{1}S_{0}^{(8)}] + g$ |
| 424 | $g + g \rightarrow c\bar{c}[^{3}P_{J}^{(8)}] + g$ | 464 | $g + g \rightarrow b\bar{b}[^{3}P_{J}^{(8)}] + g$ |
| 425 | $g+q \to q + c\bar{c}[{}^{3}S_{1}^{(8)}]$ | 465 | $g+q \to q + b\bar{b}[{}^3S_1^{(8)}]$ |
| 426 | $g+q \to q + c\bar{c}[{}^{1}S_{0}^{(8)}]$ | 466 | $g + q \rightarrow q + b\bar{b}[{}^{1}S_{0}^{(8)}]$ |
| 427 | $g + q \rightarrow q + c\bar{c}[^{3}P_{J_{(3)}}^{(8)}]$ | 467 | $g + q \rightarrow q + b\bar{b}[^{3}P_{J_{(3)}}^{(8)}]$ |
| 428 | $q + \bar{q} \rightarrow g + c\bar{c}[^{3}S_{1}^{(8)}]$ | 468 | $q + \bar{q} \rightarrow g + b\bar{b}[^{3}S_{1}^{(8)}]$ |
| 429 | $q + \bar{q} \rightarrow g + c\bar{c}[{}^{1}S_{0}^{(8)}]$ | 469 | $q + \bar{q} \rightarrow g + b\bar{b}[{}^{1}S_{0}^{(8)}]$ |
| 430 | $q + \bar{q} \rightarrow g + c\bar{c}[^3P_J^{(8)}]$ | 470 | $q + \bar{q} \rightarrow g + b\bar{b}[^3P_J^{(8)}]$ |
| 431 | $g + g \rightarrow c\bar{c}[^{3}P_{0}^{(1)}] + g$ | 471 | $g + g \rightarrow b\bar{b}[^{3}P_{0}^{(1)}] + g$ |
| 432 | $g + g \rightarrow c\bar{c}[^{3}P_{1}^{(1)}] + g$ | 472 | $g + g \rightarrow b\bar{b}[^{3}P_{l}^{(1)}] + g$ |
| 433 | $g + g \rightarrow c\bar{c}[^{3}P_{2}^{(1)}] + g$ | 473 | $g + g \rightarrow b\bar{b}[^{3}P_{2}^{(1)}] + g$ |
| 434 | $g + q \rightarrow q + c\bar{c}[^{3}P_{0}^{(1)}]$ | 474 | $g+q \to q + b\bar{b}[^{3}P_{0}^{(1)}]$ |
| 435 | $g + q \rightarrow q + c\bar{c}[^{3}P_{1}^{(1)}]$ | 475 | $g + q \rightarrow q + b\bar{b}[^{3}P_{1}^{(1)}]$ |
| 436 | $g+q \to q + c\bar{c}[{}^{3}P_{2}^{(1)}]$ | 476 | $g + q \rightarrow q + b\bar{b}[^{3}P_{2}^{(1)}]$ |
| 437 | $q + \bar{q} \rightarrow c\bar{c}[^{3}P_{0}^{(1)}] + g$ | 477 | $q + \bar{q} \rightarrow b\bar{b}[^{3}P_{0}^{(1)}] + g$ |
| 438 | $q + \bar{q} \rightarrow c\bar{c}[^{3}P_{1}^{(1)}] + g$ | 478 | $q + \bar{q} \rightarrow b\bar{b}[^{3}P_{1}^{(1)}] + g$ |
| 439 | $q + \bar{q} \rightarrow c\bar{c}[^{3}P_{2}^{(1)}] + g$ | 479 | $q + \bar{q} \rightarrow b\bar{b}[^{3}P_{2}^{(1)}] + g$ |

MSEL = 0 is selected, and ISUB = 86 is selected in this research. After proton-proton collisions, the gluons would be produced as the mediators, and the J/ψ particle and a single gluon are the daughters in this process. The common block "PYINT2" is used to store information necessary for efficient generation of the different subprocesses, and the "KFPR" type of PYINT2 gives the KF flavor codes for the products produced in subprocess ISUB. In this

research, the $\psi(2S)$ whose KF code is "100443" is requested to replace the J/ψ particle. The reason is that the decay modes of $X_c(3872)$ are similar to $\psi(2S)$, and so the decay channels belonging to $\psi(2S)$ can be used for $X_c(3872)$ in the PYTHIA program. The common block "PYDAT2" is used to give access to a number of flavor-treatment constants or parameters and particle/parton data. The "PMAS" type of PYDAT2 is used to set particle/parton mass m (in GeV/c^2) for compressed code KC, where KC = PYCOMP(KF). The value of the PMAS type is set at 3.872 (GeV/c^2) which is different from the $\psi(2S)$ mass of 3.686 GeV/c^2 .

The common block "PYDAT3" defines the access to particle decay data and parameters. The MDME(IDC,1) type of PYDAT3 is an on/off switch for individual decay channel IDC. In addition, a channel may be left selectively open; this has some special applications in the event generation machinery. Effective branching ratios are automatically recalculated for the decay channels left open, and process cross sections are affected. The IDC values in the range 1567 – 1577 represent the decay channels of the $\psi(2S)$. Only IDC = 1570, the $\psi(2S) \rightarrow J/\psi \pi^+\pi^-$ channel, is turned on, to mimic the desired $X_c(3872) \rightarrow J/\psi \pi^+\pi^-$ process. All other $\psi(2S)$ decay channels are turned off. The IDC values in the range 858 - 860 represent the decay channels of the J/ψ . $J/\psi \rightarrow \mu^+\mu^-$ is the desired channel, so IDC = 859 is turned on. Other decay channels of the J/ψ are off.

The events " $B^+ \to X_c(3872)K^+$, $X_c(3872) \to J/\psi \pi^+ \pi^-$, $J/\psi \to \mu^+ \mu^-$ ", are generated through " $pp \to B^+$ (via Bplus channel by using PythiaB generator), $B^+ \to X_c(3872)K^+$, $X_c(3872) \to J/\psi \pi^+ \pi^-$, $J/\psi \to \mu^+ \mu^-$ ". Figure 5.3 lists the partial PYTHIA job file for generating the $X_c(3872)$ events from the B^+ decay. The selections of the parameters are similar to those in the previous paragraphs.

```
PARAMETERS SPECIFIC TO PYTHIAB
PythiaB.ForceCDecay = "no"
# overwrite channels and close antib
include( "MC10JobOptions/MC10 PythiaB Bchannels.py" )
include( "MC10JobOptions/MC10 PythiaB CloseAntibQuarkNew.py" )
# ----- FORCE YOUR B CHANNEL HERE -----
#______
#include( "MC10JobOptions/MC10_PythiaB_CloseAntibQuark.py" )
PythiaB.ForceBDecay = "yes"
# B+ -> Xc(3872) K+, Xc -> J/psi pi+pi-, J/psi -> mu+mu-
#PythiaB.PythiaCommand += ["pydat3 mdme 932 1 1",
                           "pydat3 kfdp 932 1 100443",  # request Psi' instead of J/psi
PythiaB.PythiaCommand += ["pydat3 mdme 4651 1 1",
                          "pydat2 pmas 100443 1 3.872", # set Psi(2S) mass to 3.872 GeV
                         "pydat3 mdme 858 1 0",
                          "pydat3 mdme 860 1 0"
```

Figure 5.3. Partial PYTHIA job file for generating the $X_c(3872)$ events from the B^+ decay.

5.3 The Generator Filters and the Usage of the CKIN(3) Variable

The Generator Filters

When events are produced, the generated candidates contain energy and momentum distributions in a very wide range. The momentum directions of most events are along the longitudinal directions (beam directions). Few events contain the candidates of interest with transverse momenta that are below certain values (4 GeV/c for muons, for example).

The GeneratorFilters package is provided in the Athena framework to select events of interest. The MultiLeptonFilter can be imported in the job description files to filter energies (E),

transverse momenta (P_T), and pseudorapidities (η) of leptons. In general cases of using MultiLeptonFilter, the variable "Ptcut" (P_T cut-off) is set as 4.0 GeV/c which is the lowest transverse momentum of muon that ATLAS can detect. Events containing electrons or muons with transverse momenta greater than 4.0 GeV/c can pass the filter. Otherwise the events will not be recorded. The variable "Etacut" is used to filter pseudorapidities of leptons inside a given range. According to the geometry of barrel detector, ATLAS covers $|\eta| < 2.5$. The variable "NLeptons" is used to define the number of leptons to be filtered. When NLeptons is set as 2, events with 2 leptons (2 electrons, 2 muons, or 1 electron and 1 muon) passing the filter criteria will be recorded.

When the filter criteria are given, the generated events will be sifted by the event filter. The rate of events passing the filter depends on individual physics processes. For most of our Monte Carlo production, there are 2 muons to be filtered, and the criterion is to select both muons with transverse momenta greater than 4.0 GeV/c.

The Usage of the CKIN(3) Variable

In order to facilitate Monte Carlo simulation studies, some tools are designed into the PYTHIA program. The "CKIN" array of common block PYSUBS provides the kinematics cuts that affect the region of phase space within which events are generated. The CKIN(3) type is used to set the minimum p_T value for hard process, and the CKIN(4) type is used to set the maximum p_T value for hard process. The usage of CKIN(3) can provide particles with a higher transverse monenta distribution. It helps to produce more effective signal samples in Monte Carlo production and to save computing time. However, higher p_T distributions in hard process can induce a bias during the interaction. The higher CKIN(3) value setting, would produce

muons with higher transverse momenta, leading to higher filtering efficiency. The study of CKIN(3) with Generator Filters for the physics processes helps us design suitable Monte Carlo simulation criteria. Figure 5.4 shows the example of adapting CKIN(3) with minimum p_T value as 10.0 GeV/c.

```
include( "MC10JobOptions/MC10_PythiaB_Btune.py" )
PythiaB.PythiaCommand += ["pysubs ckin 3 10.",
                      "pysubs ckin 9 -3.5",
                      "pysubs ckin 10 3.5",
                      "pysubs ckin 11 -3.5",
                     "pysubs ckin 12 3.5",
                     "pysubs msel 1"]
      ----- DEFINE SELECTION CUTS -----
  ----- Selections on b quarks -----
# simulate only b-flavour events
PythiaB.flavour = 5.
PythiaB force exclusive decay channels only on b=-5 side
 ----- b=5 --- and/or --- b=-5 -----
PythiaB.cutbq = ["0. 102.5 and 8. 2.5"]
 ----- LVL1 muon cuts 0=OFF 1=ON ------
PythiaB.lvl1cut = [ 1., 4., 2.5]
       ------ LVL2 muon/electron cuts 0=OFF 1=ON------
PythiaB.lvl2cut = [ 0., 13., 4., 2.5]
#PythiaB.lv12cut = { 0., 11.,
                                 2.5};
                             6..
 ----- Offline cuts 0=OFF 1=ON -----
PythiaB.offcut = [ 1., 0.5, 2.5, 4., 2.5, 0.5, 2.5]
     ----- Number of repeated hadronization mhadr --
# End of job options file
.
```

Figure 5.4. Example PYTHIA codes for applying kinematics cuts.

5.4 Monte Carlo Samples

Several samples of interactions involving the $X_c(3872)$ particle and the charmonium-like states have been produced by the ATLAS collaboration at UTD's request. The official Monte Carlo datasets were first produced in January, 2009, and the Monte Carlo datasets are available on the Grid computing server. Table 5.4 lists the available signal channel samples for our research.

Table 5.4. Signal samples of ATLAS Monte Carlo events.

| Dun ann Mann | Dataset | CKIN3 | Filter | C4-4:-4: | |
|--------------------------------------|---------|---------|------------|------------|--|
| Process Name | No. | (GeV/c) | Efficiency | Statistics | |
| PythiaB_Bplus_XcK_Jpsipipi_mu4mu4 | 108514 | 10 | N/A | 50 k | |
| Pythia_Psi2S_Jsipipi_mu0mu0 | 108529 | 1 | 0.74 | 5 M | |
| Pythia_Xc_Jpsipipi_mu4mu4 | 108545 | 10 | 0.13473 | 50 k | |
| PythiaB_Bplus_Psi2SK_Jpsipipi_mu4mu4 | 108546 | 10 | N/A | 50 k | |

Besides the signal channel samples, background Monte Carlo events are also provided by the ATLAS group. Table 5.5 lists the available background samples of ATLAS Monte Carlo events. The study of background rejection will be based on these samples. The direct J/ψ channel, direct bb channel, and Drell-Yan process are the most important background physics processes for our study.

Table 5.5. Background samples of ATLAS Monte Carlo events.

| Duo agga Nama | Dataset | CKIN3 | Filter | Statistics |
|-------------------------------|---------|---------|------------|------------|
| Process Name | No. | (GeV/c) | Efficiency | Statistics |
| Pythia_directJpsimu4mu4 | 108536 | 1 | 0.0004 | 5 M |
| PythiaB_bbmu4mu4X | 108488 | 12 | N/A | 2 M |
| Pythia_DYLowBPhysM_mu2p5mu2p5 | 108441 | N/A | 0.016 | 500 k |
| Pythia_directJpsimu2p5mu2p5 | 108494 | 1 | 0.0030677 | 1 M |
| Pythia_directJpsimu0mu0 | 108496 | 1 | 0.237 | 5 M |
| PythiaB_bbmu2p5mu2p5X | 108490 | 8 | N/A | 6 M |
| PythiaB_bbmu0mu0X | 108500 | 5 | N/A | 200 k |

CHAPTER 6

ANALYSIS METHODS AND USER PROGRAM

6.1 The Athena Framework and Data Analysis Packages

Athena [31] [32] is a C++ control framework in which data processing and analysis are performed. It is a concrete implementation of an underlying architecture called the Gaudi project which was originally developed by the LHCb collaboration. The Gaudi project is a kernel of software common to both experiments and co-developed, while Athena is the sum of this kernel plus ATLAS-specific enhancements.

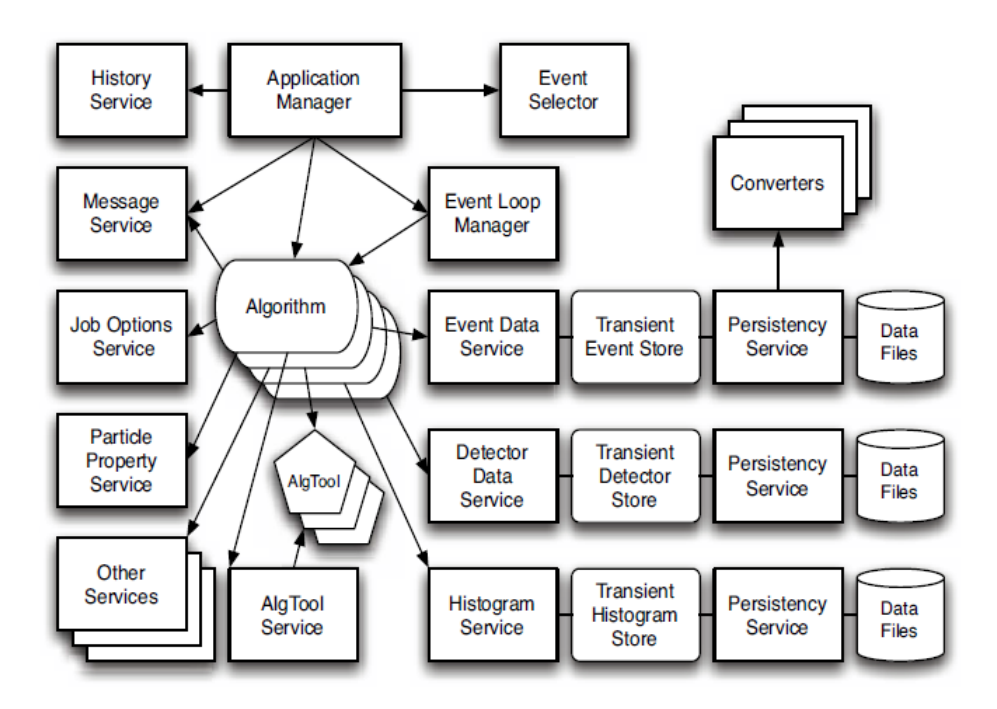


Figure 6.1. The Athena component model [31].

The major components that have been identified within the architecture are shown in Figure 6.1. This shows component instances and their relationships in terms of navigability and usage. The application manager in the Athena framework is the overall driving intelligence that manages and coordinates the activity of all other components within the application. About the algorithms, they share a common interface and provide the basic per-event processing capability of the framework, and implement methods for invocation by the framework, such as *initialize()*, *execute()*, *beginRun()*, *endRun()*, and *finalize()*. Each algorithm performs a well-defined but configurable operation on some input data, in many cases producing some output data. A Sequencer is a sequence of algorithms, each of which might itself be another Sequencer, allowing for a tree structure of processing elements. A filter algorithm can indicate that the event being processed fails to meet its filter criteria and inhibit the processing of downstream algorithms.

The ATLAS software is organized into a hierarchical structure of projects and packages. Most packages shown in the hierarchy are "container" packages used for structuring the software and managing versions in releases. The layout of each package can be organized into several sub-directories, including the "src" directory which contains the C++ source files, the "<PackageName>" directory which contains the C++ header files, and the "cmt" directory which contains requirements and setup files. The packages are subdivided into decades of sub-packages, listed below:

- Generators, Simulation, Trigger, Reconstruction, PhysicsAnalysis
- InnerDetectorSoftware, MuonSoftware, LArCalorimeter, TileCalorimeter
- CommonTrackingSoftware, Calorimeter

- Control, DataBase, DetectorDescription, Monitoring, MagneticField
- AtlasSettings, AtlasRelease, AtlasPolicy, AtlasCxxPolicy, AtlasTest, Tools, Utilities
- External

For B-Physics analysis, there are five software packages developed and maintained by the B-Physics group. The "BPhysAnalysisObjects" package contains utility classes for constructing analyses. The "BCompositeParticle" class, which is one of the major classes in this package for particle implementation, represents any particle found in the analysis that has not left a track in the detector, and contains methods for accessing quantities. The "BPhyAnalysisTools" package contains a set of tools for constructing analyses and doing vertexing. The interfaces to the vertexing programs are found inside, and the tools are provided for finding particular decays. The "BPhysToolBox", of this package, contains a range of methods for calculating variables, manipulating objects, and extracting information from the Monte Carlo truth. The "BPhysExamples" package provides several examples showing how the different tools can be used. The analyzer can modify them to analyze specific physics processes. The "BPhysAlgs" package is a repository for completed physics analysis algorithms used for producing results. The algorithms are accompanied by the ROOT scripts to read the output of the code. The "BPhysAnalysisSkeleton" package provides the "BSkeleton" algorithm which the analyzer can use as a basis for a specific analysis. The "JpsiUpsilonAlgs" package provides the algorithms dedicated for I/ψ , Y, and quakonia analysis.

6.2 Reconstruction of the $X_c(m) \rightarrow J/\psi \pi^+ \pi^-$ Events

The observed $X_c(m) \to J/\psi \pi^+ \pi^-$, $J/\psi \to \mu^+ \mu^-$ is one of the interesting physics processes in our research. Figure 6.2 lists the code for analyzing the $X_c(m)$ decays. For Monte Carlo $X_c(m)$ events, a $X_c(m)$ candidate can be produced directly or be the descendent particle from a heavier particle, such as the B^+ and B_s^0 . The "decayTopology" variable is a vector variable containing integer information which represents the PDG_ID code of particle. The $X_c(m)$ decay structure is imported, and the whole topology would be used to find the truth particles and signal tracks in containers. The "getSignalTracks(decayTopology)" function which is built in the "BPhysToolBox.cxx" source code in "BPhyAnalysisTools" package is used to find the final state tracks originating from a decay. It returns final state tracks, according to entered PDG_ID codes, to the "signalTracksHolder" variable. The "getSignalParticles(decayTopology)" function which is built in the "BPhysToolBox.cxx" source code in the "BPhyAnalysisTools" package is used to find the Monte Carlo truth particles originating from decay. It returns the "HepMC GenParticles", according to entered PDG_ID codes, to the "trueParticlesHolder" variable.

The analysis code contains the algorithms to retrieve track particles, muons, truth particles, and primary vertex information from the StoreGate, before finding signal events in the Monte Carlo truth and reconstructing candidate from tracks information. Once the necessary PDG_ID codes are imported, the Monte Carlo truth information would be identified and recorded in loop structure algorithms. For analyzing the $X_c(m)$ decay process, a total of six truth entries should be completely recorded. Furthermore, the physics properties which are accommodated to each truth particle could be retrieved simultaneously. Table 6.1 lists the codes of accessing physics properties for truth particles.

```
// Set the signal decay topology
decayTopology.push back(100443);
decayTopology.push_back(443); decayTopology.push_back(13); decayTopology.push_back(-13);
decayTopology.push_back(211); decayTopology.push_back(-211);
// Find the final state tracks orginating from this decay
signalTracksHolder = myBPhysToolBox.getSignalTracks(decayTopology);
// Find the HepMC::GenParticles originating from this decay
trueParticlesHolder = myBPhysToolBox.getSignalParticles(decayTopology);
if (trueParticlesHolder.size()==1) {
 if (trueParticlesHolder[0].size()==6) {
   foundSignalEventInTruth = true;
   ++truthEventCntr;
    for (truePtclItr=trueParticlesHolder[0].begin();
        truePtclItr!=trueParticlesHolder[0].end(); ++truePtclItr) {
     if ((*truePtclItr)->pdg_id() == 100443) yc = (*truePtclItr);
     if ((*truePtclItr)->pdg_id() == 443) jpsi = (*truePtclItr);
     if ((*truePtclItr)->pdg_id() == 13) muMinus = (*truePtclItr);
     if ((*truePtclItr)->pdg_id() == -13) muPlus = (*truePtclItr);
     if ((*truePtclItr)->pdg id() == 321) PiPlus = (*truePtclItr);
     if ((*truePtclItr)->pdg_id() == -321) PiMinus = (*truePtclItr);
} else {
 log << MSG::WARNING << "Truth record contains " << trueParticlesHolder.size()
     << " signal processes. Skipping event." << endreq;
  return StatusCode::SUCCESS;
```

Figure 6.2. Analysis codes for finding Monte Carlo truth information in the $X_c(m)$ events.

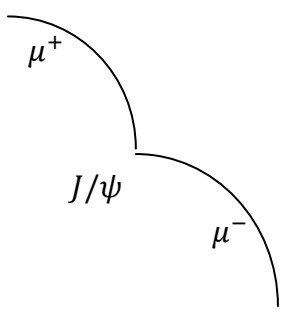
Table 6.1. Code list of accessing truth particles.

| Codes | Physics Properties |
|--|---|
| (*truePtclItr)->momentum().pseudoRapidity(); | pseudorapidity |
| (*truePtclItr)->momentum().phi(); | azimuthal angle |
| (*truePtclItr)->momentum().e(); | energy |
| (*truePtclItr)->momentum().px(); | component of momentum along x direction |
| (*truePtclItr)->momentum().py(); | component of momentum along y direction |
| (*truePtclItr)->momentum().pz(); | component of momentum along z direction |
| (*truePtclItr)->momentum().perp(); | transverse momentum |

The physics properties associated to tracks and reconstructed candidates can be accessed from the vertexing programs which are returned through the BPhysics interfaces. The quantities

can be calculated by vertexing algorithms and the composite particle is able to hold these vertices alongside the objects that made it. The information from the composite particle includes the mass as calculated at the vertexer, and the kinematic quantities calculated from the 'refitted' track parameters. The methods to access these quantities are listed below:

- refittedMass()
- refittedPx()
- refittedPy()
- refittedPz()
- refittedPt()
- refittedE()
- refittedPseudorapidity()

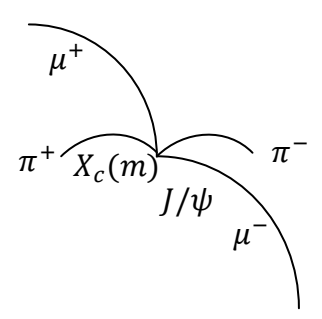


The J/ψ particle is reconstructed in its decay to $\mu^+\mu^-$. The charged muons (μ^+ and μ^-) are detected and identified by the inner detectors (ID) and the associated muon subdetector hits of the ID charge tracks. The momenta of muons are measured and the sign of charge of each muon is identified by the inner detectors. The inner detectors include the pixel detector, the semiconductor tracker (SCT), and the transition radiation tracker (TRT). The x, y, and z

components of the μ^{\pm} momenta are determined from fits to the hits associated with the μ^{\pm} tracks inside ID. For a pair of muons, μ^{+} and μ^{-} , they share a common vertex. The common vertex of muons is reconstructed from tracks provided by the inner detectors, and the J/ψ candidate is inferred. The momentum of each J/ψ candidate is then determined as the sum of the momenta of the $\mu^{+}\mu^{-}$ pair, assuming the muons are from the pp interaction point. Using the PDG value for the μ^{\pm} mass, the total energies of the muons are calculated. The energy of each J/ψ candidate is the summation of the μ^{+} energy and the μ^{-} energy. The invariant mass of the J/ψ candidate can be calculated as follows.

$$\begin{split} p_{x(\mu^{\pm})} &= p_{T(\mu^{\pm})} \cos \varphi_{(\mu^{\pm})} &\quad (\varphi_{(\mu^{\pm})} \text{ is the azimuthal angle}) \\ p_{y(\mu^{\pm})} &= p_{T(\mu^{\pm})} \sin \varphi_{(\mu^{\pm})} \\ p_{z(\mu^{\pm})} &= p_{T(\mu^{\pm})} \cot \theta_{(\mu^{\pm})} &\quad (\theta_{(\mu^{\pm})} \text{ is the polar angle}) \\ p_{x(J/\psi)} &= p_{x(\mu^{+})} + p_{x(\mu^{-})} \\ p_{y(J/\psi)} &= p_{y(\mu^{+})} + p_{y(\mu^{-})} \\ p_{z(J/\psi)} &= p_{z(\mu^{+})} + p_{z(\mu^{-})} \\ p_{(J/\psi)} &= \sqrt{p_{x(J/\psi)}^{2} + p_{y(J/\psi)}^{2} + p_{z(J/\psi)}^{2}} \\ E_{(\mu^{\pm})} &= \sqrt{p_{(\mu^{\pm})}^{2} + m_{(\mu^{\pm})}^{2}} \\ E_{(J/\psi)} &= E_{(\mu^{+})} + E_{(\mu^{-})} \\ m_{(\mu^{+}\mu^{-})} &= \sqrt{E_{(J/\psi)}^{2} - p_{(J/\psi)}^{2}} \end{split}$$

Comparing with the PDG value of the J/ψ mass, which is 3096.916 MeV/c², and a given window, the events of invariant masses locating in the mass window are regarded as the J/ψ candidates.



The $X_c(m)$ events are reconstructed via $X_c(m) \to J/\psi \pi^+ \pi^-$ decay. The life time of the J/ψ is very short. It decays immediately without traveling in the detector. The two muon tracks and the two pion tracks share a common vertex, and the $X_c(m)$ candidate can be reconstructed from the four tracks. The mass of the J/ψ is constrained during this calculation. The energy of each $X_c(m)$ candidate is the summation of J/ψ energy, which is μ^+ energy plus μ^- energy, π^+ energy, and π^- energy. The invariant mass of the $X_c(m)$ candidate can be calculated as $J/\psi \pi^+\pi^-$ mass, as follows.

$$\begin{split} p_{x(X_{c}(m))} &= p_{x(\mu^{+})} + p_{x(\mu^{-})} + p_{x(\pi^{+})} + p_{x(\pi^{-})} \\ p_{y(X_{c}(m))} &= p_{y(\mu^{+})} + p_{y(\mu^{-})} + p_{y(\pi^{+})} + p_{y(\pi^{-})} \\ p_{z(X_{c}(m))} &= p_{z(\mu^{+})} + p_{z(\mu^{-})} + p_{z(\pi^{+})} + p_{z(\pi^{-})} \\ p_{(X_{c}(m))} &= \sqrt{p_{x(X_{c}(m))}^{2} + p_{y(X_{c}(m))}^{2} + p_{z(X_{c}(m))}^{2}} \end{split}$$

$$\begin{split} E_{(\pi^{\pm})} &= \sqrt{p_{(\pi^{\pm})}^2 + m_{(\pi^{\pm})}^2} \\ E_{(X_c(m))} &= E_{(J/\psi)} + E_{(\pi^+)} + E_{(\pi^-)} \\ m_{(J/\psi\pi^+\pi^-)} &= \sqrt{E_{(X_c(m))}^2 - p_{(X_c(m))}^2} \end{split}$$

Four tracks are fitted to a common vertex, and the J/ψ mass is constrained at the PDG value. The fitted vertex indicates a $X_c(m)$ candidate, and the physics properties of the $X_c(m)$ candidate can be retrieved. The calculated mass distribution of $X_c(m)$ candidates is then fitted by a Gaussian function with a polynomial function representing the background, and the invariant masses located in a given mass window are regarded as the $X_c(m)$ candidates.

6.3 Background Suppression

Background rejection is important for this analysis. The reconstruction of Monte Carlo events needs to be combined with background information for simulating real data. The expected sources of background for prompt charmonium with a di-muon μ4μ4 trigger are:

- Direct J/ψ production
- Indirect I/ψ production from beauty decays
- Continuum of muon pairs from beauty decays
- Continuum of muon pairs from charm decays
- Di-muon production via the Drell-Yan process
- Decays in flight of π^{\pm} and K^{\pm} mesons

In our research, the dominant background sources are continuum of muon pairs from decays of beauty decays, direct J/ψ production, and di-muon production via the Drell-Yan process. Contributions from charm decays have not been simulated, but despite having an estimated total rate twice as high as from beauty for a $\mu 4\mu 4$ trigger, the p_T distribution of muons from charm quarks falls more steeply, and so charm events are expected to contribute at a lower level than beauty. Only a small fraction of the Drell-Yan pairs survive the di-muon trigger cuts of $\mu 4\mu 4$ in the interested mass range, which makes this background essentially negligible. Muons from decays in flight also have a steeply falling muon momentum spectrum, and in addition require random coincidences with muons from other sources in the quarkonium invariant mass range. This is estimated to be at the level of a few percent of the signal rate, spread over a continuum of invariant masses.

CHAPTER 7

MONTE CARLO STUDY OF $X_c(3872)$ EVENTS

The official Monte Carlo samples of signals and backgrounds as described in Chapter 5 are ported to the UTD HEP cluster. The analysis packages, initially developed by the ATLAS B-Physics group and modified for this research, are built on the UTD machine. The analysis codes are modified for reconstructing interesting physics processes. The Monte Carlo events $"X_c(3872) \rightarrow J/\psi \pi^+ \pi^-, J/\psi \rightarrow \mu^+ \mu^-"$, where the $X_c(3872)$ is produced via direct $pp \rightarrow X_c(3872)$ or $B^+ \rightarrow X_c(3872)K^+$ interactions, are studied, respectively. The fitted mass values of the reconstructed Monte Carlo $X_c(3872)$ signals are consistent with the input value of 3.872 GeV/c² set in the simulation. The rms spread of the fitted mass is 11.7 MeV/c² with a χ^2 /dof value 2.456. The simulated transverse momenta, pseudo-rapidity, and the reconstruction efficiency of the muons, the pions, the J/ψ , and the $X_c(3872)$ particles, are examined. The systematic errors of the reconstructed particles, and the Monte Carlo truth matching to the reconstructed particles, are studied.

7.1 Event Generation and Filter Efficiency

The official ATLAS Monte Carlo samples used in this dissertation have been requested by UTD and produced by the ATLAS collaboration. The details of the event generation and the filtering of the direct $pp \to X_c(3872)$ and $B^+ \to X_c(3872)K^+$ samples are described in this section.

Generation of direct $pp \rightarrow X_c(3872)$ sample:

```
MetaData: cross-section (nb) = 0.723352
GenFilter::finalize()
Events passed = 5000
                        Events Failed = 32569
                                     BSignalFilter Summary Report
  LV11 muon trigger report:
        pT cut
                                                                 4000 MeV
         Pseudo-rapidity cut
         No of events containing at least
         one particle satisfying these cuts
                                                                           26869
  LV12 muon trigger report:
                                                                4000 MeV
        Muon pT cut
        Muon pseudo-rapidity cut
                                                                I
         No of events containing at least one muon satisfying LVL1 cut
         and at least one separate particle passing these LVL2 cuts
                                                                      37569
   Total no of input events
   No of events rejected by trigger
                                                                           32569
   No of events rejected in total
                                                                           32569
  To obtain correct cross section, multiply BX in PythiaB report by
                                                                                 0.133088
                                          ===End of report==
>>> TestHepMC from finalize
   Events passed = 37569
                            Events Failed = 0
>>> CountHepMC from finalize
    Events passing all checks and written = 5000
```

Figure 7.1. Log record of the direct $pp \to X_c(3872)$ event generation (1st sub-job).

Table 7.1. Number of events and filter efficiencies of the direct $pp \to X_c(3872)$ event generation.

| sub-jobs | 1 st | 2 nd | 3 rd | 4 th | 5 th | 6 th | 7^{th} | 8 th | 9 th | 10 th |
|---------------------------|-----------------|-----------------|-----------------|-----------------|-----------------|-----------------|-----------------|-----------------|-----------------|------------------|
| Cross- Section (nb) | 0.7233 | 0.7196 | 0.7190 | 0.7201 | 0.7226 | 0.7198 | 0.7196 | 0.7218 | 0.7222 | 0.7192 |
| Generated Events | 37569 | 36676 | 36179 | 36733 | 36040 | 36584 | 36890 | 37482 | 35902 | 35968 |
| Filtered Events | 5000 | 5000 | 5000 | 5000 | 5000 | 5000 | 5000 | 5000 | 5000 | 5000 |
| Filter Efficiency | 0.1331 | 0.1363 | 0.1382 | 0.1361 | 0.1387 | 0.1367 | 0.1355 | 0.1334 | 0.1393 | 0.1390 |

The event production was performed with 10 sub-jobs, with 5,000 events passing the filter criteria for simulation in each sub-job, and 50,000 events in total. Figure 7.1 shows the log record of the event generation of the first sub-job for the direct $pp \rightarrow X_c(3872)$ sample. In this sub-job, 37,569 physics events were produced. The LVL1 muon trigger is used for selecting one muon truth particle with $p_T > 4.0$ GeV/c and $|\eta| < 2.5$ in each event, and 26,869 events passing the first filter (LVL1). The LVL2 muon trigger is then used for selecting the second muon truth

particle with $p_T > 4.0$ GeV/c and $|\eta| < 2.5$ in each event, and 5,000 events finally passing the second filter. The filter efficiency in this sub-job is 0.133 (5,000 / 37,569). The cross-section of the direct $pp \to X_c(3872)$ process in this sub-job is 0.723352 (nb), and the estimated $X_c(3872) \to J/\psi \pi^+ \pi^-, J/\psi \to \mu^+ \mu^-$ cross-section is 0.723352 × BR($X_c(3872) \to J/\psi \pi^+ \pi^-$) (unknown) × 0.0593 (BR($J/\psi \to \mu^+ \mu^-$)). Table 7.1 lists the statistics of the 10 sub-jobs. The total generated number of physics events is 366,023, and the total number of events passing the filters is 50,000. The overall filtering efficiency is 0.137.

Generation of $B^+ \to X_c(3872)K^+$ sample:

```
CROSSSECTION OF YOUR B-CHANNEL IS BX= PX*NB/AC/MHAD=
IN CASE YOU FORCED ANY DECAY YOU SHOULD CORRECT CROSS
SECTION BX FURTHER, MULTIPLYING BX BY BRANCHING RATIO(S)
OF YOUR FORCED DECAY(S) AND BY A FACTOR OF 2 FOR SYMMETRY
MORE DETAILS ON CROSS SECTION
PYTHIA MSEL=1
                 CROSS SECTION IS
                                                              3.63613 mbarn
          ACCEPTED MSEL=1 EVENTS
                                      AC=
NUMBER OF
                                                              13168861
           ACCEPTED
                       B-EVENTS
REPEATED HADRONIZATIONS IN EACH EVENT MHAD=
                                                              1.001
AVERAGE NUM OF ACCEPTED EVTS IN HADRONIZATION LOOP
        YOUR MAIN SIMULATION PARAMETERS AND CUTS
HARD SCATTERING CUT pysubs().ckin(3)
STRUCTURE FCN (1=CTEQ3 7=CTEQ5) pypars().mstp(51)
                                                              20650
CUTS ON b and/or anti b QUARK
                                                              0; 102.5; and; 8; 2.5
LVL1 MUON CUTS:
                                                              4; 2.5
LVL2 CUTS:
                   ON(1)/OFF(0); PARTICLE-ID;
                                              PT AND ETA
CUTS FOR STABLE PARTICLES IN B-DECAY:
                                              ON(1)/OFF(0) I
                                                              0.5;
 CHARGED HADRONS:
                                              PT AND ETA
                                                              4; 2.5
0.5; 2.5
 MUONS:
 ELECTRONS:
                                              PT AND ETA
```

Figure 7.2. Log record of the $B^+ \to X_c(3872)K^+$ event generation (1st sub-job).

The event production was performed with 10 sub-jobs, with 5,000 (± 1) events passing the filter criteria for simulation in each sub-job, and 50,005 events in total. Figure 7.2 shows an example of the event generation log record of the first sub-job of the $B^+ \to X_c(3872)K^+$ sample. In this sub-job, 13,168,861 events were produced. The LVL1 muon trigger is used for selecting one muon truth particle with $p_T > 4.0$ GeV/c and $|\eta| < 2.5$, and the LVL2 muon trigger is used

for selecting the second muon truth particle with $p_T > 4.0$ GeV/c and $|\eta| < 2.5$, in each event. Additional filter is applied for selecting charged hadrons, i.e. pion and kaons, with $p_T > 0.5$ GeV/c and $|\eta| < 2.5$. 5,000 events finally pass the whole filters. The filter efficiency in this subjob is 0.00038 (5,000 / 13,168,861). The cross-section of the $B^+ \to X_c(3872)K^+$ process in this sub-job is 1,380.58 (nb), and the estimated $X_c(3872) \to J/\psi \pi^+ \pi^-$, $J/\psi \to \mu^+ \mu^-$ cross-section is 1,380.58 × 2 × BR($B^+ \to X_c(3872)K^+$) (unknown) × BR($X_c(3872) \to J/\psi \pi^+ \pi^-$) (unknown) × 0.0593 (BR($J/\psi \to \mu^+ \mu^-$)). Table 7.2 lists the statistic results of the 10 sub-jobs. The total generated number of events is 132,750,751, and the total number of events passing filter is 50,005. The overall filtering efficiency is 0.000377.

Table 7.2. Number of events and filter efficiencies of the $B^+ \to X_c(3872)K^+$ event generation.

| sub-jobs | 1 st | 2 nd | 3 rd | 4 th | 5 th |
|--------------------|-----------------|-----------------|-----------------|-----------------|-----------------|
| Cross-Section (nb) | 1380.58 | 1360.57 | 1372.39 | 1373.59 | 1361.99 |
| Generated Events | 13168861 | 13366305 | 13248217 | 13236998 | 13348333 |
| Filtered Events | 5000 | 5000 | 5000 | 5000 | 5000 |
| Filter Efficiency | 0.000380 | 0.000374 | 0.000377 | 0.000378 | 0.000375 |

| sub-jobs | 6 th | 7 th | 8 th | 9 th | 10^{th} |
|--------------------|-----------------|-----------------|-----------------|-----------------|------------------|
| Cross-Section (nb) | 1353.85 | 1414.33 | 1395.16 | 1348.54 | 1338.08 |
| Generated Events | 13428913 | 12856109 | 13031719 | 13479699 | 13585597 |
| Filtered Events | 5000 | 5000 | 5000 | 5000 | 5000 |
| Filter Efficiency | 0.00037 | 0.000389 | 0.000384 | 0.000371 | 0.000368 |

These events are taken to go through ATLAS detector simulation and event reconstruction by the ATLAS collaboration. The output of this simulation is the AOD format, identical to that of data. These Monte Carlo simulated events are studied to determine $X_c(3872)$ event selection and detection efficiency.

7.2 Event Selection

The official ATLAS Monte Carlo samples described in Section 7.1 are analyzed with the event selection criteria. Due to the difference in the event generation filter conditions between the direct $pp \to X_c(3872)$ and the $B^+ \to X_c(3872)K^+$ events, the event selection analysis starts at Monte Carlo truth pion with $p_T > 0.5$ GeV/c and $|\eta| < 2.5$ (Cut-0). The total number of events of the direct $pp \to X_c(3872)K^+$ sample is 29,143 events, and the total number of events of the $B^+ \to X_c(3872)K^+$ sample is 47,117 events.

Event Selection at the 1st Step (Cut-1):

Firstly, the events are selected with the JpsiFinder Tool. The J/ψ candidates are selected with oppositely charged muons tracks, with the entries from the StacoMuonCollection, with χ^2 < 10000.0 (the vertex fit performed on the two muon tracks), and Monte Carlo truth matched. 29,141 events (99.99 ± 0.00 % of 29,143) of the direct $pp \to X_c(3872)$ sample pass the selection criteria, and 47,034 events (99.82 ± 0.02 % of 47,117) of the $B^+ \to X_c(3872)K^+$ sample pass the criteria, respectively. The simulated invariant mass distributions of $J/\psi \to \mu^+\mu^-$ of the two samples passing Cut-1 are shown at Figure 7.3.

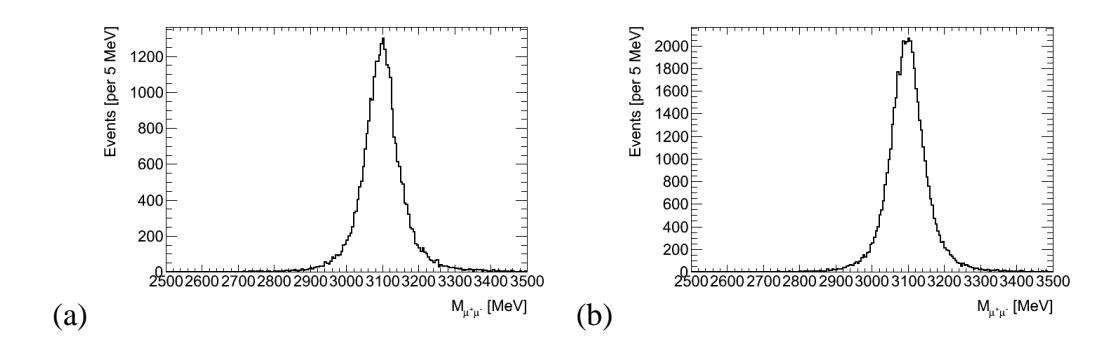


Figure 7.3. Mass distributions of $J/\psi \to \mu^+\mu^-$ events. (a) The direct $pp \to X_c(3872)$ sample. (b) The $B^+ \to X_c(3872)K^+$ sample. **Event Selection at the 2nd Step (Cut-2):**

The muon tracks are then selected with $p_T > 4.0$ GeV/c. 28,298 events (97.08 \pm 0.10 % of 29,141) of the direct $pp \to X_c(3872)$ sample pass, and 45,936 events (97.67 \pm 0.07 % of 47,034) of the $B^+ \to X_c(3872)K^+$ sample pass, respectively. Figure 7.4 and Figure 7.5 illustrate the muon p_T distributions and the p_T cut of the two samples, and the simulated invariant mass of the $J/\psi \to \mu^+\mu^-$ events passing the selection, respectively.

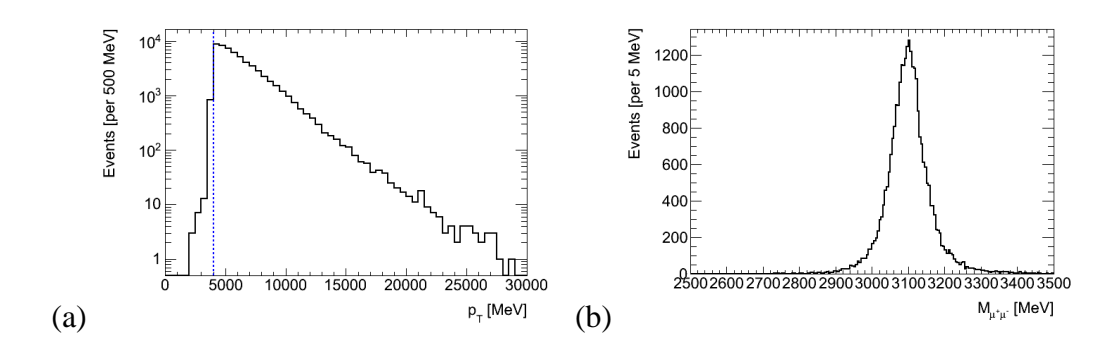


Figure 7.4. (a) The muon p_T distribution, and the p_T cut at 4.0 GeV/c. (b) The mass distribution of $J/\psi \to \mu^+\mu^-$ events of the direct $pp \to X_c(3872)$ sample.

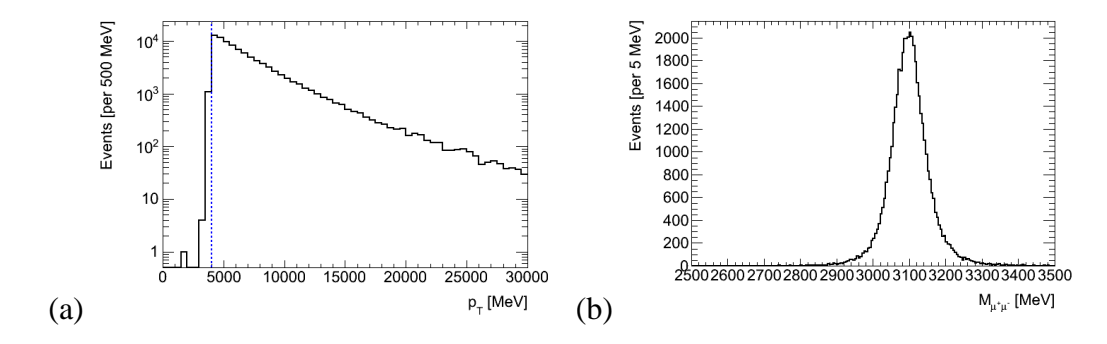


Figure 7.5. (a) The muon p_T distribution, and the p_T cut at 4.0 GeV/c. (b) The mass distribution of $J/\psi \to \mu^+\mu^-$ events of the $B^+ \to X_c(3872)K^+$ sample.

Event Selection at the 3rd Step (Cut-3):

The muon tracks are then selected with number of pixel hits \geq 1, and number of SCT hits \geq 6. A total of 27,971 events (98.88 \pm 0.06 % of 28,298) of the direct $pp \rightarrow X_c$ (3872) sample pass, and 45,479 events (99.01 \pm 0.05 % of 45,936) of the $B^+ \rightarrow X_c$ (3872) K^+ sample pass. Figure 7.6 and Figure 7.7 illustrate the number of pixel hits distributions and the number of SCT hits distributions of the two samples, and $J/\psi \rightarrow \mu^+\mu^-$ invariant mass distributions of the events passing the selection, respectively.

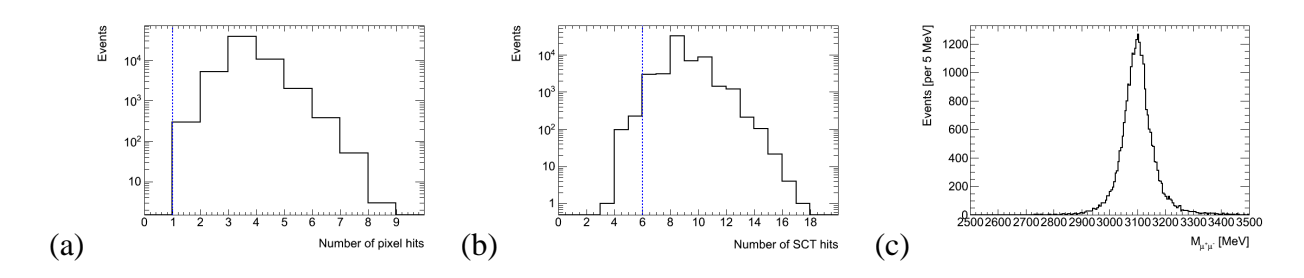


Figure 7.6. (a) Number of pixel hits distribution of muon tracks, (b) number of SCT hits distribution of muon tracks, (c) mass distribution of $J/\psi \to \mu^+\mu^-$ of the direct $pp \to X_c(3872)$ sample.

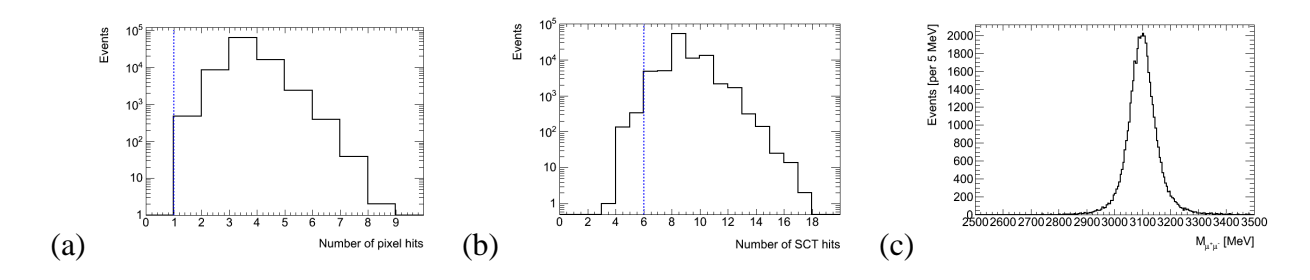


Figure 7.7. (a) Number of pixel hits distribution of muon tracks, (b) number of SCT hits distribution of muon tracks, (c) mass distribution of $J/\psi \to \mu^+\mu^-$ of the $B^+ \to X_c(3872)K^+$ sample.

Event Selection at the 4th Step (Cut-4):

For reconstructing the $X_c(3872) \to J/\psi \pi^+ \pi^-$ candidates, the J/ψ candidates are selected with the $\mu^+\mu^-$ invariant mass in a mass window, $|M(\mu\mu) - M(J/\psi)| < 120 \text{ MeV/c}^2$, where $M(J/\psi)$ is 3,096.916 MeV/c², the PDG mass value of J/ψ . 26,137 events (93.44 ± 0.15 % of 27,971) of the direct $pp \to X_c(3872)$ sample pass, and 43,177 events (94.94 ± 0.10% of 45,479) of the $B^+ \to X_c(3872)K^+$ sample pass. The difference of this selection efficiency between the two samples is about ~1.5 %. The invariant mass distributions of $J/\psi \to \mu^+\mu^-$ of the two samples passing Cut-4 are shown at Figure 7.8.

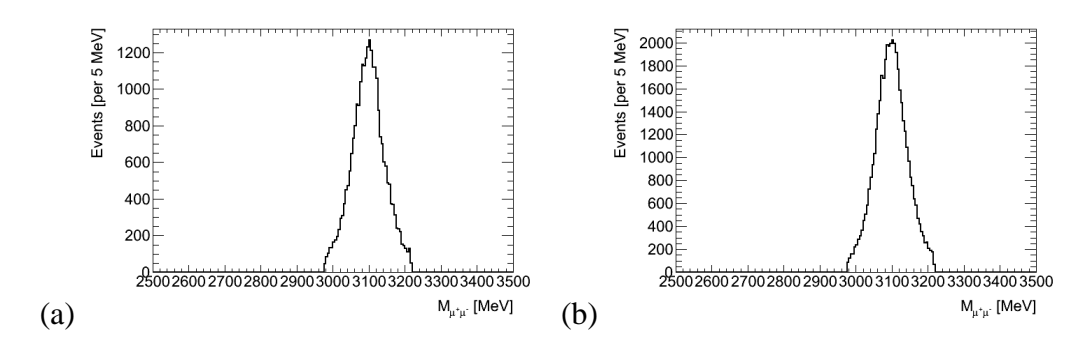


Figure 7.8. Invariant mass distributions of $J/\psi \to \mu^+\mu^-$ of (a) the direct $pp \to X_c(3872)$ sample, and (b) the $B^+ \to X_c(3872)K^+$ sample.

Event Selection at the 5th Step (Cut-5):

In order to reconstruct a $X_c(3872) \rightarrow J/\psi \pi^+ \pi^-$ candidate, a J/ψ candidate and a pair of oppositely charged $\pi^+\pi^-$ tracks are selected, and truth matched. The truth matching of the $X_c(3872) \rightarrow J/\psi \pi^+\pi^-$ candidate is performed with any one of the three methods: the Four Track truth matching (FT), or the Decaying Topology truth matching (TP), or the Truth Mass Window truth matching (MW). Refer to the Appendix codes for details of these methods. In the FT method, the four tracks, $\mu^+\mu^-\pi^+\pi^-$, of the $X_c(3872)$ candidate are identical kinematically to

the four tracks of the Monte Carlo signal $X_c(3872)$ in an event. In the TP method, the parent particles and grand-parent particles of the track-truth particles are identified, and the whole decay tree is formed as the correct decay topology of the Monte Carlo signal $X_c(3872)$, where $X_c(3872) \rightarrow J/\psi \pi^+ \pi^-$, $J/\psi \rightarrow \mu^+ \mu^-$. In the MW method, the invariant mass of the four track-truth particles is calculated, and is selected within a very narrow mass window, $|M(\mu\mu\pi\pi)-M(X_c(3872))| < 1 \text{ MeV/c}^2$.

Applying the above selection criteria, 10,684 events of the direct $pp \to X_c(3872)$ sample pass, and 16,226 events of the $B^+ \to X_c(3872)K^+$ sample pass. However, referring to Figure 7.9, the $J/\psi\pi^+\pi^-$ candidates are selected within the invariant mass region, from 3,500.0 MeV/c² to 6,000.0 MeV/c², and some of them distribute with the mass far away from our target value 3,872.0 MeV/c². The four-track invariant mass distribution plots show the significant deviations from the generated $X_c(3872)$ mass value a small fraction of the $J/\psi\pi^+\pi^-$ combinations. The event selection criteria, where the Monte Carlo truth invariant mass within $|M(\mu\mu\pi\pi)|$ - $M(X_c(3872))| < 0.1 \text{ MeV/c}^2$ and four-track invariant mass within $|M(\mu\mu\pi\pi)|$ - $M(X_c(3872))| < 0.1 \text{ MeV/c}^2$, is subsequently applied. Therefore, 20,444 events (78.22 \pm 0.26 % of 26,137) of the direct $pp \to X_c(3872)$ sample pass the event selection, and 34,436 events (79.76 \pm 0.19 % of 43,177) of the $B^+ \to X_c(3872)K^+$ sample pass. The difference of this selection efficiency between the two samples is about ~1.54 %. The mass distributions of $X_c(3872) \to J/\psi\pi^+\pi^-$ of the two samples passing Cut-5 are shown at Figure 7.10.

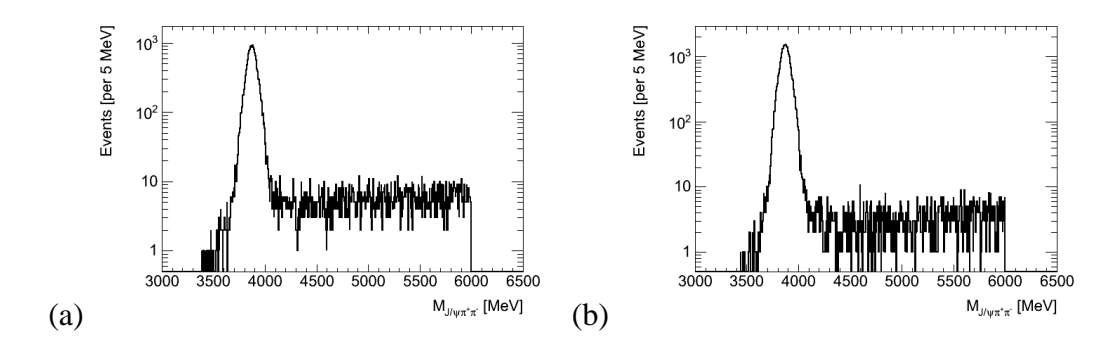


Figure 7.9. The four-track invariant mass distribution of $J/\psi\pi^+\pi^-$. (a) The direct $pp \to X_c(3872)$ sample. (b) The $B^+ \to X_c(3872)K^+$ sample.

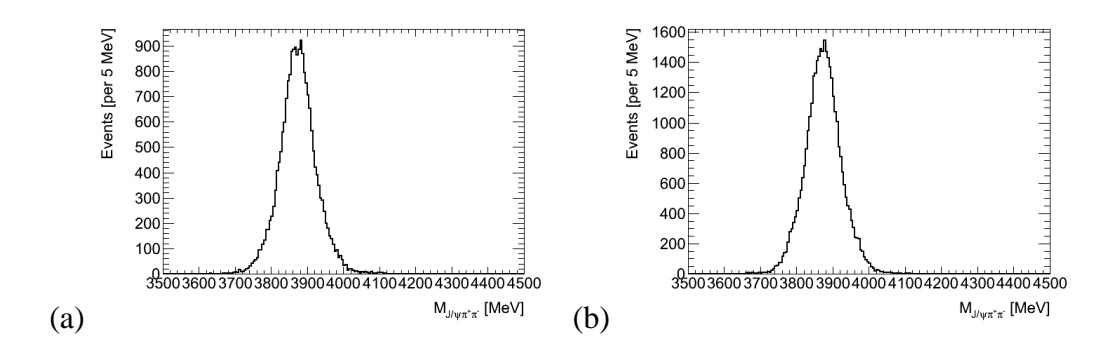


Figure 7.10. Simulated invariant mass distributions of $X_c(3872) \rightarrow J/\psi \pi^+ \pi^-$ of (a) the direct $pp \rightarrow X_c(3872)$ sample, and (b) the $B^+ \rightarrow X_c(3872)K^+$ sample.

Event Selection at the 6th Step (Cut-6):

The pion tracks are then selected with $p_T > 0.6$ GeV/c to suppress background arising from slow charged particles. 17,865 events (87.39 \pm 0.23 % of 20,444) of the direct $pp \rightarrow X_c(3872)$ sample pass, and 30,567 events (88.76 \pm 0.17 % of 34,436) of the $B^+ \rightarrow X_c(3872)K^+$ sample pass. Figure 7.11 and Figure 7.12 illustrate the pion p_T distributions and the p_T cut standard of the two samples, and the $X_c(3872) \rightarrow J/\psi \pi^+ \pi^-$ mass distributions passing the selection, respectively.

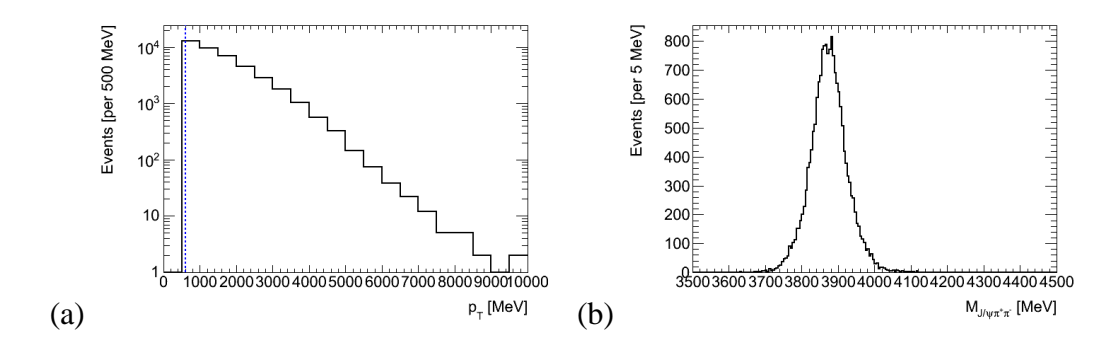


Figure 7.11. (a) Pion track p_T distribution, and the cut at 0.6 GeV/c. (b) The mass distribution of $X_c(3872) \rightarrow J/\psi \pi^+ \pi^-$ of the direct $pp \rightarrow X_c(3872)$ sample.

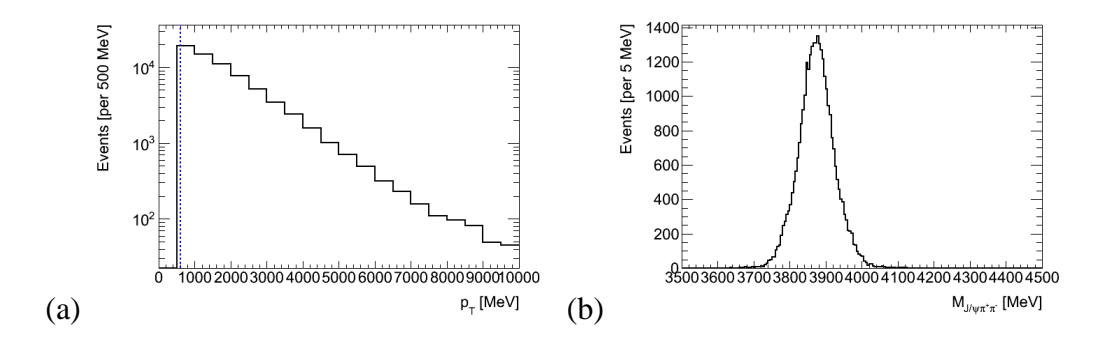


Figure 7.12. (a) Pion track p_T distribution, and the cut at 0.6 GeV/c. (b) The mass distribution of $X_c(3872) \rightarrow J/\psi \pi^+ \pi^-$ of the $B^+ \rightarrow X_c(3872) K^+$ sample.

Event Selection at the 7th Step (Cut-7):

The pion tracks are then selected with $|\eta| < 2.5$. This selection criterion was already performed while the pre-selection of the pion tracks and the muon tracks. So it is used to confirm the pseudo-rapidity distribution of the pion tracks again, and all events passing previous event selection also pass this event selection as well.

Event Selection at the 8th Step (Cut-8):

The pion tracks are then selected with number of pixel hits ≥ 1 , and number of SCT hits \geq 6. 17,072 events (95.56 \pm 0.15 % of 17,865) of the direct $pp \rightarrow X_c$ (3872) sample pass, and

29,209 events (95.56 \pm 0.12 % of 30,567) of the $B^+ \to X_c(3872)K^+$ sample pass. Figure 7.13 and Figure 7.14 illustrate the pion p_T distributions and the p_T cut standard of the two samples, and the $X_c(3872) \to J/\psi \pi^+ \pi^-$ mass distributions passing the selection, respectively.

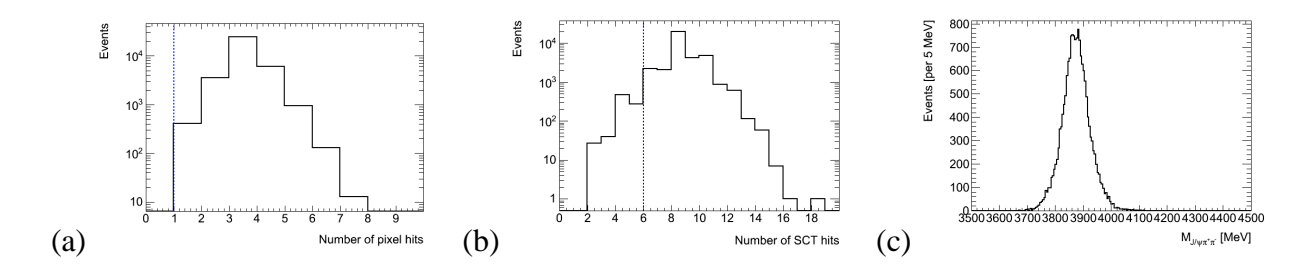


Figure 7.13. (a) Number of pixel hits distribution of pion tracks, (b) number of SCT hits distribution of pion tracks, (c) mass distribution of $X_c(3872) \rightarrow J/\psi \pi^+ \pi^-$ of the direct $pp \rightarrow X_c(3872)$ sample.

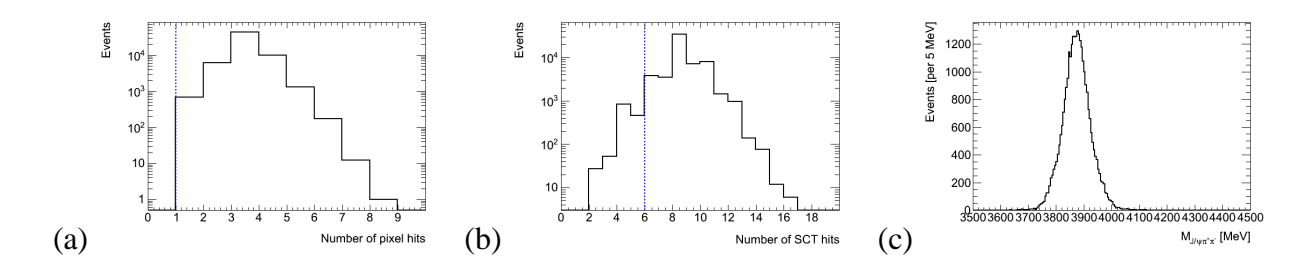


Figure 7.14. (a) Number of pixel hits distribution of pion tracks, (b) number of SCT hits distribution of pion tracks, (c) mass distribution of $X_c(3872) \rightarrow J/\psi \pi^+ \pi^-$ of the $B^+ \rightarrow X_c(3872)K^+$ sample.

Event Selection at 9th Step (Cut-9):

The $J/\psi\pi^+\pi^-$ combinations are then fitted with the common vertex and J/ψ mass constraint to improve mass resolution of the reconstructed $X_c(3872)$. Figure 7.15 lists the code segment that performs the vertex fitting for the $J/\psi\pi^+\pi^-$ combination. The J/ψ mass, the $\mu^+\mu^-$ combination, is constrained at 3,096.916 MeV/c², the PDG value of J/ψ particle, by using the function "setMassConstraints()". The $\mu^+\mu^-\pi^+\pi^-$ track masses are given with the muon mass

and the pion mass, respectively, using the function "setTrackMasses()", and a set of the four tracks to share the common vertex is passed to the fitter, using the function "setInputTracks()". The function "performFit()" is used to perform the fit, and the results of the fit are automatically written to yVertex, a Trk::VxCandidate*, using the function "getFittedVertex".

```
// Set up collections
TrackBag muons, quadruplet;
quadruplet.reserve(4);
muons.reserve(2);
quadruplet.push back(muon1);
quadruplet.push back(muon2);
muons.push back(muon1);
muons.push back(muon2);
quadruplet.push back(pion1);
quadruplet.push back(pion2);
Trk::VxCandidate* yVertex(NULL);
// Vertex fit // Xc fit
myVKalVrtFitter.reset();
myVKalVrtFitter.setMassConstraints(jpsiMassConstraint,consIndices);
myVKalVrtFitter.setTrackMasses(YcTrkMasses);
myVKalVrtFitter.setInputTracks(quadruplet);
myVKalVrtFitter.performFit();
yVertex = myVKalVrtFitter.getFittedVertex();
```

Figure 7.15. Analysis codes for fitting the vertex of the $X_c(m) \to J/\psi \pi^+ \pi^-$ events.

After the vertex fitting, 17,051 events (99.88 \pm 0.03 % of 17,072) of the direct $pp \rightarrow X_c(3872)$ sample pass, and 29,187 events (99.92 \pm 0.02 % of 29,209) of the $B^+ \rightarrow X_c(3872)K^+$ sample pass. The mass distributions of $X_c(3872) \rightarrow J/\psi \pi^+ \pi^-$ of the two samples passing Cut-9 are shown at Figure 7.16. Figure 7.17 and Figure 7.18 show the mass distribution with fits, before and after vertex fitting. The $\sigma_{\text{no-fit}}$ (before the fits) is 48.6 ± 1.8 (MeV/c²) and the σ_{fit} (after the fit has been applied) is 12.8 ± 0.3 (MeV/c²) of the direct $pp \rightarrow X_c(3872)$ sample. The $\sigma_{\text{no-fit}}$ is 48.6 ± 2.3 (MeV/c²) (before the fits) and the σ_{fit} (after the fit has been applied) is 12.7 ± 0.2 (MeV/c²) of the $B^+ \rightarrow X_c(3872)K^+$ sample.

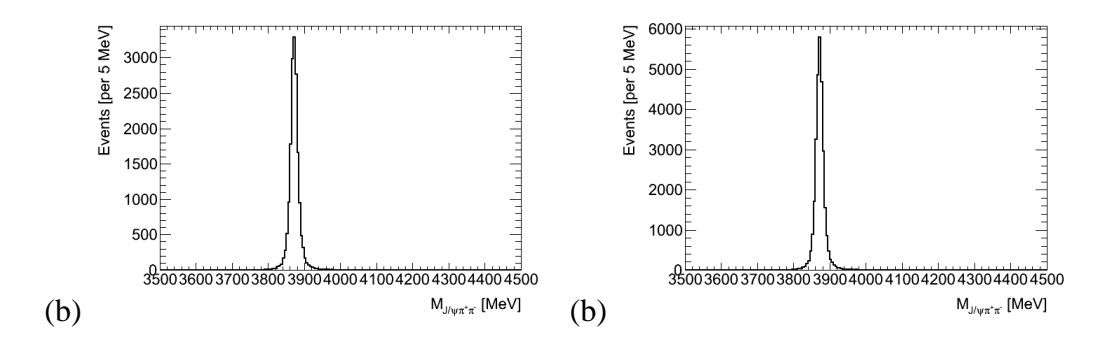


Figure 7.16. Mass distributions of $X_c(3872) \to J/\psi \pi^+ \pi^-$. (a) The direct $pp \to X_c(3872)$ sample. (b) The $B^+ \to X_c(3872)K^+$ sample.

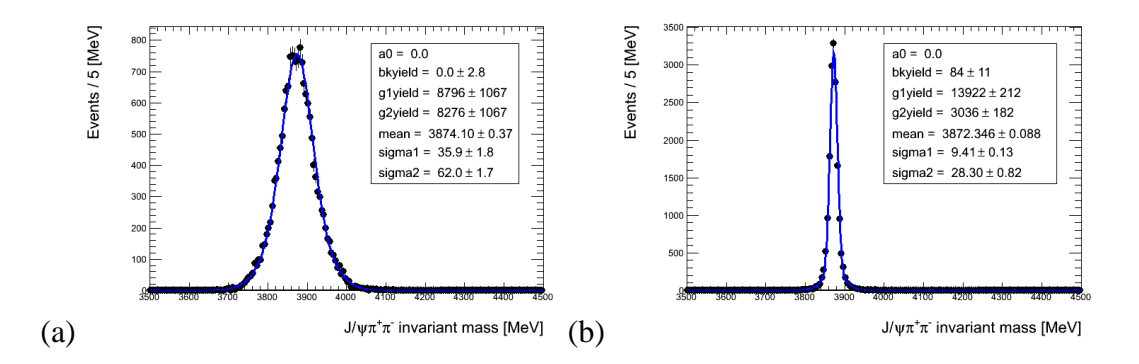


Figure 7.17. (a) Mass distribution of $X_c(3872) \rightarrow J/\psi \pi^+ \pi^-$ before vertex fitting. ($\sigma_{\text{no-fit}} = 48.6 \pm 1.8 \text{ (MeV/c}^2\text{)}$). (b) Mass distribution of $X_c(3872) \rightarrow J/\psi \pi^+ \pi^-$ after vertex fitting. ($\sigma_{\text{fit}} = 12.8 \pm 0.3 \text{ (MeV/c}^2\text{)}$) of the direct $pp \rightarrow X_c(3872)$ sample.

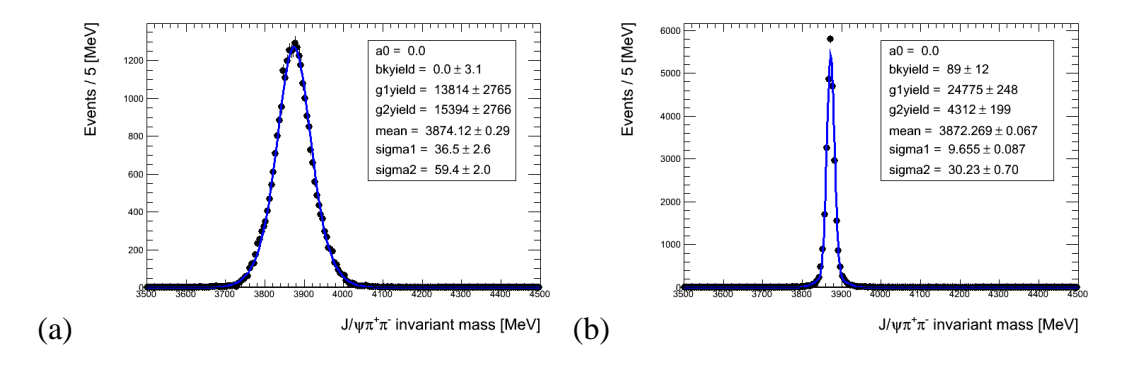


Figure 7.18. (a) Mass distribution of $X_c(3872) \rightarrow J/\psi \pi^+ \pi^-$ before vertex fitting. ($\sigma_{\text{no-fit}} = 48.6 \pm 2.3 \text{ (MeV/c}^2\text{)}$). (b) Mass distribution of $X_c(3872) \rightarrow J/\psi \pi^+ \pi^-$ after vertex fitting. ($\sigma_{\text{fit}} = 12.7 \pm 0.2 \text{ (MeV/c}^2\text{)}$) of the direct $pp \rightarrow X_c(3872)$ sample.

Event Selection at the 10th Step (Cut-10):

The $J/\psi\pi^+\pi^-$ combinations are finally selected with $\operatorname{Prob}(\chi^2) > 0.02$ of the $\mu^+\mu^-\pi^+\pi^-$ combination, where $\operatorname{Prob}(\chi^2) = 1 - P(\frac{NDF}{2}, \frac{\chi^2}{2})$. The function $P(\frac{NDF}{2}, \frac{\chi^2}{2})$ is the incomplete gamma function. The χ^2 is the rms squared of the difference between the measured values, and the fitted values of the vertex fit performed on the $\mu^+\mu^-\pi^+\pi^-$ tracks. The NDF is the number of degree of freedom. The signal $J/\psi\pi^+\pi^-$ combinations are selected and a large fraction of the backgrounds are suppressed. 15,163 events (88.93 \pm 0.24 % of 17,051) of the direct $pp \to X_c(3872)$ sample pass, and 26,023 events (89.16 \pm 0.18 % of 29,187) of the $B^+ \to X_c(3872)K^+$ sample pass. Figure 7.19 and Figure 7.20 illustrate the $\operatorname{Prob}(\chi^2)$ distributions and the $\operatorname{Prob}(\chi^2)$ cut standard of the two samples, and the $X_c(3872) \to J/\psi\pi^+\pi^-$ mass distributions passing the selection.

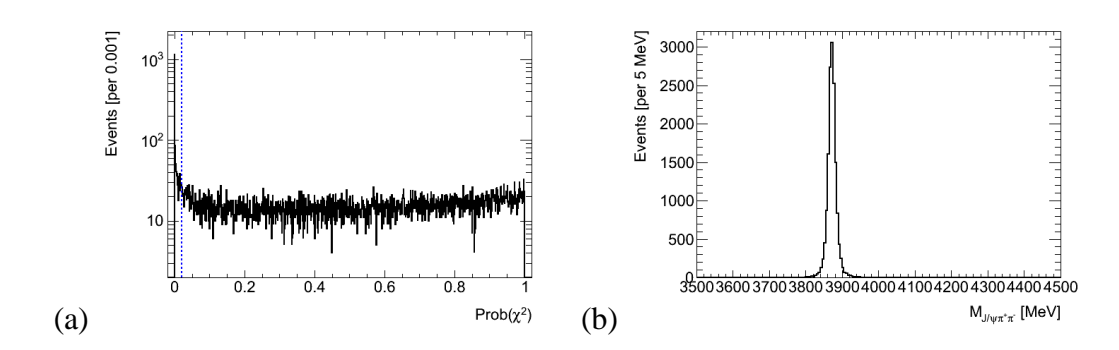


Figure 7.19. (a) Prob(χ^2) distribution of $\mu^+\mu^-\pi^+\pi^-$ combination, (b) mass distributions of $X_c(3872) \rightarrow J/\psi \pi^+\pi^-$ of the direct $pp \rightarrow X_c(3872)$ sample.

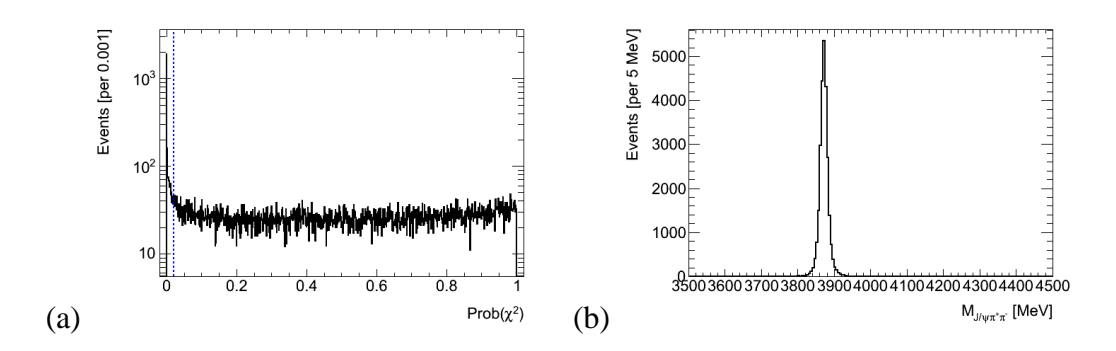


Figure 7.20. (a) Prob(χ^2) distribution of $\mu^+\mu^-\pi^+\pi^-$ combination, (b) mass distributions of $X_c(3872) \to J/\psi \pi^+\pi^-$ of the $B^+ \to X_c(3872) K^+$ sample.

In conclusion, the overall event selection efficiency of the direct $pp \to X_c(3872)$ sample is ~52.03 \pm 0.29 % (15,163 of 29,143 events), the overall event selection efficiency of the $B^+ \to X_c(3872)K^+$ sample is ~55.23 \pm 0.23 % (26,023 of 47,117 events). The difference in the selection efficiencies between the two samples is about ~3.2 %. Table 7.3 lists the numeric results of each event selection steps.

Table 7.3. List of events and the efficiencies passing the event selections.

| Direct pp | Direct $pp \to X_c(3872)$ $B^+ \to X_c(3872)K$ | | | | | | | |
|---|---|-----------------------------|-----------------|--|--|--|--|--|
| Number of Events | Efficiency | Number of Events | Efficiency | | | | | |
| Cut-0: Truth pion, $p_T > 0.5 \text{ GeV/c}$, $ \eta < 2.5$ | | | | | | | | |
| 29,143 | N/A | 47,117 | N/A | | | | | |
| Cut-1: $J/\psi \rightarrow \mu^+\mu^-$ co | Cut-1: $J/\psi \to \mu^+\mu^-$ combination, STACOMUON, $\chi^2 < 10000.0$ of muons, truth matched | | | | | | | |
| 29,141 | 99.99 ± 0.00 % | 47,034 | 99.82 ± 0.02 % | | | | | |
| Cut-2: Muon tracks: p _T | > 4.0 GeV/c | | | | | | | |
| 28,289 | $97.08 \pm 0.10 \%$ | 45,936 | 97.67 ± 0.07 % | | | | | |
| Cut-3: Muon tracks: Nu | umber of pixel hits ≥ 1 , N | fumber of SCT hits ≥ 6 | 1 | | | | | |
| 27,971 | $98.88 \pm 0.06 \%$ | 45,479 | 99.01 ± 0.05 % | | | | | |
| Cut-4: $ M(\mu \mu) - M(J/\psi) $ | Cut-4: $ M(\mu\mu) - M(J/\psi) < 120 \text{ MeV/c}^2$ | | | | | | | |
| 26,137 | 93.44 ± 0.15 % | 43,177 | 94.94 ± 0.10 % | | | | | |
| Cut-5: $J/\psi \pi^+\pi^-$ comb | ination, truth matched | | 1 | | | | | |
| 20,444 | $78.22 \pm 0.26 \%$ | 34,436 | 79.76 ± 0.19 % | | | | | |
| Cut-6: Pion tracks: p _T > | > 0.6 GeV/c | | | | | | | |
| 17,865 | 87.39 ± 0.23 % | 30,567 | 88.76 ± 0.17 % | | | | | |
| Cut-7: Pion tracks: η | < 2.5 | | | | | | | |
| 17,865 | $100.00 \pm 0.00 \%$ | 30,567 | 100.00 ± 0.00 % | | | | | |
| Cut-8: Pion tracks: Nur | mber of pixel hits ≥ 1 , Nu | mber of SCT hits ≥ 6 | 1 | | | | | |
| 17,072 | 95.56 ± 0.15 % | 29,209 | 95.56 ± 0.12 % | | | | | |
| Cut-9: Vertex fitting of the $J/\psi \pi^+\pi^-$ combination, with J/ψ mass constraint | | | | | | | | |
| 17,051 | $99.88 \pm 0.03 \%$ | 29,187 | 99.92 ± 0.02 % | | | | | |
| Cut-10: $Prob(\chi^2) > 0.02$ | Cut-10: Prob(χ^2) > 0.02 of the $\mu^+\mu^-\pi^+\pi^-$ combination | | | | | | | |
| 15,163 | 88.93 ± 0.24 % | 26,023 | 89.16 ± 0.18 % | | | | | |

7.3 Mass Spectra of Simulated $J/\psi \pi^+\pi^-$ Events

From the Monte Carlo analysis, the mass distributions are obtained and the mass values are found to be consistent with the generated values. Table 7.4 gives the summary of Monte Carlo $X_c(3872)$ events analysis results. Only muons with transverse momenta greater than 4.0 GeV/c, and pseudo-rapidity $|\eta| < 2.5$ are selected. Pions with transverse momenta greater than 0.6 GeV/c, and pseudo-rapidity $|\eta| < 2.5$ are selected. The J/ψ particles are selected in a given mass window $(3.097 \pm 0.12 \text{ GeV/c}^2)$, and mass constraint of the J/ψ particle is applied. The details of the events selection criteria are described in Section 7.2. The mass distribution of the $X_c(3872)$ events is fitted by double Gaussian functions sharing an identical mass mean value, by using the Roofit function in the ROOT macro, referring to Appendix IV for more information. The $X_c(3872) \rightarrow J/\psi \pi^+ \pi^-$ mass distributions of the direct $pp \rightarrow X_c(3872)$ sample, the $B^+ \rightarrow X_c(3872)K^+$ sample, and the combined samples are shown at Figure 7.21-23.

Table 7.4. Summary of Monte Carlo study of the $X_c(3872) \rightarrow I/\psi \pi^+ \pi^-$.

| Physics Process | Direct $X_c(3872)$ | $B^+ \to X_c(3872)K^+$ | Combined |
|---|---------------------|------------------------|---------------------|
| Number of events analyzed | 29,143 | 47,117 | N/A |
| Number of events reconstructed | 15,163 | 26,023 | N/A |
| Detection efficiency | 52.03 ± 0.29 % | 55.23 ± 0.23 % | N/A |
| Mass (MeV/c ²) | $3,872.28 \pm 0.09$ | $3,872.27 \pm 0.07$ | $3,872.27 \pm 0.05$ |
| Mass rms resolution (MeV/c ²) | 11.8 ± 0.3 | 11.6 ± 0.2 | 11.7 ± 0.2 |
| χ^2 /dof value of fit | 1.287 | 1.442 | 2.456 |

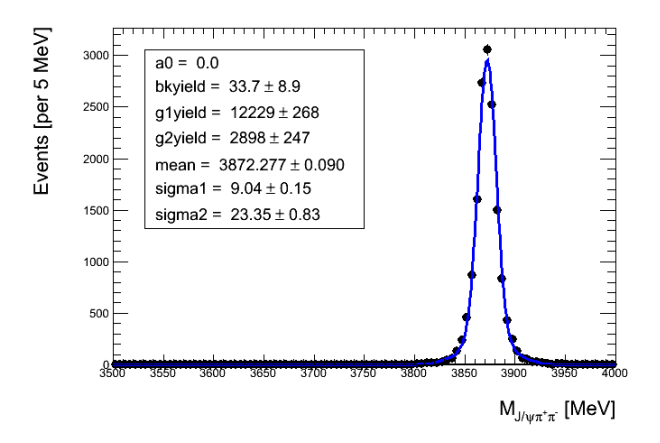


Figure 7.21. $X_c(3872) \rightarrow J/\psi \pi^+ \pi^-$ mass distribution of the direct $pp \rightarrow X_c(3872)$ sample.

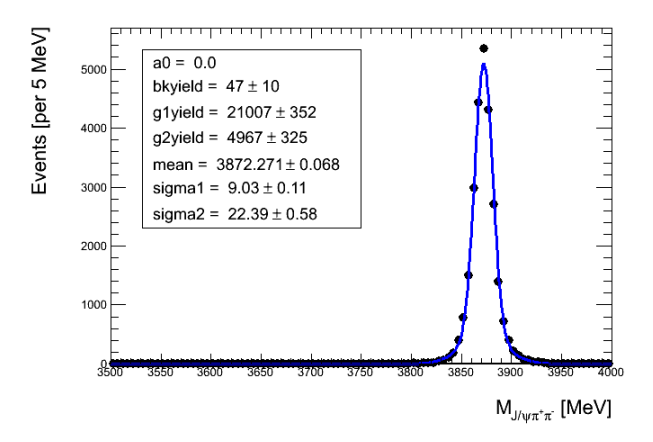


Figure 7.22. $X_c(3872) \rightarrow J/\psi \pi^+ \pi^-$ mass distribution of the $B^+ \rightarrow X_c(3872) K^+$ sample.

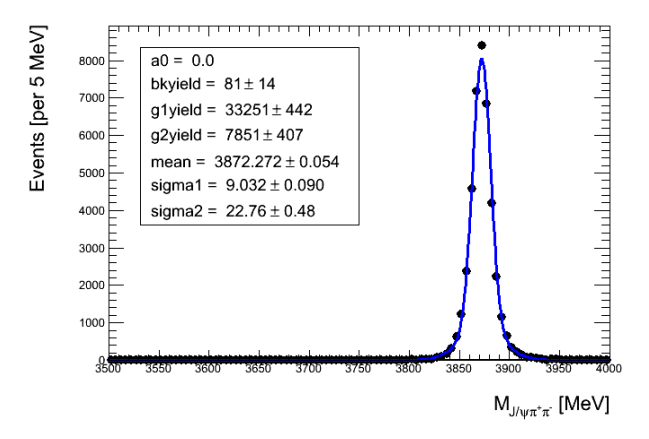


Figure 7.23. $X_c(3872) \rightarrow J/\psi \pi^+ \pi^-$ mass distribution of combined samples.

7.4 Transverse Momenta

Figure 7.24 shows the transverse momentum distribution of reconstructed muons, of the direct $pp \to X_c(3872)$ sample. The muons must pass the muon filters, and the muons are accordingly analyzed with lowest p_T 4 GeV/c cut, pseudo-rapidity $|\eta| < 2.5$, number of pixel detector hits ≥ 1 , and number of SCT hits ≥ 6 . Figure 7.25 shows the transverse momentum distribution of reconstructed pions, of the direct $pp \to X_c(3872)$ sample. The pions are selected with transverse momenta greater than 600 MeV/c, pseudo-rapidity $|\eta| < 2.5$, number of pixel detector hits ≥ 1 , and number of SCT hits ≥ 6 .

The transverse momentum distribution of the J/ψ particles, reconstructed from two oppositely charged muon tracks with χ^2 < 10000.0, is shown in Figure 7.26. Most J/ψ particles contain the transverse momenta greater than 10 GeV/c. The J/ψ particles with transverse momenta less than 10 GeV/c are reconstructed from two muons traveling in different directions with larger angles.

Figure 7.27 shows the transverse momentum distribution of the $X_c(3872)$ particles which are reconstructed from two muon tracks and two pion tracks, as the selection criteria described in Section 7.2. Due to the contribution of two pions p_T , The transverse momenta of $X_c(3872)$ particles are generally greater than those of J/ψ particles. The $X_c(3872)$ particles with transverse momenta less than 10 GeV/c are reconstructed from two muons and two pions traveling in different directions.

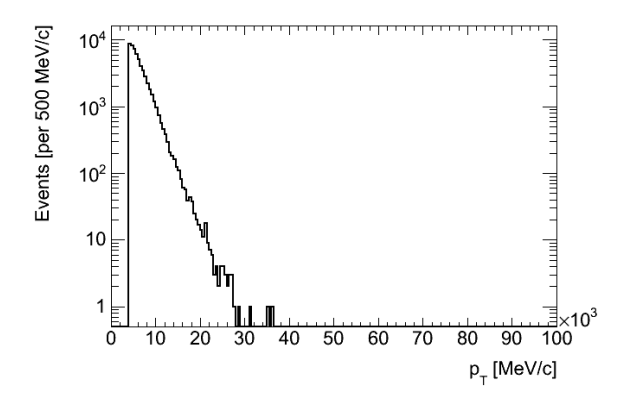


Figure 7.24. Transverse momentum distribution of muons of the direct $pp \rightarrow X_c(3872)$ sample.

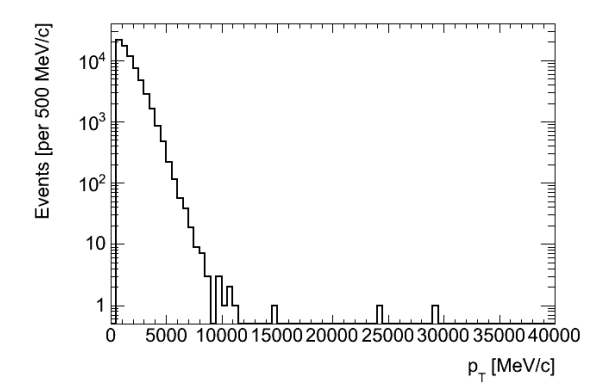


Figure 7.25. Transverse momentum distribution of pions of the direct $pp \to X_c(3872)$ sample.

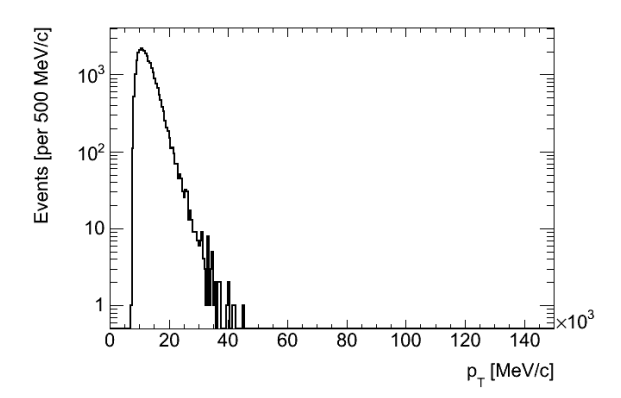


Figure 7.26. Transverse momentum distribution of the J/ψ of the direct $pp \to X_c(3872)$ sample.

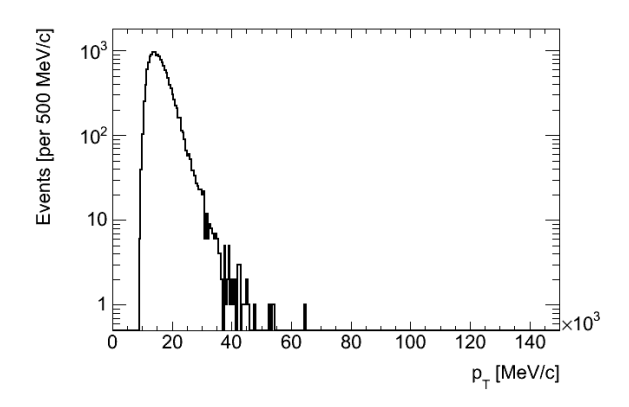


Figure 7.27. Transverse momentum distribution of the $X_c(3872)$ of the direct $pp \to X_c(3872)$ sample.

Figure 7.28-31 show the transverse momenta distributions of muons, pions, the J/ψ , and the $X_c(3872)$, of the $B^+ \to X_c(3872)K^+$ sample. The event filters and analysis selection criteria are identical to those used for the direct $pp \to X_c(3872)$ sample.

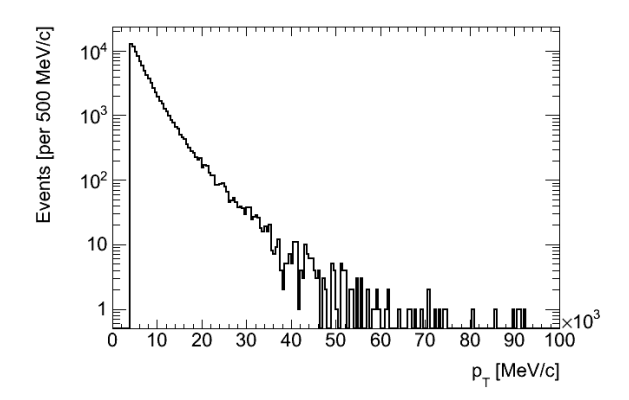


Figure 7.28. Transverse momentum distribution of muons of the $B^+ \to X_c(3872)K^+$ sample.

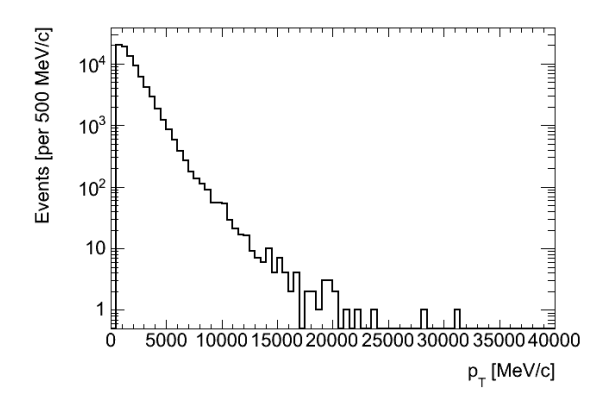


Figure 7.29. Transverse momentum distribution of pions of the $B^+ \to X_c(3872)K^+$ sample.

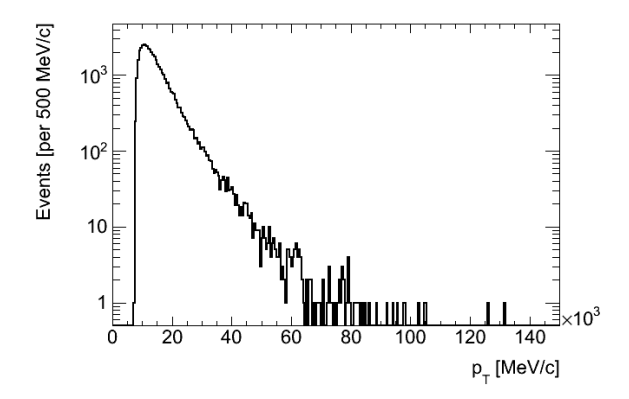


Figure 7.30. Transverse momentum distribution of the J/ψ of the $B^+ \to X_c(3872)K^+$ sample.

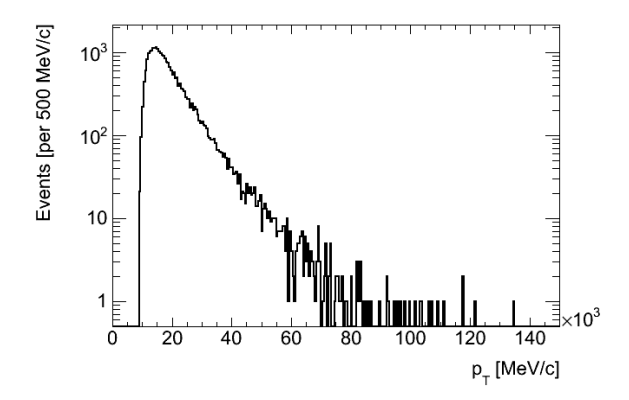


Figure 7.31. Transverse momentum distribution of the $X_c(3872)$ of the $B^+ \to X_c(3872)K^+$ sample.

7.5 Reconstruction Efficiencies

Figure 7.32 shows the reconstruction efficiency of transverse momentum and pseudorapidity distributions of muons, of the direct $pp \rightarrow X_c(3872)$ sample. In Figures 7.32 (b) and (d), the generated muons (blue line) are the Monte Carlo signal muons without any event selection criteria. The pre-selected muons (black line) are the Monte Carlo signal muons with event selection Cut-0. The reconstructed muons are the detected muons, with track muon $p_T > 4.0$ GeV/c, $|\eta| < 2.5$, number of pixel hits ≥ 1 , and number of SCT hits ≥ 6 . The reconstruction efficiency is calculated with "number of reconstructed muons / number of pre-selected muons". The high reconstruction efficiency (~ 97.97 %) reveals that most muons are detected by the tacking systems and identified by the muon spectrometers.

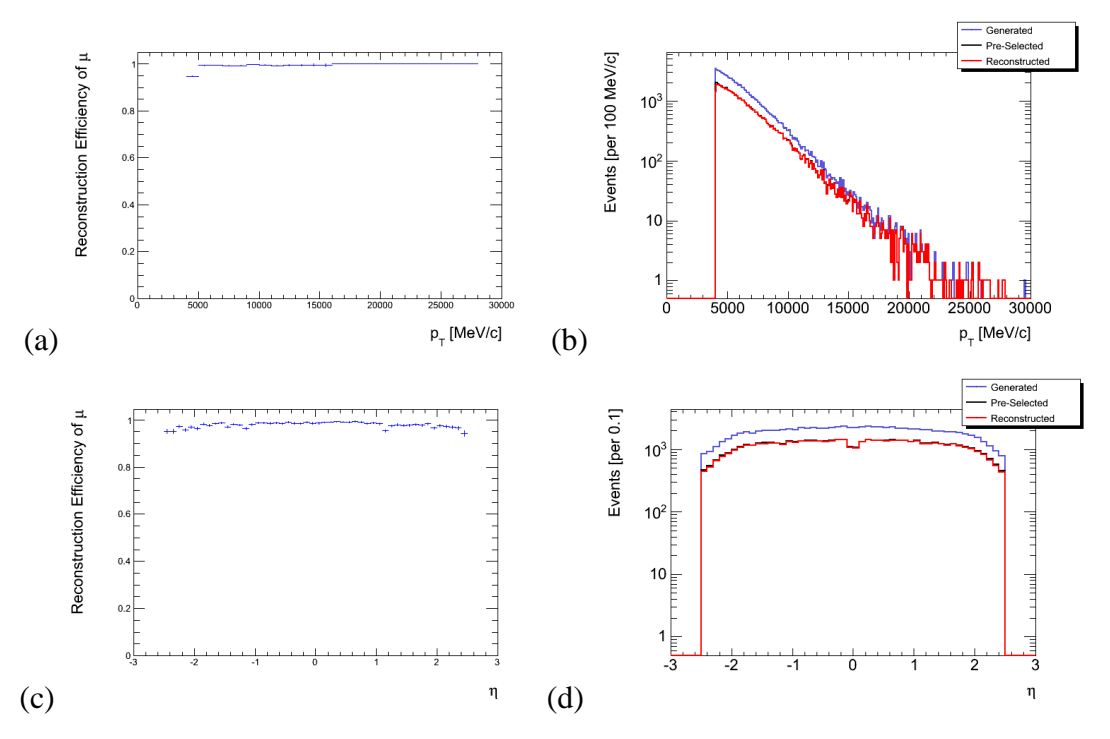


Figure 7.32. Reconstruction efficiency of muons of the direct $pp \to X_c(3872)$ sample. (a) reconstruction efficiency vs. muon p_T , (b) muon p_T distribution, (c) reconstruction efficiency vs. muon η , (d) muon η distribution.

Figure 7.33 shows the reconstruction efficiency of pions, of the direct $pp \to X_c(3872)$ sample. In Figures 7.33 (b) and (d), the generated pions (blue line) are the Monte Carlo signal pions without any event selection criteria. The Pre-Selected pions (black line) are the Monte Carlo signal pions with event selection Cut-0. The reconstructed pions are the detected pions, with track pion $p_T > 0.6$ GeV/c, $|\eta| < 2.5$, number of pixel hits ≥ 1 , and number of SCT hits ≥ 6 . The reconstruction efficiency is calculated with "number of reconstructed pions / number of preselected pions". The high reconstruction efficiency (~92.44 %) indicates that most pions are detected by the tacking systems.

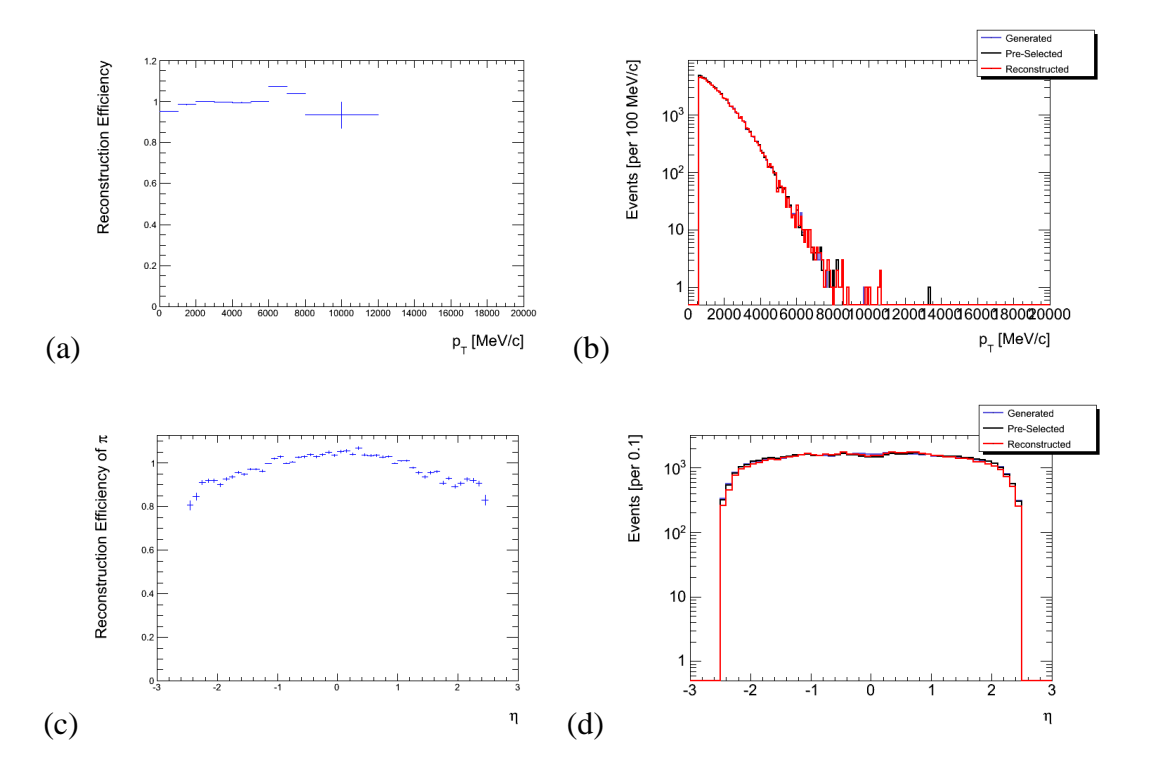


Figure 7.33. Reconstruction efficiency of pions of the direct $pp \to X_c(3872)$ sample. (a) reconstruction efficiency vs. pion p_T , (b) pion p_T distribution, (c) reconstruction efficiency vs. pion η , (d) pion η distribution.

Figure 7.34 shows the reconstruction efficiency of the J/ψ , of the direct $pp \to X_c(3872)$ sample. The reconstruction efficiency (~95.97 %) is calculated with "number of Reconstructed J/ψ (at Cut-4) / number of Pre-Selected J/ψ (at Cut-0)". Besides, the reconstruction efficiency of the J/ψ could be numerically estimated from the reconstruction efficiency of muons ($\varepsilon_{J/\psi} = \varepsilon_{\mu}^2$, (97.97 %)² = ~95.98 %).

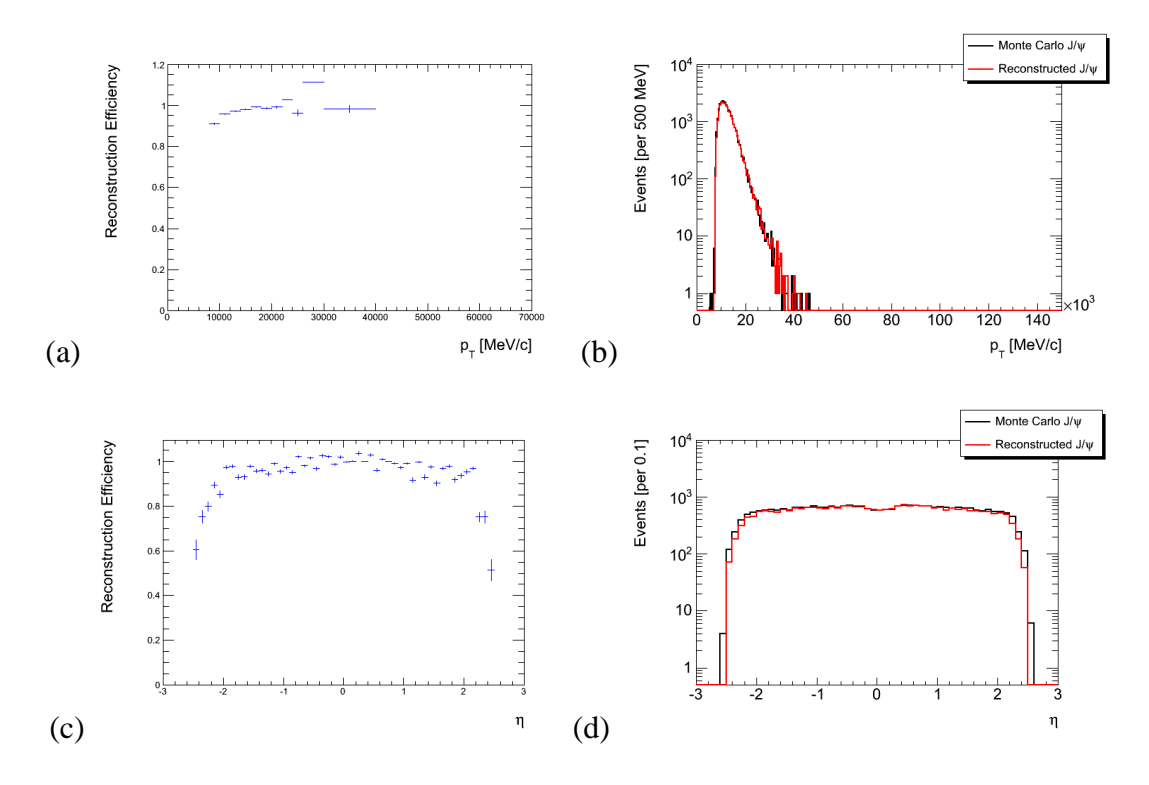


Figure 7.34. Reconstruction efficiency of the J/ψ of the direct $pp \to X_c(3872)$ sample. (a) reconstruction efficiency vs. J/ψ p_T, (b) J/ψ p_T distribution, (c) reconstruction efficiency vs. J/ψ η, (d) J/ψ η distribution.

The estimated reconstruction efficiency of the $X_c(3872)$ is ~52.03 %, as shown in Figure 7.35, and is calculated with "number of reconstructed $X_c(3872)$ (at Cut-10) / number of preselected $X_c(3872)$ (at Cut-0)". The reconstruction efficiency of the $X_c(3872)$ is strongly influenced by the reconstruction efficiency of the pions. Comparing with the reconstruction

efficiency of p_T distribution and η distribution of the J/ψ (Figure 7.34), the reconstruction efficiency of the $X_c(3872)$ particle is lower at lower p_T region and larger η region. The $X_c(3872)$, composed of $\mu^+\mu^-\pi^+\pi^-$ tracks, is barely detected with soft pion tracks ($p_T < 600$ MeV/c) and the tracks with larger η . The $X_c(3872)$ particles with transverse momenta less than 10.0 GeV/c are not well reconstructed, the efficiency below 10 GeV/c is not well determined.

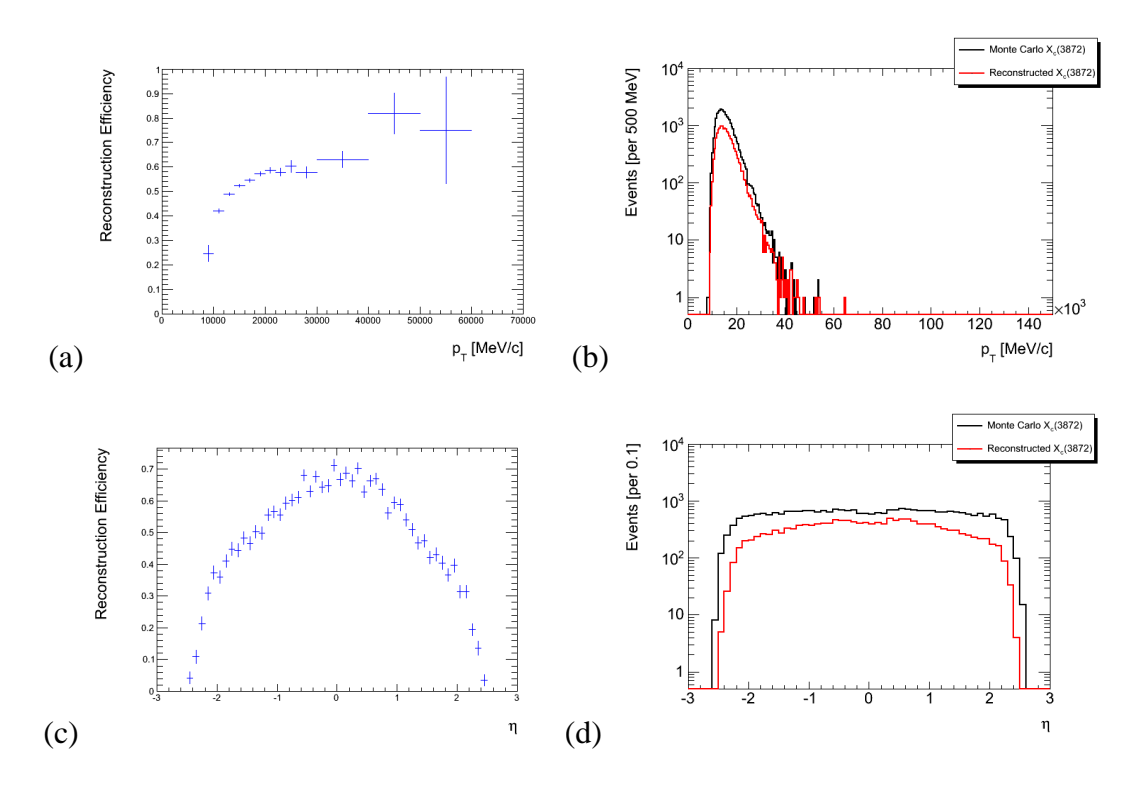


Figure 7.35. Reconstruction efficiency of the $X_c(3872)$ of the direct $pp \to X_c(3872)$ sample. (a) reconstruction efficiency vs. $X_c(3872)$ p_T, (b) $X_c(3872)$ p_T distribution, (c) reconstruction efficiency vs. $X_c(3872)$ η, (d) $X_c(3872)$ η distribution.

Figure 7.36-39 show the reconstruction efficiencies of muons, pions, the J/ψ , and the $X_c(3872)$, in the $B^+ \to X_c(3872)K^+$ events.

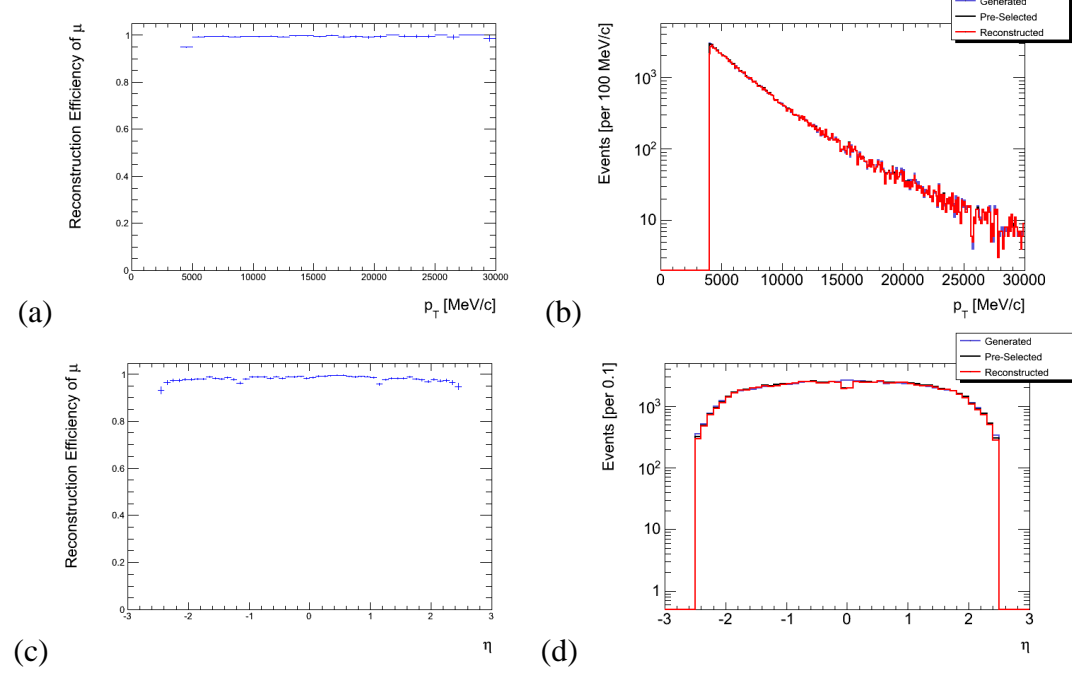


Figure 7.36. Reconstruction efficiency of muons of the $B^+ \to X_c(3872)K^+$ sample. (a) reconstruction efficiency vs. muon p_T , (b) muon p_T distribution, (c) reconstruction efficiency vs. muon η , (d) muon η distribution.

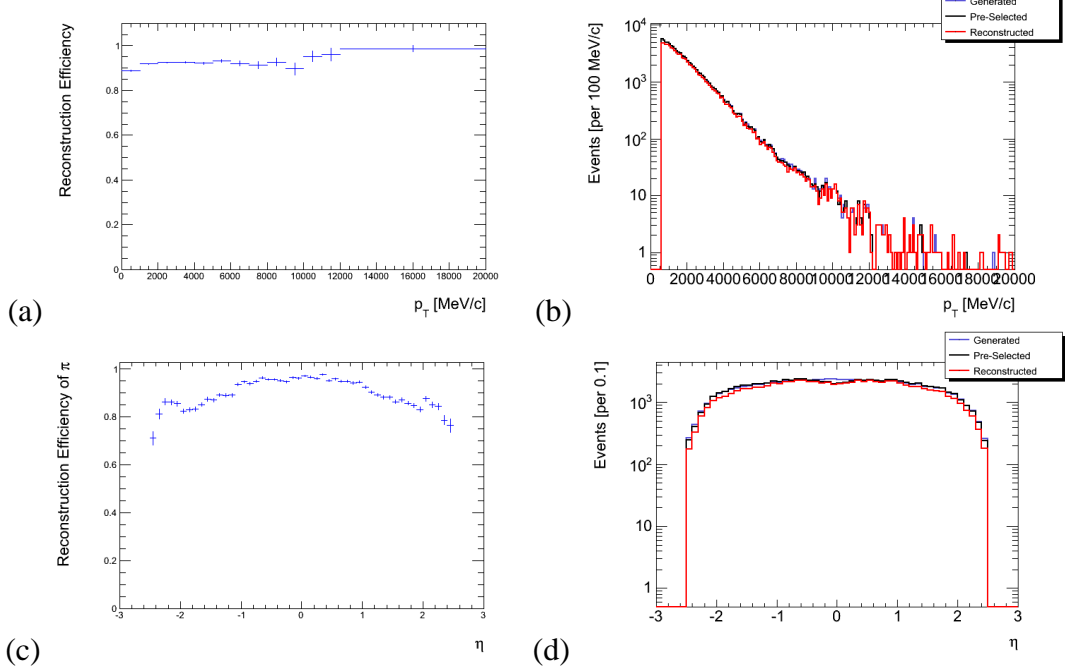


Figure 7.37. Reconstruction efficiency of pions of the $B^+ \to X_c(3872)K^+$ sample. (a) reconstruction efficiency vs. pion p_T , (b) pion p_T distribution, (c) reconstruction efficiency vs. pion η , (d) pion η distribution.

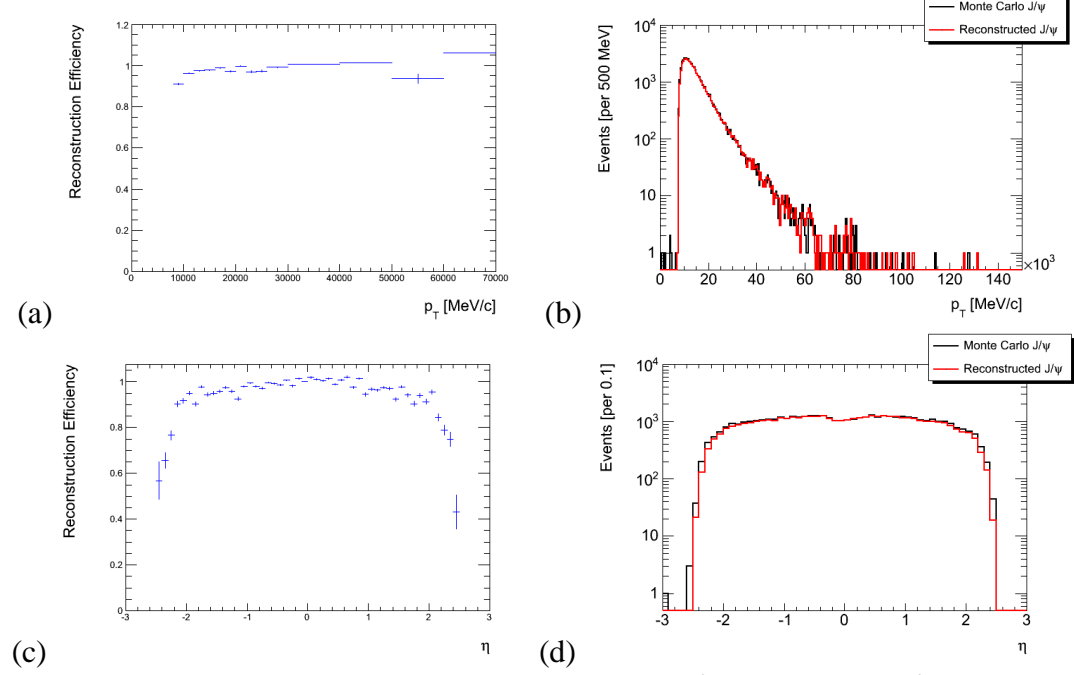


Figure 7.38. Reconstruction efficiency of the J/ψ of the in $B^+ \to X_c(3872)K^+$ sample. (a) reconstruction efficiency vs. J/ψ p_T, (b) J/ψ p_T distribution, (c) reconstruction efficiency vs. J/ψ η, (d) J/ψ η distribution.

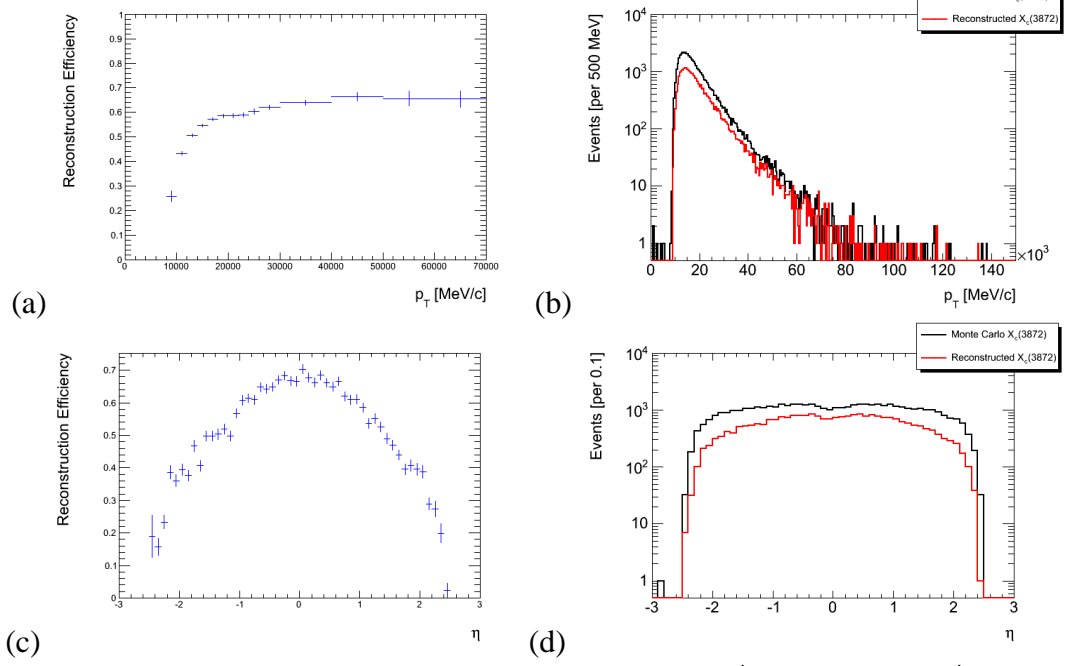


Figure 7.39. Reconstruction efficiency of the $X_c(3872)$ of the $B^+ \to X_c(3872)K^+$ sample. (a) reconstruction efficiency vs. $X_c(3872)$ p_T, (b) $X_c(3872)$ p_T distribution, (c) reconstruction efficiency vs. $X_c(3872)$ η, (d) $X_c(3872)$ η distribution.

CHAPTER 8

DATA SAMPLE, DATA ANALYSIS, AND RERULTS

8.1 Data Sample

Data analyzed in this dissertation research were pp collision events recorded by the ATLAS detector in 2010, 2011, at $\sqrt{s} = 7$ TeV at the LHC. The integrated luminosity is 39.9 pb⁻¹ in 2010, and is 2,402.7 pb⁻¹ in 2011 (up to data taking period K4). The overall integrated luminosity of the data is 2,442.5 pb⁻¹.

The data are analyzed over the ATLAS computing Grid, where the analysis codes are compiled. The analysis jobs are submitted to the Grid from a CERN computer. The derived AOD (DAOD) files, also named as DAOD_ONIAMUMU, or skim of the AOD, are rearranged by the ATLAS B-Physics group from the AOD files. The analyzed data are from good runs recorded when the ATLAS detector was functional. The data are analyzed with ATLAS software Release 17.0.2 with Good Run Lists (GRL) applied. The relative configuration about collision periods are kept in the good run list Extensible Markup Language (XML) files, which are created by the online ATLAS Good Run List Generator [42]. The delivered luminosities, the live-fraction corrected luminosities, and the prescales corrected luminosity with the trigger "EF_2mu4_Jpsimumu" are calculated by the online ATLAS Luminosity Calculator [43], and are listed in Table 8.1. The trigger "EF_2mu4_Jpsimumu" is recommended by the ATLAS B-Physics group, to collect most events for our analysis. This trigger selects 2 muons which from a

 J/ψ candidate, using the online data information. It is very effective at rejecting backgrounds. The name list of the data, the GRL list, and the integrated luminosities determined, are summarized below:

2012 Data files

- data10_7TeV.periodB.physics_MuonswBeam.PhysCont.DAOD_ONIAMUMU.repro05_v02/
- data10_7TeV.periodC.physics_MuonswBeam.PhysCont.DAOD_ONIAMUMU.repro05_v02/
- data10_7TeV.periodD.physics_MuonswBeam.PhysCont.DAOD_ONIAMUMU.repro05_v02/
- data10_7TeV.periodE.physics_MuonswBeam.PhysCont.DAOD_ONIAMUMU.repro05_v02/
- data10_7TeV.periodF.physics_MuonswBeam.PhysCont.DAOD_ONIAMUMU.repro05_v02/
- data10_7TeV.periodG.physics_MuonswBeam.PhysCont.DAOD_ONIAMUMU.repro05_v02/
- data10_7TeV.periodH.physics_MuonswBeam.PhysCont.DAOD_ONIAMUMU.repro05_v02/
- data10_7TeV.periodI.physics_MuonswBeam.PhysCont.DAOD_ONIAMUMU.repro05_v02/

2011 Data files

- data11_7TeV.periodB2.physics_Muons.PhysCont.DAOD_ONIAMUMU.repro09_v01/
- data11_7TeV.periodD.physics_Muons.PhysCont.DAOD_ONIAMUMU.repro09_v01/
- data11_7TeV.periodE.physics_Muons.PhysCont.DAOD_ONIAMUMU.repro09_v01/
- data11_7TeV.periodF2.physics_Muons.PhysCont.DAOD_ONIAMUMU.repro09_v01/
- data11_7TeV.periodF3.physics_Muons.PhysCont.DAOD_ONIAMUMU.repro09_v01/
- data11_7TeV.periodG.physics_Muons.PhysCont.DAOD_ONIAMUMU.repro09_v01/
- data11_7TeV.periodH.physics_Muons.PhysCont.DAOD_ONIAMUMU.repro09_v01/
- data11_7TeV.periodI.physics_Muons.PhysCont.DAOD_ONIAMUMU.repro09_v01/

- data11_7TeV.periodJ.physics_Muons.PhysCont.DAOD_ONIAMUMU.repro09_v01/
- data11_7TeV.periodK1.physics_Muons.PhysCont.DAOD_ONIAMUMU.repro09_v01/
- data11_7TeV.periodK2.physics_Muons.PhysCont.DAOD_ONIAMUMU.repro09_v01/
- data11_7TeV.periodK3.physics_Muons.PhysCont.DAOD_ONIAMUMU.repro09_v01/
- data11_7TeV.periodK4.physics_Muons.PhysCont.DAOD_ONIAMUMU.repro09_v01/

Good Run Lists

- data10_7TeV.periodAllYear_DetStatus-v21-pro05_CoolRunQuery-00-04-00_Muon.xml
- data11_7TeV.periodAllYear_DetStatus-v33-pro09-01_CoolRunQuery-00-04-00_Muon.xml

Table 8.1. (*Preliminary*) Luminosities by periods, calculated with trigger EF_2mu4_Jpsimumu.

| Luminosity | 2010 data | 2011 data | 2011 data | 2011 data | 2011 data | 2011 data | 2011 data |
|---------------------|-------------|-----------|-----------|-----------|-----------|-----------|-----------|
| (pb ⁻¹) | all periods | period B2 | period D | period E | period F2 | period F3 | period G |
| Delivered | 41.1054 | 12.9571 | 182.482 | 52.1980 | 134.867 | 19.4923 | 562.135 |
| Livefraction | 40.1783 | 12.7003 | 176.858 | 50.1759 | 131.565 | 18.3803 | 553,416 |
| Corrected | 40.1763 | 12.7003 | 170.056 | 30.1739 | 131.303 | 16.5605 | 333.410 |
| Prescale | 39.8896 | 12.6783 | 176.256 | 49.7661 | 130.928 | 18.3026 | 550.906 |
| Corrected | 37.8690 | 12.0763 | 170.230 | 49.7001 | 130.926 | 18.3020 | 330.900 |

| Luminosity | 2011 data |
|---------------------|-----------|-----------|-----------|-----------|-----------|-----------|-----------|
| (pb ⁻¹) | period H | period I | period J | period K1 | period K2 | period K3 | period K4 |
| Delivered | 276.231 | 403.182 | 237.454 | 246.847 | 208.697 | 90.8272 | 40.5601 |
| Livefraction | 271.133 | 393,313 | 231.387 | 240.534 | 204.298 | 88.5548 | 39.6148 |
| Corrected | 2/1.133 | 373.313 | 231.367 | 240.334 | 204.296 | 00.3340 | 37.0146 |
| Prescale | 270.281 | 391.76 | 230.565 | 239.892 | 203.601 | 88.2124 | 39,4216 |
| Corrected | 270.201 | 391.70 | 230.303 | 239.692 | 203.001 | 00.2124 | 39.4210 |

The event selection criteria used for data analysis are obtained from the Monte Carlo analysis, without truth matching. Referring to Appendix III, the event selections are declared in the analysis source code or in the job option file. The $X_c(3872)$ selection criteria of the tracks are considered to reject low momentum background and the cosmic ray events, to keep only well

measured tracks. The event selection criteria is similar to the measurements of the J/ψ and $\Upsilon(1S)$ productions in proton-proton collisions at $\sqrt{s} = 7$ TeV collected by the ATLAS detector [14] [44].

Analysis packages used are:

- TrkVertexAnalysisUtils-00-02-21
- JpsiUpsilonTools-00-00-36
- BPhysAnalysisObjects-00-00-42
- BPhysAnalysisTools-00-02-01
- JpsiUpsilonAlgs-00-00-32

Event selection criteria are:

$\mu^+\mu^-$ selection

- JpsiFinder Tool
- StacoMuonCollection
- Muons: $p_T > 4.0 \text{ GeV/c}$
- $\chi^2 < 10000.0$
- Oppositely charged pairs
- Number of pixel hits ≥ 1 , Number of SCT hits ≥ 6

π^{\pm} track selection

- $p_T > 0.6 \text{ GeV/c}$
- $|\eta| < 2.5$
- Number of pixel hits ≥ 1 , Number of SCT hits ≥ 6

Oppositely charged pairs

$J/\psi \pi^{+}\pi^{-}$ Selection ($\psi(2S), X_{c}(3872)$)

- J/ψ candidates with $|M(\mu\mu) M(J/\psi)| < 120 \text{ MeV}$
- I/ψ mass constraint
- $\mu^+\mu^-\pi^+\pi^-$ combinations with Prob(χ^2) > 0.02

8.2 Mass Spectrum of $I/\psi \pi^+\pi^-$ Combinations

The $J/\psi\pi^+\pi^-$ combinations are selected with the criteria described in Section 8.1. The mass values of the $J/\psi\pi^+\pi^-$ combinations are calculated, with the method described in Section 6.2, and the $J/\psi\pi^+\pi^-$ mass spectrum is obtained.

Figure 8.1 shows the preliminary inclusive $J/\psi\pi^+\pi^-$ mass distribution, in the mass region between 3,600.0 and 4,400.0 MeV/c². The prominent $\psi(2S)$ and the visible $X_c(3872)$ signals are observed. The PDG value of $\psi(2S)$ is 3,686.09 \pm 0.04 MeV/c², and the PDG value of the $X_c(3872)$ particle is 3,871.57 \pm 0.25 MeV/c². At the right-up corner plot, in the mass region between 3,750.0 and 4,050.0 MeV/c², the $X_c(3872)$ mass distribution is fitted with a single Gaussian as the signal, where the resolution is fixed at 12.0 MeV/c², and a 1st order of Chebyshev polynomial as the background. Table 8.2 gives the summary of the fitted $X_c(3872)$ signal. The observed mass value and the resolution consist with the expected value in the Monte Carlo analysis in Chapter 7, and the PDG value. The errors are statistical only.

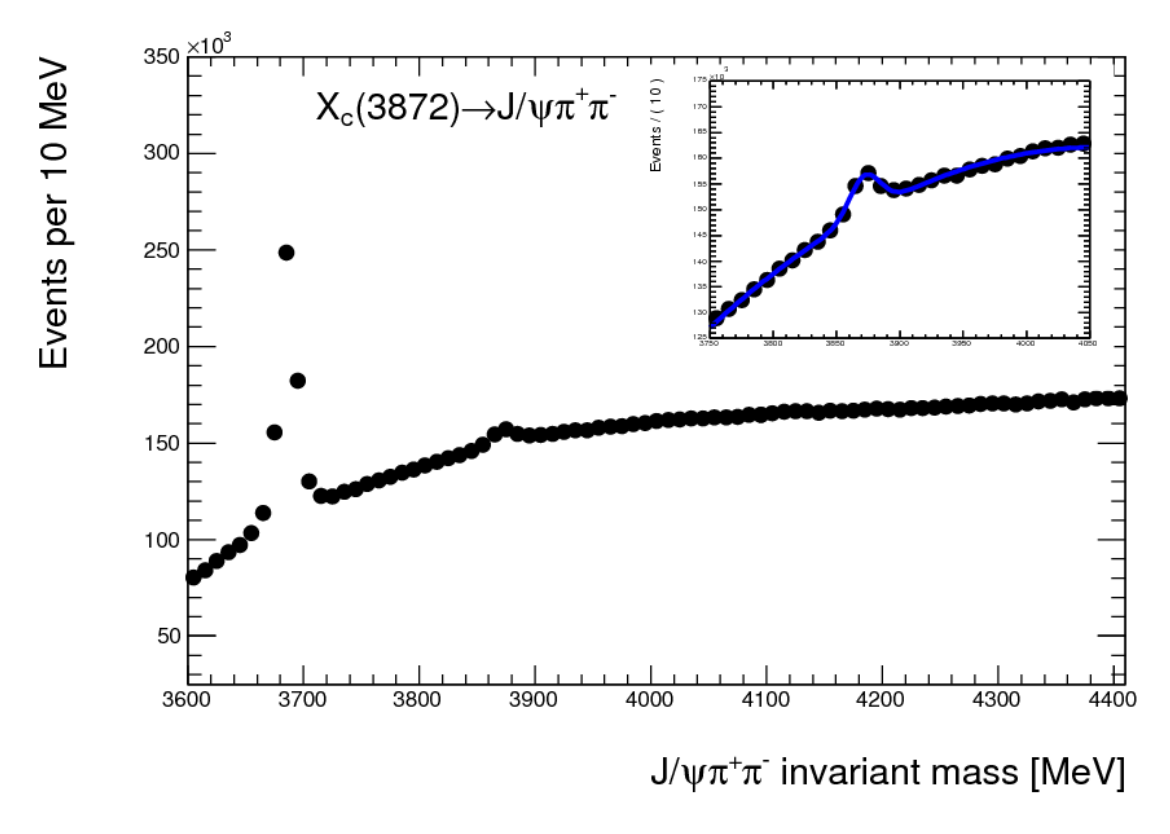


Figure 8.1. (*Preliminary*) Inclusive $J/\psi \pi^+\pi^-$ mass distribution.

Table 8.2. (*Preliminary*) Summary of the $X_c(3872) \rightarrow J/\psi \pi^+ \pi^-$.

| (<i>Preliminary</i>) Observation of $X_c(3872)$ | (<i>Preliminary</i>) Observation of $X_c(3872) \rightarrow J/\psi \pi^+ \pi^-$ | | | | | | | |
|---|--|--|--|--|--|--|--|--|
| Integrated Luminosity (pb ⁻¹) | 2,442.5 | | | | | | | |
| Mass (MeV/c ²) | $3,872.1 \pm 0.6$ | | | | | | | |
| Resolution (MeV/c ²) | 11.9 ± 1.4 | | | | | | | |
| Yield | $21,625 \pm 980$ | | | | | | | |
| χ^2 / dof value of fit | 1.09 | | | | | | | |

Figure 8.2 shows the raw yield distribution per 2000.0 MeV/c of p_T of the preliminary $X_c(3872)$ signal, where the errors are binomial. The $X_c(3872)$ p_T distribution is divided into several p_T intervals. Due to the transverse momenta selections of muons and pions, the $X_c(3872)$

yields are only shown for p_T greater than 10.0 GeV/c for the differential cross-section study. The $X_c(3872)$ events with p_T less than 10.0 GeV/c are checked for the systematic uncertainty study. The ranges of the $X_c(3872)$ p_T intervals, from (a) to (n), are listed below. They are used in Sections 8.3 and 8.4 in the same way.

- p_T interval (a): $X_c(3872)$ $p_T < 10,000.0$ (MeV/c)
- p_T interval (b): $10,000.0 < X_c(3872) p_T < 12,000.0 (MeV/c)$
- p_T interval (c): 12,000.0 < X_c (3872) p_T < 14,000.0 (MeV/c)
- p_T interval (d): 14,000.0 < X_c (3872) p_T < 16,000.0 (MeV/c)
- p_T interval (e): $16,000.0 < X_c(3872) p_T < 18,000.0 (MeV/c)$
- p_T interval (f): 18,000.0 < X_c (3872) p_T < 20,000.0 (MeV/c)
- p_T interval (g): 20,000.0 < X_c (3872) p_T < 22,000.0 (MeV/c)
- p_T interval (h): 22,000.0 < X_c (3872) p_T < 24,000.0 (MeV/c)
- p_T interval (i): 24,000.0 < X_c (3872) p_T < 26,000.0 (MeV/c)
- p_T interval (j): 26,000.0 < X_c (3872) p_T < 30,000.0 (MeV/c)
- p_T interval (k): 30,000.0 < X_c (3872) p_T < 40,000.0 (MeV/c)
- p_T interval (1): $40,000.0 < X_c(3872) p_T < 50,000.0 (MeV/c)$
- p_T interval (m): 50,000.0 < X_c (3872) p_T < 60,000.0 (MeV/c)
- p_T interval (n): $60,000.0 < X_c(3872) p_T < 70,000.0 (MeV/c)$

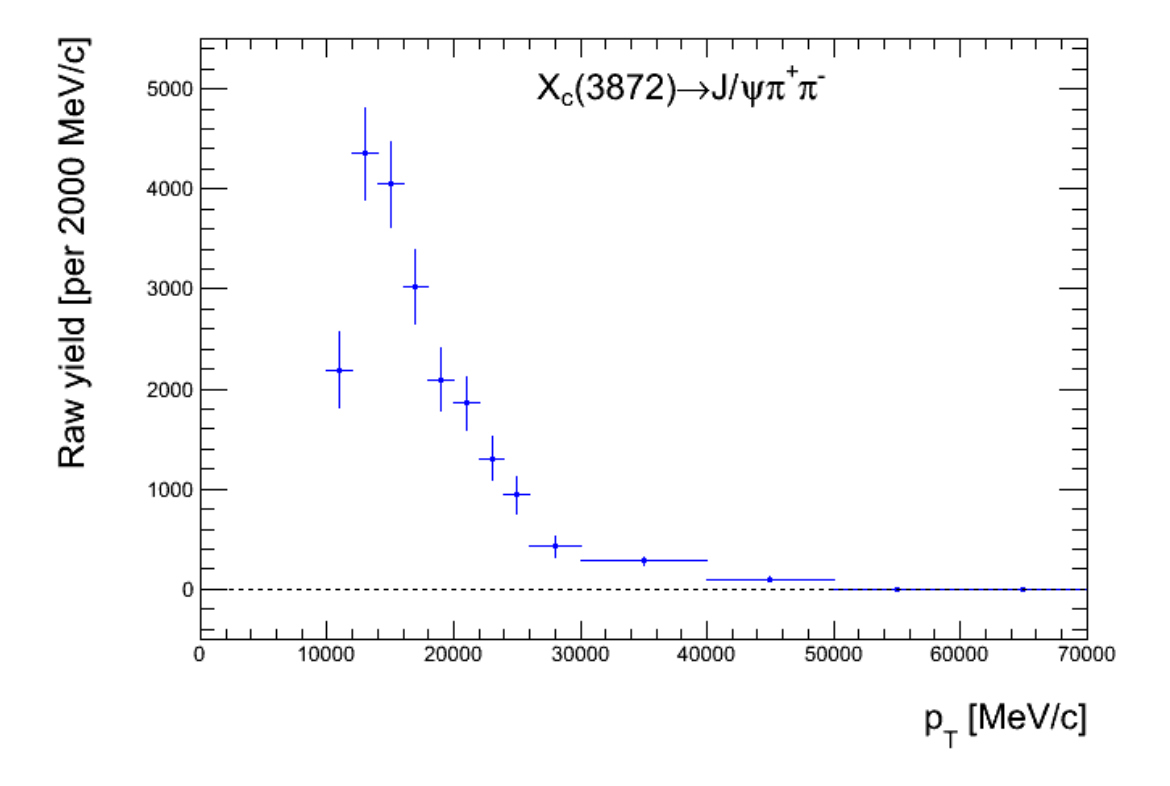


Figure 8.2. (Preliminary) Raw yield distribution of the fitted $X_c(3872)$ signals vs. p_T .

In the $J/\psi\pi^+\pi^-$ mass spectrum, the $\psi(2S)$ and the $X_c(3872)$ signals are clearly observed. No other significant enhancement is observed in the $J/\psi\pi^+\pi^-$ mass spectrum. We find no evidence for new states within the mass range examined. This analysis establishes that ATLAS can detect $X_c(3872)$ -like new particles in the $J/\psi\pi^+\pi^-$ final state, and with current data sample, no new states have been observed.

8.3 Systematic Uncertainties

In addition to the statistical uncertainties, the systematic uncertainties affect the measurement of the yield. The sources for the systematic errors are listed in Table 8.3.

Table 8.3. (*Preliminary*) Sources of systematic errors.

| Name | Effects to consider | Uncertainties | |
|--------------------------------|---|---------------|--|
| | Done in this dissertation. | | |
| Monte Carlo Models | Prompt production, B decays | 3.2 % | |
| Monte Carlo Statistics | Statistical error on efficiency | 0.29 % | |
| Imperfection in Monte | μ ID, π tracking, mass/p _T resolution | 0.5 % | |
| Carlo simulation | (To be taken from J/ψ , Υ papers) [14] [44] | 0.5 % | |
| Fit to the data | Resolution, background parameter, signal form | 8.6 % | |
| $BR(J/\psi \to \mu^+ \mu^-)$ | From PDG [3] | 0.06 % | |
| Error on the luminosity | Provided by the LHC [45] | 3.4 % | |
| | Not done in this dissertation. | | |
| Trigger scale | prescale corrected / delivered | N/A | |
| Edge effect at low X_c p_T | p _T resolution, p _T spectrum | N/A | |
| Pileup effects | Multiple vertices | N/A | |
| Bunch crossings | Variation of collisions | N/A | |

The systematic uncertainties are partially studies in this dissertation. The difference in reconstruction efficiencies due to the Monte Carlo models are presented in Chapter 7. The fitting methods in this dissertation are described in previous sections. More fitting results in this section give the uncertainty ranges of the yield. The event reconstructions in the Monte Carlo analysis reveal the systematic uncertainties, from the event counting, the detection efficiency error, and the fitting, to be described below. The detection efficiencies and correlated error propagations come from the errors of the Monte Carlo event generation, the online trigger efficiency, the offline filter efficiency, the event reconstruction efficiency, and the luminosity uncertainty (\sim 3.4%) [45]. The pile up effect, due to changes in the LHC bunch crossings, and the bias caused by detector resolution at low p_T of the X_c (3872) are not studied in this dissertation.

The systematic errors on the estimated $X_c(3872)$ yield are evaluated. Table 8.4 lists the numbers of signal events (described below), the reconstruction efficiencies, the fit-to-count ratios, and the errors obtained from the combined sample of the direct $pp \to X_c(3872)$ and the $B^+ \to X_c(3872)K^+$. The explanations are provided below.

- N_A : Number of Monte Carlo truth-matched $X_c(3872)$ events after Cut-0 has been applied, in each p_T (generated truth p_T value) interval,
- N_B : Number of reconstructed Monte Carlo $X_c(3872)$ events after Cut-0, in each p_T (reconstructed value) interval,
- N_C : Number of detected Monte Carlo truth-matched $X_c(3872)$ events after Cut-10, in each p_T (generated truth p_T value) interval,
- N_D : Number of detected, truth-matched Monte Carlo $X_c(3872)$ events after Cut-10, in each p_T (reconstructed value) interval, by count.
- N_{fit}: Number of fitted Monte Carlo $X_c(3872) \rightarrow J/\psi \pi^+ \pi^-$ events after Cut-10, where the $X_c(3872)$ signal is fitted with double Gaussians and a Chebyshev polynomial as the background.
- ε_1 : Reconstruction efficiency (N_D/N_A) with binomial error, in each p_T interval.
- ϵ_2 : Reconstruction efficiency (N_C / N_A) with binomial error, in each p_T interval.
- ε_3 : Reconstruction efficiency (N_D/N_B) with binomial error, in each p_T interval.
- ε_4 : Reconstruction efficiency (N_C / N_B) with binomial error, in each p_T interval.
- N_{fit}/N_D : The ratio of the number of the fitted $X_c(3872)$ to the number of $X_c(3872)$ by count after Cut-10.
- ϵ_1 ': Reconstruction efficiency ϵ_1 corrected by (N_{fit} / N_D) , in each p_T interval, to account for

the effect of the fit. The error is binomial.

- ϵ_2 ': Reconstruction efficiency ϵ_2 corrected by (N_{fit} / N_D) , in each p_T interval, to account for the effect of the fit. The error is binomial.
- ϵ_3 ': Reconstruction efficiency ϵ_3 corrected by (N_{fit} / N_D) , in each p_T interval, to account for the effect of the fit. The error is binomial.
- ϵ_4 ': Reconstruction efficiency ϵ_4 corrected by (N_{fit} / N_D) , in each p_T interval, to account for the effect of the fit. The error is binomial.

Table 8.4. (*Preliminary*) Summary of Monte Carlo study of $X_c(3872)$ detection efficiencies.

| p _T intervals | (a) | (b) | (c) | (d) | (e) | (f) | (g) |
|-----------------------------------|-------------|-------------|-------------|-------------|-------------|-------------|-------------|
| N _A | 630 | 7997 | 15260 | 14914 | 11434 | 7862 | 5295 |
| N _B | 1210 | 7279 | 12320 | 11407 | 8729 | 5958 | 4097 |
| N _C | 162 | 3426 | 7607 | 8004 | 6416 | 4557 | 3103 |
| N _D | 161 | 3426 | 7605 | 7996 | 6412 | 4566 | 3105 |
| N_{fit} | 153±91 | 3339±621 | 7306±1409 | 7636±1013 | 6286±833 | 4421±830 | 2995±632 |
| ϵ_1 | 0.256±0.017 | 0.428±0.006 | 0.498±0.004 | 0.536±0.004 | 0.561±0.005 | 0.581±0.006 | 0.586±0.007 |
| ϵ_2 | 0.257±0.017 | 0.428±0.006 | 0.498±0.004 | 0.537±0.004 | 0.561±0.005 | 0.580±0.006 | 0.586±0.007 |
| ϵ_3 | 0.133±0.010 | 0.471±0.006 | 0.617±0.004 | 0.701±0.004 | 0.735±0.005 | 0.766±0.005 | 0.758±0.007 |
| ε ₄ | 0.134±0.010 | 0.471±0.006 | 0.617±0.004 | 0.702±0.004 | 0.735±0.005 | 0.765±0.005 | 0.757±0.007 |
| $N_{\rm fit}$ / $N_{\rm D}$ | 0.950310 | 0.974605 | 0.960683 | 0.954977 | 0.980349 | 0.968243 | 0.964573 |
| ϵ_{l} | 0.243±0.017 | 0.418±0.005 | 0.479±0.004 | 0.512±0.004 | 0.550±0.005 | 0.562±0.005 | 0.566±0.007 |
| ε2' | 0.244±0.017 | 0.418±0.005 | 0.479±0.004 | 0.513±0.004 | 0.550±0.005 | 0.561±0.005 | 0.565±0.007 |
| ε3' | 0.126±0.010 | 0.459±0.006 | 0.593±0.004 | 0.669±0.004 | 0.720±0.005 | 0.742±0.005 | 0.731±0.006 |
| ε ₄ ' | 0.127±0.009 | 0.459±0.006 | 0.593±0.004 | 0.670±0.004 | 0.721±0.005 | 0.741±0.005 | 0.731±0.006 |
| | | | | | | | |
| p _T intervals | (h) | (i) | (j) | (k) | (1) | (m) | (n) |
| N _A | 3544 | 2410 | 2950 | 2750 | 738 | 269 | 207 |
| N _B | 2698 | 1834 | 2321 | 2166 | 616 | 217 | 176 |
| $N_{\rm C}$ | 2095 | 1428 | 1819 | 1763 | 491 | 180 | 135 |
| N_{D} | 2080 | 1457 | 1813 | 1758 | 494 | 177 | 136 |
| N_{fit} | 1997±615 | 1403±250 | 1818±261 | 1751±125 | 486±147 | 177±46 | 141±48 |
| ϵ_1 | 0.587±0.008 | 0.605±0.010 | 0.615±0.009 | 0.639±0.009 | 0.669±0.017 | 0.658±0.029 | 0.657±0.033 |
| ϵ_2 | 0.591±0.008 | 0.593±0.010 | 0.617±0.009 | 0.641±0.009 | 0.665±0.017 | 0.669±0.029 | 0.652±0.033 |
| €3 | 0.771±0.008 | 0.794±0.009 | 0.781±0.009 | 0.812±0.008 | 0.802±0.016 | 0.816±0.026 | 0.773±0.032 |
| €4 | 0.777±0.008 | 0.779±0.010 | 0.784±0.009 | 0.814±0.008 | 0.797±0.016 | 0.829±0.026 | 0.767±0.032 |
| N _{fit} / N _D | 0.960096 | 0.962937 | 1.002757 | 0.996018 | 0.983805 | 1 | 1.036764 |
| ϵ_1 ' | 0.563±0.008 | 0.582±0.010 | 0.616±0.009 | 0.637±0.009 | 0.658±0.017 | 0.658±0.029 | 0.681±0.034 |
| ε2' | 0.568±0.008 | 0.571±0.010 | 0.618±0.009 | 0.639±0.009 | 0.655±0.017 | 0.669±0.029 | 0.676±0.034 |
| ε ₃ ' | 0.740±0.008 | 0.765±0.010 | 0.783±0.009 | 0.808±0.009 | 0.789±0.016 | 0.816±0.026 | 0.801±0.033 |
| ε ₄ ' | 0.746±0.008 | 0.750±0.009 | 0.786±0.009 | 0.811±0.008 | 0.784±0.016 | 0.829±0.026 | 0.795±0.033 |

Figure 8.3 shows the reconstruction efficiency of the $X_c(3872)$, with and without the $N_{\rm fit}$ / $N_{\rm D}$, of the combined sample of the direct $pp \to X_c(3872)$ and the $B^+ \to X_c(3872)K^+$ events. The major difference between the four reconstruction efficiencies distributions (ϵ_1 , ϵ_2 , ϵ_3 , and ϵ_4)

is due to the reconstruction rate at Cut-0, i.e. finding all $\mu^+\mu^-\pi^+\pi^-$ tracks, as explained in Section 7.2. The corrected efficiencies are used in determined the $X_c(3872)$ yield.

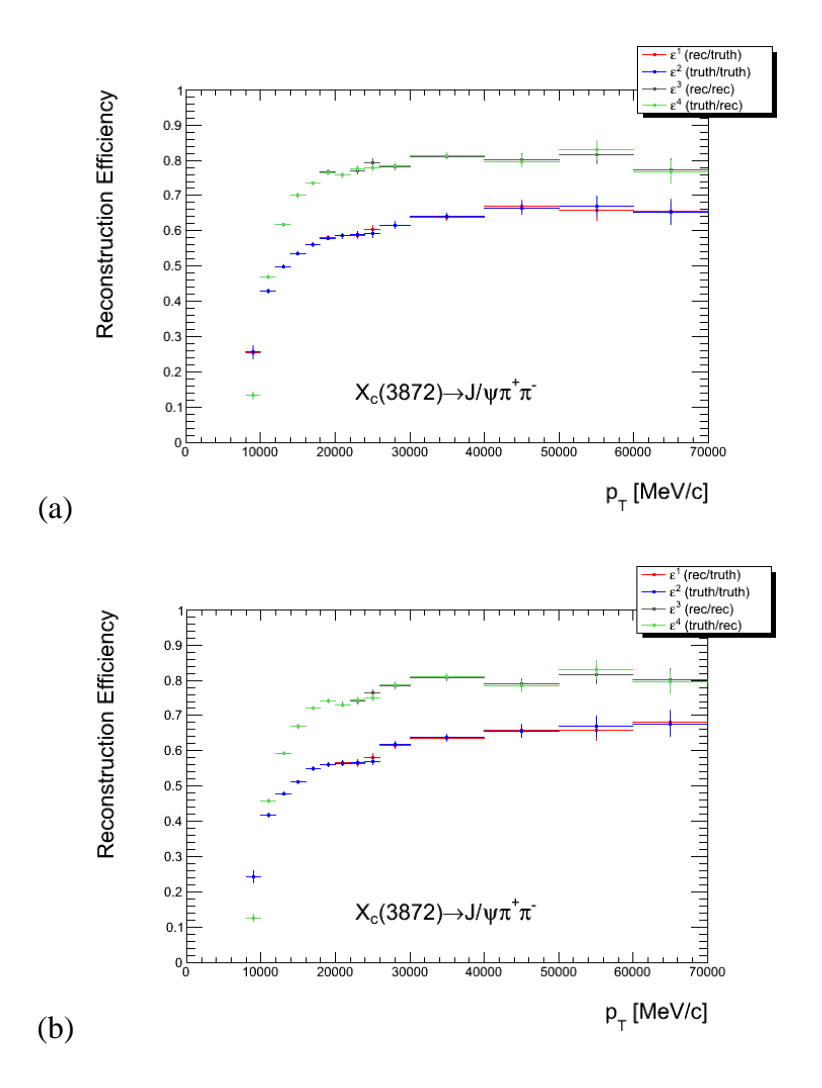


Figure 8.3. (*Preliminary*) Reconstruction efficiencies of the $X_c(3872)$ vs. p_T , of the combined Monte Carlo sample. (a) Without the N_{fit} / N_D correction. (b) With the N_{fit} / N_D correction.

The systematic uncertainty of the fitting due to $X_c(3872)$ mass resolution is considered. In Table 8.2, $X_c(3872)$ events are obtained by fits with mass resolutions fixed at 12.0, 10.6, and 13.4 MeV/ c^2 , in p_T intervals, to evaluate the deviation of differential cross-sections. The change in resolution corresponds to the error on the mass resolution. Figure 8.4 shows the mass distributions with the observed data $X_c(3872)$ fitted with a single Gaussian function, the mean mass values fixed at 3872.0 MeV/c^2 and a resolution of 12.0 MeV/c^2 , in all p_T intervals, and a 1^{st} order of Chebyshev polynomial as the background. Table 8.5 lists the raw yields from the fits. Figure 8.5 and Figure 8.6 show the mass distributions with the observed $X_c(3872)$ fitted with single Gaussian functions, the mass mean values fixed at $3.872.0 \text{ MeV/c}^2$ with resolutions 10.6 MeV/c^2 , and 13.4 MeV/c^2 , respectively. Table 8.6 - 8.7 list the raw yields of the fitting results.

Table 8.5. (*Preliminary*) $X_c(3872)$ yields with mass resolution fixed at 12.0 MeV/c² in the fit.

| p _T interval | (a) | (b) | (c) | (d) | (e) | (f) | (g) |
|-------------------------|----------|----------|----------|----------|----------|----------|----------|
| Yield | N/A | 2192±374 | 4355±457 | 4048±426 | 3021±367 | 2095±311 | 1859±263 |
| p _T interval | (h) | (i) | (j) | (k) | (1) | (m) | (n) |
| Yield | 1309±221 | 943±188 | 860±211 | 1425±213 | 491±114 | 0±52 | 0±6.8 |

Table 8.6. (Preliminary) $X_c(3872)$ yields with mass resolution fixed at 10.6 MeV/c² in the fit.

| 14010 0:0: (1 | Tettilitett y j | 116(00, 2) | jields with mass resolution inted at 10.0 Me v/e in the int | | | | | |
|-------------------------|-----------------|------------|---|----------|----------|----------|----------|--|
| p_T interval | (a) | (b) | (c) | (d) | (e) | (f) | (g) | |
| Yield | N/A | 2022±341 | 3983±417 | 3713±387 | 2725±335 | 1878±284 | 1675±240 | |
| p _T interval | (h) | (i) | (j) | (k) | (1) | (m) | (n) | |
| Yield | 1220±201 | 841±172 | 826±193 | 1327±195 | 439±105 | 0±47 | 0±6.3 | |

Table 8.7. (Preliminary) $X_c(3872)$ yields with mass resolution fixed at 13.4 MeV/c² in the fit.

| p _T interval | (a) | (b) | (c) | (d) | (e) | (f) | (g) |
|-------------------------|----------|----------|----------|----------|----------|----------|----------|
| Yield | N/A | 2374±408 | 4722±498 | 4369±465 | 3304±402 | 2286±339 | 2034±286 |
| p _T interval | (h) | (i) | (j) | (k) | (1) | (m) | (n) |
| Yield | 1390±240 | 1041±205 | 885±230 | 1517±232 | 541±125 | 0±59 | 0±7.4 |

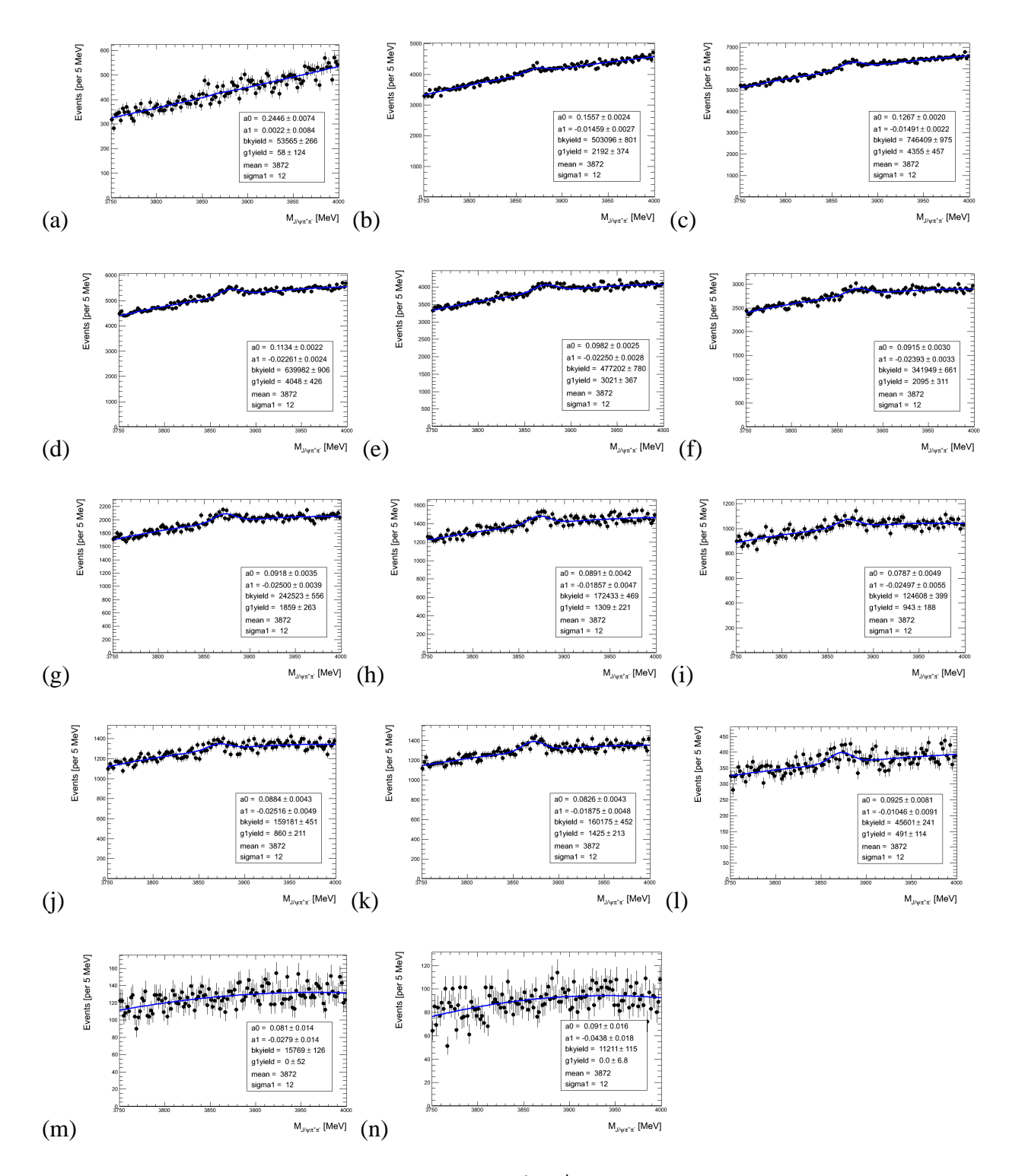


Figure 8.4. (*Preliminary*) Mass distributions of $J/\psi\pi^+\pi^-$, fitted with a single Gaussian signal, the mass mean values fixed at 3,872.0 MeV/c² with resolution 12.0 MeV/c², in p_T intervals.

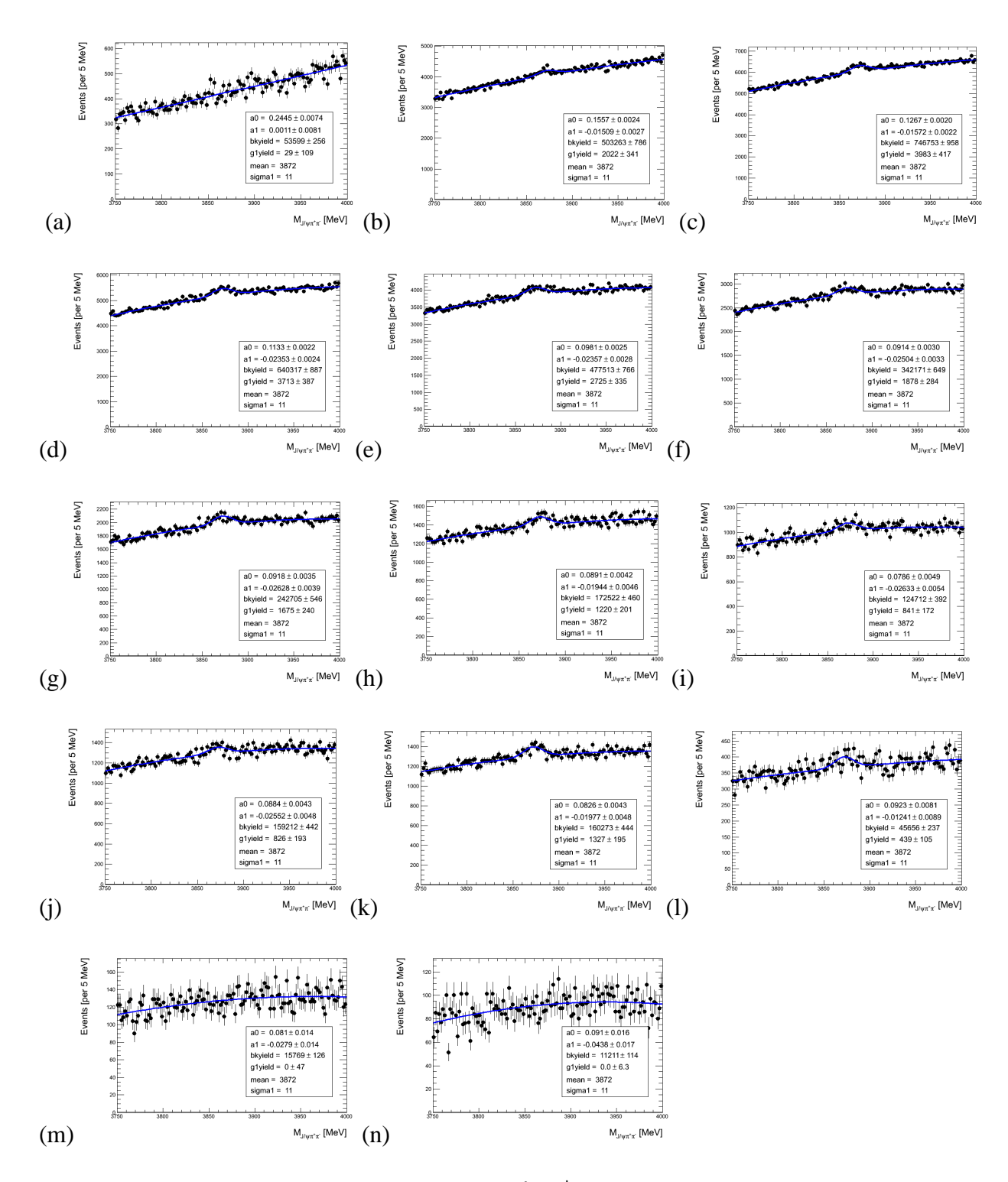


Figure 8.5. (*Preliminary*) Mass distributions of $J/\psi\pi^+\pi^-$, fitted with a single Gaussian signal, the mass mean values fixed at 3,872.0 MeV/c² with resolution 10.6 MeV/c², in p_T intervals.

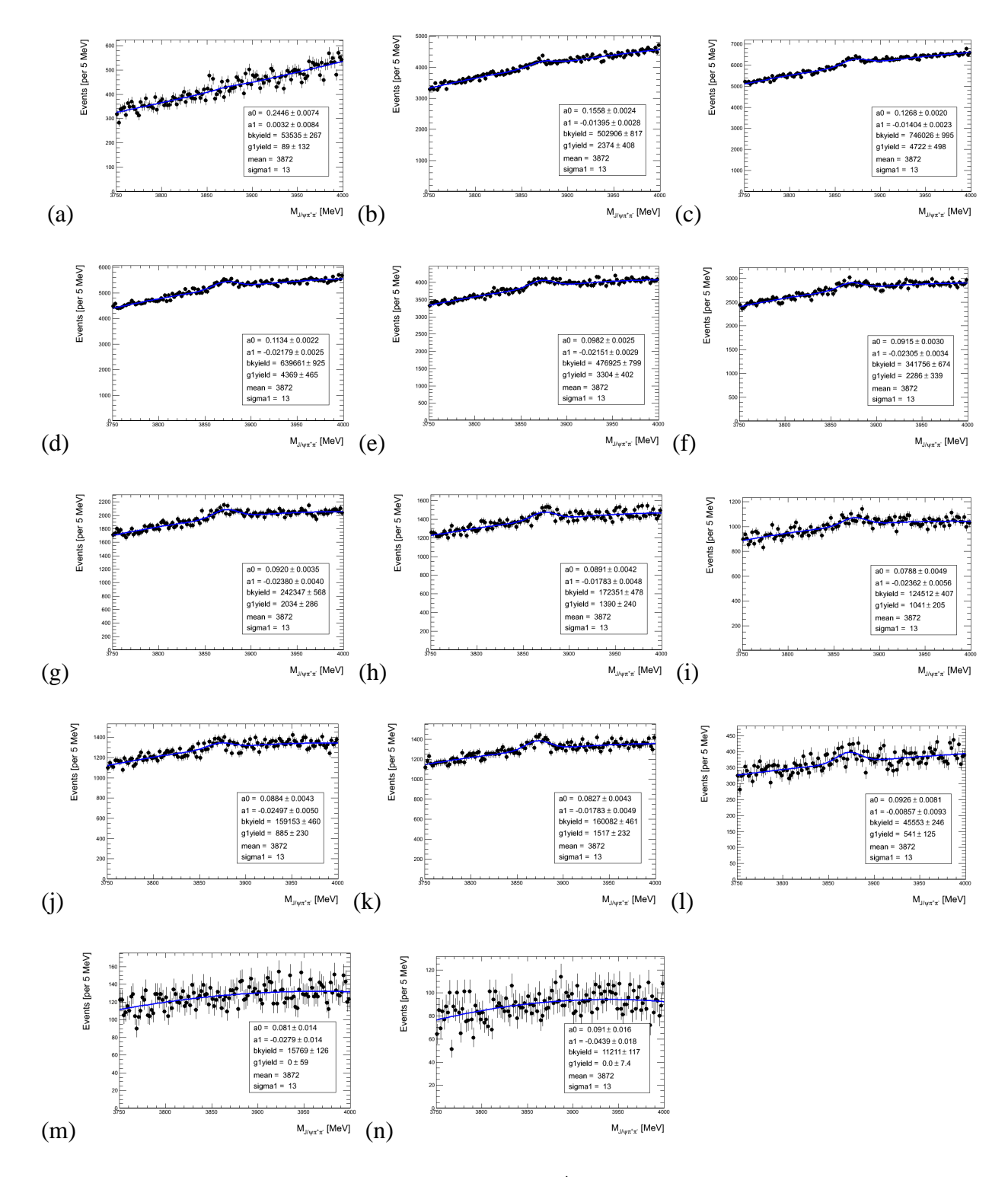


Figure 8.6. (*Preliminary*) Mass distributions of $J/\psi\pi^+\pi^-$, fitted with a single Gaussian signal, the mass mean values fixed at 3,872.0 MeV/c² with resolution 13.4 MeV/c², in p_T intervals.

The 2010 data and data from periods B to K4 in 2011 are checked for time dependent variations. The pileup effect (where multiple *pp* annihilation events are recorded as one event) with period by period variations needs to be understood. 2010 data with "repro05_v02" is used in this dissertation. There is no pileup-setup in 2010 data, as the LHC luminosity was much lower, and the comparable Monte Carlo version MC09 is not used. 2011 data with "repro09_v01", periods B to K, is used in this dissertation. The MC10b, where the names of datasets ending with AMI tag "r2297_r2300", is used in this dissertation, and is comparable to 2011 data with "repro08" and "repro09". The bunch train pileup-setup: three trains with 9BC=225ns separation, within trains are 36 filled bunches with 50ns bunch separation and variable < n_MB >.

The pileup effect exists in 2011 data, and the reconstruction efficiency study with MC10b version of the simulated events as described, in Chapter 7, is thought to be adequate for the data. In this section, the pileup effect is examined with the $\psi(2S)$ yields per unit luminosity over all the data periods. The $J/\psi\pi^+\pi^-$ mass distributions are examined and the yields of $\psi(2S)$ are determined by fits. The variation of the $\psi(2S)$ yields per 1 fb⁻¹ over the periods illustrates the effect due to the pileup effect and other biases which depend on the time. Figure 8.7 shows the $J/\psi\pi^+\pi^-$ mass distribution with fits to the $\psi(2S)$ signals, of the 14 periods, from 2010 data, 2011 periods B2, D, E, F2, F3, G, H, I, J, K1, K2, K3, to K4. Table 8.8 shows the fitting results, the $\psi(2S)$ yields with errors, the luminosities, and the calculated $\psi(2S)$ yields per 1 fb⁻¹, by periods. Figure 8.8 shows the $\psi(2S)$ yields per 1fb⁻¹ for each period. The trend in the Figure 8.8 shows that the estimated $\psi(2S)$ yields per 1fb⁻¹ with the 2010 data, and the dependency on time behavior of the 2011 data.

Besides, the possible pileup effect and time dependency of the $X_c(3872)$ is also examined. Figure 8.9 shows the $J/\psi\pi^+\pi^-$ mass distribution with fits to the $X_c(3872)$ signals in all the 14 periods. Table 8.9 shows the statistical results, the $X_c(3872)$ yields with errors, the luminosities, and the calculated $X_c(3872)$ yields per 1 fb⁻¹, by periods. Figure 8.10 shows the $X_c(3872)$ yields per 1fb⁻¹ for each period. The fluctuation is more dramatic, owing to the relative few yields of the $X_c(3872)$ particle and the short periods. The errors are large with the $X_c(3872)$ signal and the pileup effect is not very conclusive. However the period dependency trend observed with the $\psi(2S)$ in Figure 8.8 is quite firm. A set of correction factors from Figure 8.8 can be extracted to correct for the systematic bias. This will be carried out in the journal preparation phase.

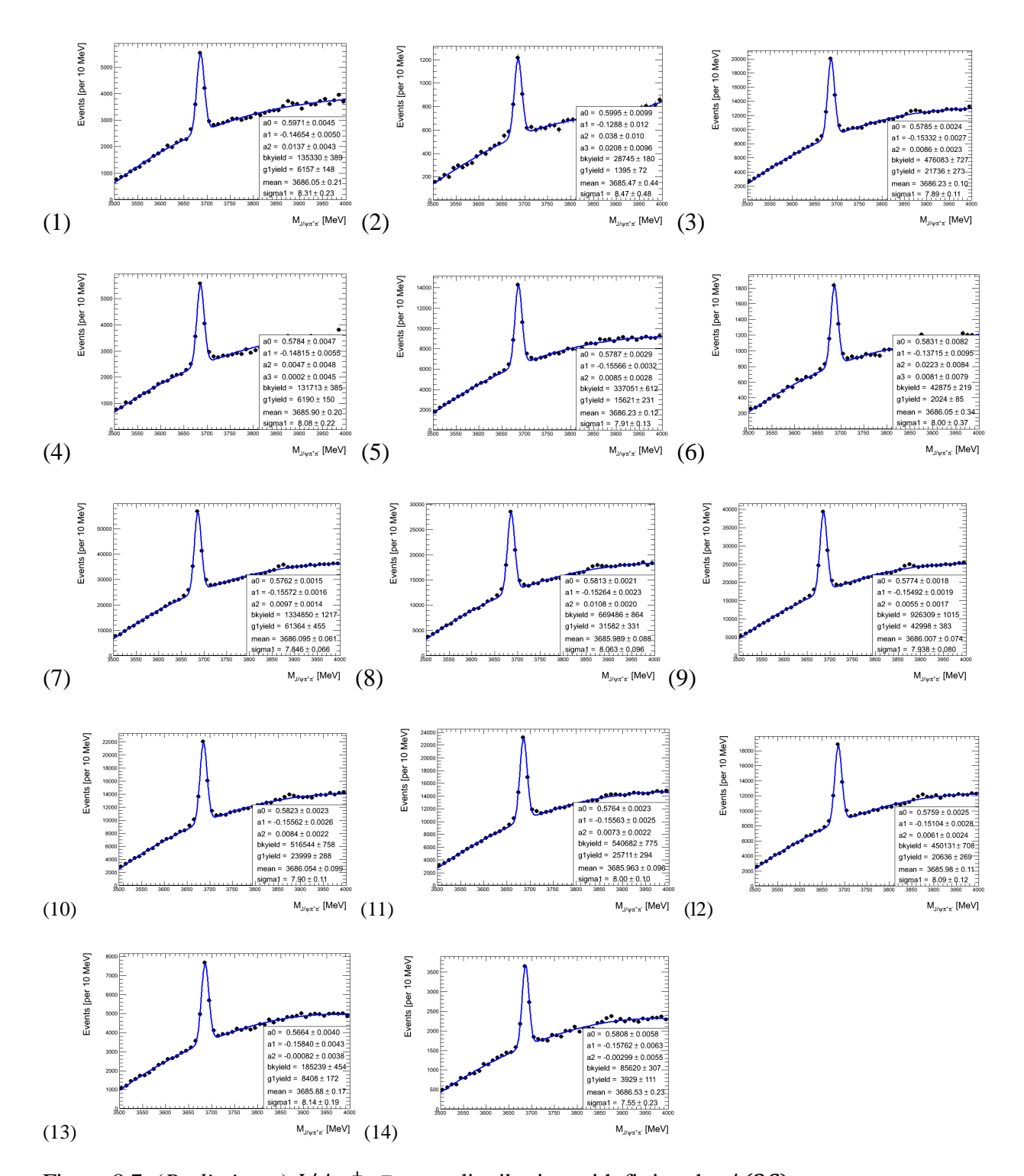


Figure 8.7. (*Preliminary*) $J/\psi \pi^+\pi^-$ mass distribution with fitting the $\psi(2S)$ mass.

| Table 8.8. (<i>Preliminary</i>) Data $\psi(2S)$ yields, by periods, obtained from fits to $J/\psi \pi^+\pi^-$ may | ass |
|---|-----|
| distributions. | |

| Period | (1) 2010 | (2) 2011 B2 | (3) 2011 D | (4) 2011 E | (5) 2011 F2 | (6) 2011 F3 | (7) 2011 G |
|----------------------------------|------------------|------------------|------------------|------------------|------------------|------------------|-----------------|
| $\psi(2S)$ Yield | 6157±148 | 1395±72 | 21736±273 | 6190±150 | 15621±231 | 2024±85 | 61364±455 |
| Mean (MeV/c ²) | 3686.1±0.2 | 3685.5±0.4 | 3686.2±0.1 | 3685.9±0.2 | 3686.2±0.1 | 3686.1±0.3 | 3686.1±0.1 |
| Resolution (MeV/c ²) | 8.31±0.23 | 8.47±0.48 | 7.89±0.11 | 8.08±0.22 | 7.91±0.13 | 8.00±0.37 | 7.85±0.07 |
| Luminosity (fb ⁻¹) | 0.040 | 0.013 | 0.176 | 0.050 | 0.131 | 0.018 | 0.551 |
| Yield / fb ⁻¹ | 154388 ± 3711 | 110102 ± 5682 | 123317 ± 1548 | 124372 ± 3013 | 119308 ± 1764 | 110601 ± 4644 | 111386 ± 825 |

| Period | (8) 2011 H | (9) 2011 I | (10) 2011 J | (11) 2011K1 | (12) 2011K2 | (13) 2011K3 | (14) 2011K4 |
|----------------------------------|------------------|-----------------|------------------|------------------|------------------|-----------------|-----------------|
| $\psi(2S)$ Yield | 31582±331 | 42998±383 | 23999±288 | 25711±294 | 20636±269 | 8408±172 | 3929±111 |
| Mean (MeV/c ²) | 3686.0±0.1 | 3686.0±0.1 | 3686.1±0.1 | 3686.0±0.1 | 3686.0±0.1 | 3685.9±0.2 | 3686.5±0.2 |
| Resolution (MeV/c ²) | 8.06±0.10 | 7.94±0.08 | 7.09±0.11 | 8.00±0.10 | 8.09±0.12 | 8.14±0.19 | 7.55±0.23 |
| Luminosity (fb ⁻¹) | 0.270 | 0.392 | 0.231 | 0.240 | 0.204 | 0.088 | 0.039 |
| Yield / fb ⁻¹ | 116849 ± 1224 | 109755 ± 977 | 104085 ± 1249 | 107178 ± 1225 | 101355 ± 1321 | 95317 ± 1949 | 99670 ± 2815 |

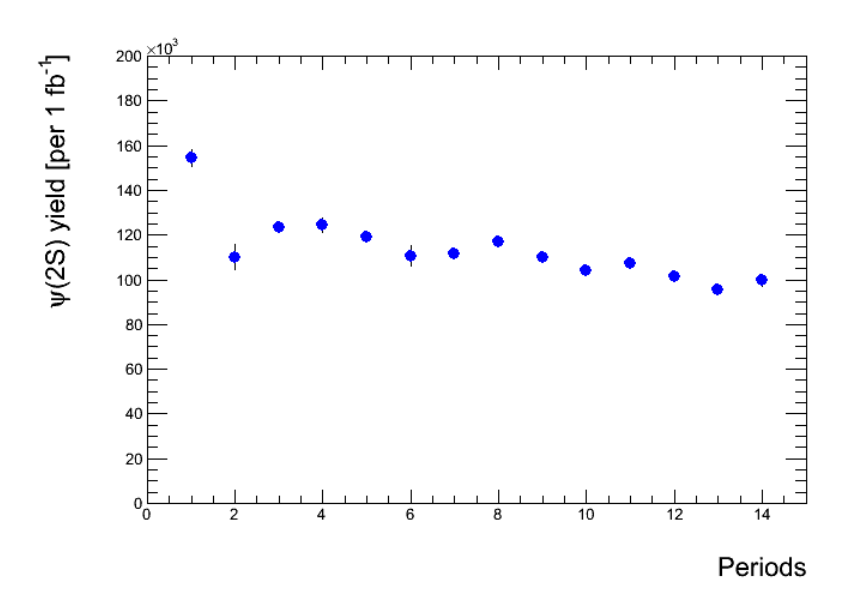


Figure 8.8. (*Preliminary*) Data $\psi(2S)$ yields per 1fb⁻¹ for each period.

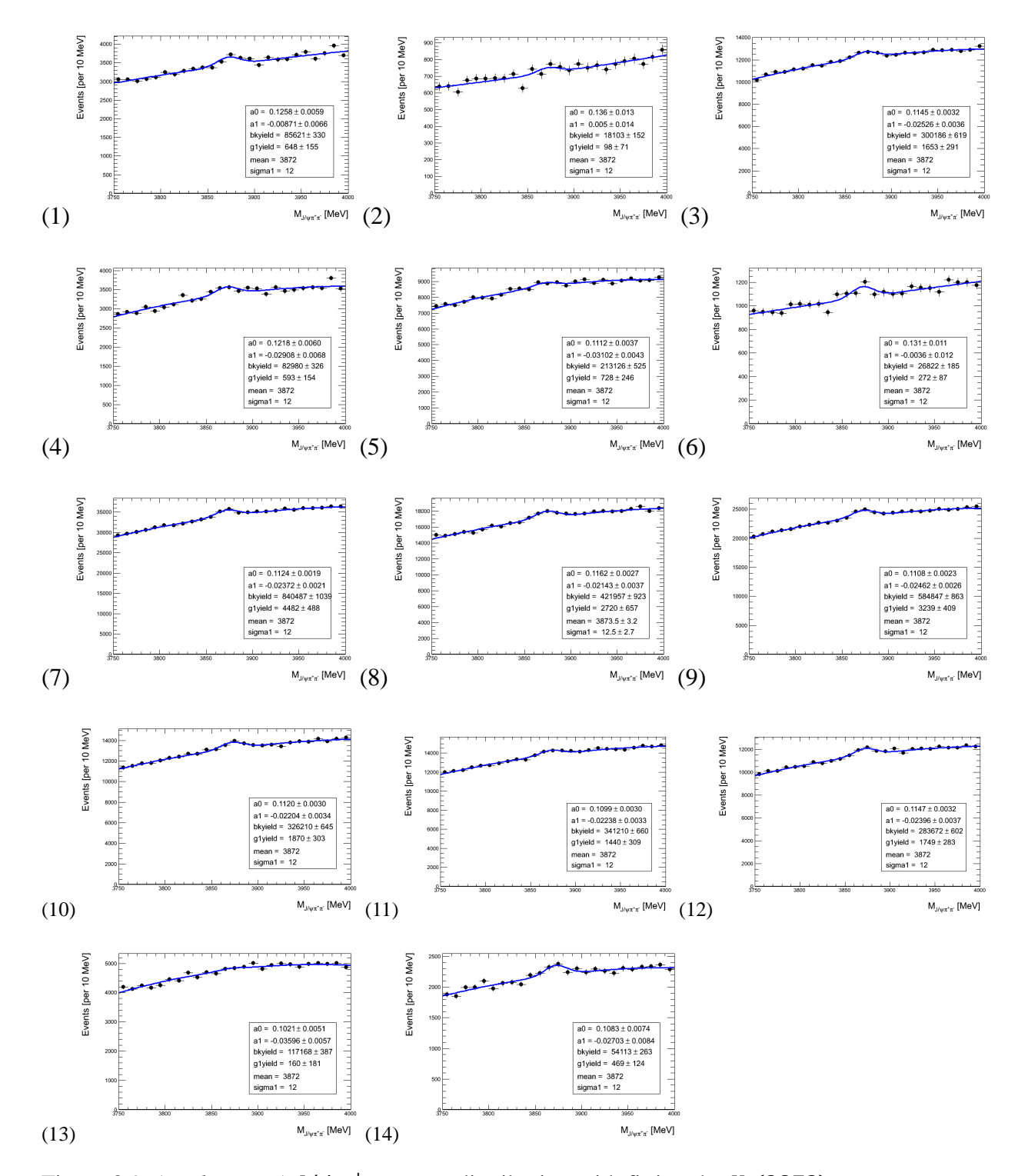


Figure 8.9. (*Preliminary*) $J/\psi \pi^+ \pi^-$ mass distribution with fitting the $X_c(3872)$ mass.

Table 8.9. (*Preliminary*) Data $X_c(3872)$ yields, by periods, obtained from fits to $J/\psi \pi^+\pi^-$ mass distributions.

| Period | (1) 2010 | (2) 2011 B2 | (3) 2011 D | (4) 2011 E | (5) 2011 F2 | (6) 2011 F3 | (7) 2011 G |
|--------------------------------|-----------------|----------------|----------------|-----------------|----------------|-----------------|---------------|
| $X_c(3872)$ Yield | 648 ± 155 | 98 ± 17 | 1653 ± 291 | 593 ± 154 | 728 ± 246 | 272 ± 87 | 4482 ± 488 |
| Luminosity (fb ⁻¹) | 0.040 | 0.013 | 0.176 | 0.050 | 0.131 | 0.018 | 0.551 |
| Yield / fb ⁻¹ | 16248 ± 3886 | 7734 ± 1341 | 9378 ± 1650 | 11914 ± 3094 | 5560 ± 1878 | 14863 ± 4754 | 8135 ± 885 |

| Period | (8) 2011 H | (9) 2011 I | (10) 2011 J | (11) | (12) | (13) | (14) |
|--------------------------------|-----------------|----------------|----------------|----------------|----------------|----------------|-----------------|
| | | | | 2011K1 | 2011K2 | 2011K3 | 2011K4 |
| $X_c(3872)$ Yield | 2720 ± 657 | 3239 ± 409 | 1870 ± 303 | 1440 ± 309 | 1749 ± 283 | 160 ± 181 | 469 ± 124 |
| Luminosity (fb ⁻¹) | 0.270 | 0.392 | 0.231 | 0.240 | 0.204 | 0.088 | 0.039 |
| Yield / fb ⁻¹ | 10063 ± 2430 | 8267 ± 1044 | 8110 ± 1314 | 6002 ± 1288 | 8590 ± 1389 | 1813 ± 2051 | 11897 ± 3145 |
| | | | | | | | |

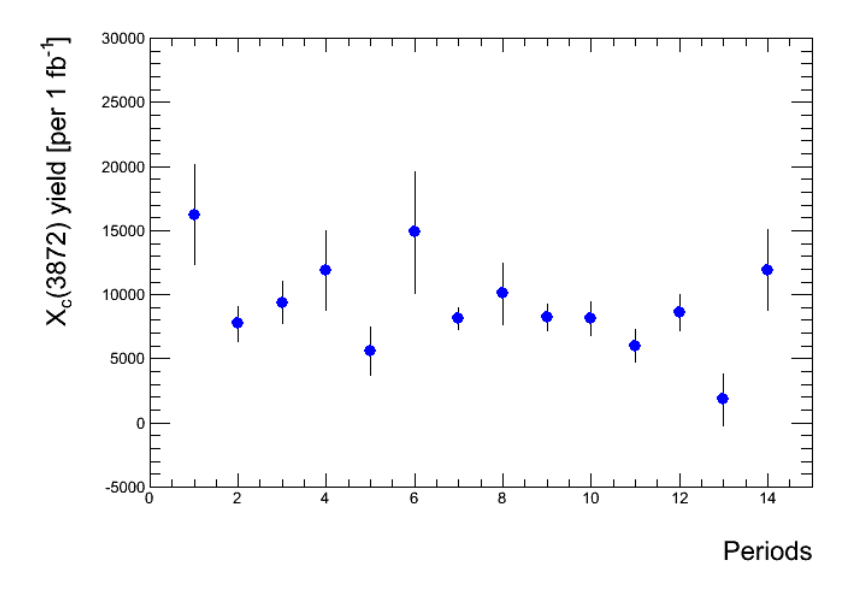


Figure 8.10. (*Preliminary*) Data $X_c(3872)$ yields per 1fb⁻¹ for each period.

CHAPTER 9

CONCLUSIONS AND OUTLOOK

9.1 Conclusions

Using pp collision data collected at $\sqrt{s}=7$ TeV in 2010 and 2011 with the ATLAS detector, corresponding to an integrated luminosity of 2.44 fb⁻¹, the $J/\psi\pi^+\pi^-$ combinations have been studied in the invariant mass range between 3,000.0 MeV/c² and 5,800.0 MeV/c². The selection criteria have been developed, the detection efficiency of the $X_c(3872)$ signal has been evaluated, and the systematic errors have been identified, some of which have been estimated. Both the $\psi(2S)$ and the $X_c(3872)$ signals are observed in the $J/\psi\pi^+\pi^-$ mass spectrum. The observation of the interaction $X_c(3872) \rightarrow J/\psi\pi^+\pi^-$ proves that the detection of the charmonium-like X, Y, Z states is feasible with the ATLAS detector at the LHC. The size of the $X_c(3872)$ signal is found to be 21,625 \pm 980 with a mass of 3872.1 \pm 0.6 (statistical error only) MeV/c² and an rms resolution of 11.9 \pm 1.4 (statistical error only) MeV/c².

Other than the $\psi(2S)$ and the $X_c(3872)$ signals, there is no evidence for any significant enhancement in the $J/\psi\pi^+\pi^-$ mass spectrum. This dissertation research establishes that ATLAS can detect $X_c(3872)$ like new particles in the $J/\psi\pi^+\pi^-$ final state, and with current data sample, no new states have been observed in this study.

The Monte Carlo $pp \to X_c(3872) + anything$ and $B^+ \to X_c(3872)K^+$ samples have been studied. With identical selection criteria, the offline reconstruction efficiency of the

 $pp \to X_c(3872) + anything$ sample is ~52.03 \pm 0.29 % (statistical), and that of the $B^+ \to X_c(3872)K^+$ sample is ~55.23 \pm 0.23 % (statistical). The difference in reconstruction efficiencies is ~3.2 % between the two samples. This difference is treated as a systematic error due to Monte Carlo models.

The systematic errors come from several sources. The Monte Carlo models, the fitting methods, the uncertainty on BR($J/\psi \to \mu^+\mu^-$), and the error in detection efficiencies, have been considered in the systematical error evaluation in this dissertation. Effects due to pileup associated with high LHC luminosity, variations in bunch crossings, the muon identification efficiency, the error on the luminosity, pion tracking, the edge effect of efficiency for X_c (3872) at $p_T \sim 10$ GeV/c, and the imperfections in the Monte Carlo simulation, are the possible sources of systematical errors not studied here. They should be determined later for the final journal paper.

9.2 Outlook

Figure 9.1 shows the LHC schedule assumption in the coming years. The plan of the LHC for 2012 is to produce proton-proton collisions at $\sqrt{s} = 8$ TeV, with a luminosity 6×10^{33} cm⁻²s⁻¹, a bunch spacing of 50 ns, and an integrated luminosity ~ 15-20 fb⁻¹ to be collected by the ATLAS detector. The LHC will shut down (Long Shutdown, LS1) in November 2012, for repairing and upgrading the detectors at LHC, till July 2014. It will leave a window for physics with the 2012 data in late 2012 to 2014. After LS1, the LHC will produce proton-proton collisions at $\sqrt{s} = 13$ -14 TeV, with a luminosity 1×10^{34} cm⁻²s⁻¹, a bunch spacing of 25 ns, and an integrated luminosity ~ 75-100 fb⁻¹ per experiment for the period from 2014 to 2017. The LS2

phase will take place in 2018, after which the LHC will produce full energy proton-proton collisions at $\sqrt{s} = 14$ TeV, with a luminosity 2×10^{34} cm⁻²s⁻¹, a bunch spacing of 25 ns, and an integrated luminosity ~ 350 fb⁻¹ per experiment. We expect the factor ratios of 6-8 (LS1), 30-40 (LS2), and 140 (LS3), respectively, of current statistics presented in this dissertation.

This dissertation research has demonstrated that the pp collision events at the LHC produce X-like events, and the X-like events can be detected. Any new Y, Z and other charmonium-like states may be consequently found and measured by the ATLAS detector, via the $J/\psi\pi^+\pi^-$ and other decay modes. The unprecedent $X_c(3872)$ and other charmonium-like states samples to be collected by the ATLAS will allow for details study of the X, Y, Z states.

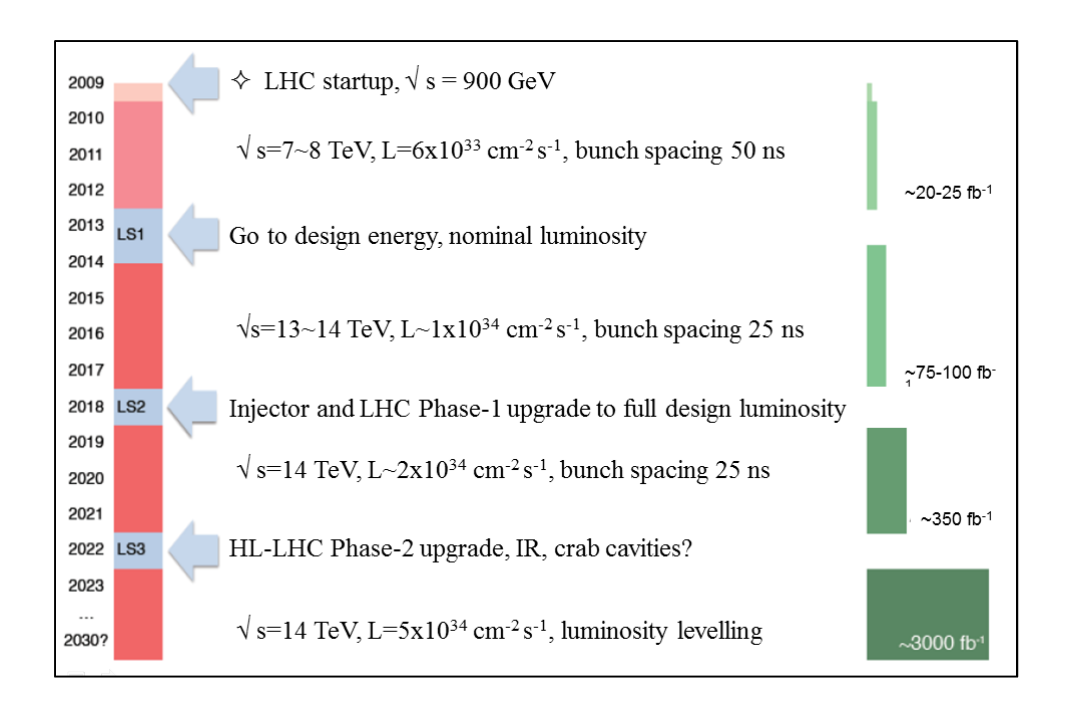


Figure 9.1. LHC Schedule Assumptions [46].

APPENDIX 1

PYTHIA JOB FILE FOR GENERATING $X_c(3872)$ EVENTS

```
# PRODUCTION SYSTEM FRAGMENT
    jobOptions for production of Xc(3872)-> J/psi pi+pi-,
#
                    J/psi -> mu+mu-
#
    using Psi(2S) for Xc(3872) production
#
#-----
# Private Application Configuration options
#-----
from AthenaCommon.AlgSequence import AlgSequence
topAlg = AlgSequence("TopAlg")
include ( "MC10JobOptions/MC10_Pythia_Common.py" )
from GeneratorFilters.GeneratorFiltersConf import BSignalFilter
topAlg += BSignalFilter()
# Xc(3872)-> J/psi pi+pi-, J/psi -> mu+mu-
Pythia.PythiaCommand += [
  "pysubs msel 0",  # turn OFF global process selection 
"pysubs msub 86 1",  # g+g -> J/psi+g turned ON
  "pyint2 kfpr 86 1 100443", # request Psi' instead of J/psi
  "pydat2 pmas 100443 1 3.872", # set Psi' mass to 3.872 GeV
  "pydat3 mdme 1567 1 0", # Psi' -> ee turned OFF
  "pydat3 mdme 1568 1 0", # Psi' -> mumu turned OFF
  "pydat3 mdme 1569 1 0", # Psi' -> random turned OFF
  "pydat3 mdme 1570 1 1",
                          # Psi' -> J/psi pi+pi- turned ON
  "pydat3 mdme 1571 1 0",
                          # Psi' -> J/psi pi0pi0 turned OFF
  "pydat3 mdme 1572 1 0",
                          # Psi' -> J/psi eta turned OFF
  "pydat3 mdme 1573 1 0",
                           # Psi' -> J/psi pi0 turned OFF
  "pydat3 mdme 1574 1 0",
                           # Psi' -> chi 0c gamma turned OFF
  "pydat3 mdme 1575 1 0",
                           # Psi' -> chi_1c gamma turned OFF
  "pydat3 mdme 1576 1 0",
                           # Psi' -> chi 2c gamma turned OFF
  "pydat3 mdme 1577 1 0",
                          # Psi' -> eta c gamma turned OFF
  "pydat3 mdme 858 1 0",
                          # J/psi -> ee turned OFF
  "pydat3 mdme 859 1 1".
                          # J/psi -> mumu turned ON
  "pydat3 mdme 860 1 0"
                          # J/psi -> random turned OFF
Pythia.PythiaCommand += [
```

```
"pysubs ckin 3 10.", # lower pT cut on hard process in 10 GeV
#----- Muon Trigger Cuts ------
BSignalFilter = topAlg.BSignalFilter
#----- Level 1 Muon Cuts -----
BSignalFilter.LVL1MuonCutOn = True
BSignalFilter.LVL1MuonCutPT = 4000.0
BSignalFilter.LVL1MuonCutEta = 2.5
#----- Level 2 lepton cuts -----
# These will only function if LVL1 trigger used.
BSignalFilter.LVL2MuonCutOn = True
BSignalFilter.LVL2MuonCutPT = 4000.0
BSignalFilter.LVL2MuonCutEta = 2.5
try:
  StreamEVGEN.RequireAlgs += ["BSignalFilter"]
except Exception, e:
  pass
from MC10JobOptions.PythiaEvgenConfig import evgenConfig
evgenConfig.efficiency = 0.1
#evgenConfig.minevents = 5000
# End of job options file
```

APPENDIX 2

PYTHIAB JOB FILE FOR GENERATING $B^+ \rightarrow X_c(3872)K^+$ EVENTS

```
jobOptions for production of B+ -> Xc(3872) K+,
#
          Xc -> J/psi pi+pi-, J/psi -> mu+mu-,
   overwriting psi' and using B+ -> psi' K+
#
# General Application Configuration options
from MC10JobOptions.PythiaBEvgenConfig import evgenConfig
#evgenConfig.minevents = 5000
#-----
# Private Application Configuration options
#-----
from AthenaCommon.AlgSequence import AlgSequence
topAlg = AlgSequence("TopAlg")
include ("MC10JobOptions/MC10 PythiaB Common.py")
     PARAMETERS SPECIFIC TO PYTHIAB
#-----
PythiaB.ForceCDecay = "no"
# overwrite channels and close antib
include( "MC10JobOptions/MC10_PythiaB_Bchannels.py" )
include( "MC10JobOptions/MC10 PythiaB CloseAntibQuarkNew.py" )
# ------ FORCE YOUR B CHANNEL HERE ------
#-----
#include( "MC10JobOptions/MC10 PythiaB CloseAntibQuark.py" )
PythiaB.ForceBDecay = "yes"
# B+ -> Xc(3872) K+, Xc -> J/psi pi+pi-, J/psi -> mu+mu-
#PythiaB.PythiaCommand += ["pydat3 mdme 932 1 1",
               "pydat3 kfdp 932 1 100443", # request Psi' instead of J/psi
PythiaB.PythiaCommand += ["pydat3 mdme 4651 1 1",
              "pydat2 pmas 100443 1 3.872", # set Psi(2S) mass to 3.872 GeV
              "pydat3 mdme 1567 1 0", # Psi' -> ee turned OFF
              "pydat3 mdme 1568 1 0", # Psi' -> mumu turned OFF
```

```
"pydat3 mdme 1569 1 0",
                                         # Psi' -> random turned OFF
                 "pydat3 mdme 1570 1 1",
                                         # Psi' -> J/psi pi+pi- turned ON
                 "pydat3 mdme 1571 1 0",
                                         # Psi' -> J/psi pi0pi0 turned OFF
                 "pydat3 mdme 1572 1 0",
                                         # Psi' -> J/psi eta turned OFF
                 "pydat3 mdme 1573 1 0",
                                         # Psi' -> J/psi pi0 turned OFF
                 "pydat3 mdme 1574 1 0",
                                         # Psi' -> chi_0c gamma turned OFF
                "pydat3 mdme 1575 1 0",
                                         # Psi' -> chi_1c gamma turned OFF
                 "pydat3 mdme 1576 1 0",
                                         # Psi' -> chi_2c gamma turned OFF
                 "pydat3 mdme 1577 1 0",
                                         # Psi' -> eta_c gamma turned OFF
                           "pydat3 mdme 858 1 0",
                           "pydat3 mdme 860 1 0"
                                                   1
# ------ PYTHIA PARAMETERS OPTIMAL FOR BEAUTY PRODUCTION --
# 'msel 5' is only for fast tests!
# for correct b-producion you should use 'msel 1'
# 'mstj 26 0' = no mixing was defined in Btune as default
# 'mstj 22 2' = no K0S, Lambda0 decays in Pythia - defined in Btune as default
include( "MC10JobOptions/MC10 PythiaB Btune.py" )
PythiaB.PythiaCommand += ["pysubs ckin 3 10.",
             "pysubs ckin 9 -3.5",
             "pysubs ckin 10 3.5",
             "pysubs ckin 11 -3.5",
             "pysubs ckin 12 3.5",
             "pysubs msel 1"]
# ----- DEFINE SELECTION CUTS ------
#-----
# ------ Selections on b quarks ------
# simulate only b-flavour events
PythiaB.flavour = 5.
# PythiaB force exclusive decay channels only on b=-5 side
# ------ b=5 --- and/or --- b=-5 -----
PythiaB.cutbq = ["0. 102.5 and 8. 2.5"]
# ------ LVL1 muon cuts 0=OFF 1=ON ------
PythiaB.lvl1cut = [1., 4., 2.5]
# ------ LVL2 muon/electron cuts 0=OFF 1=ON------
PythiaB.lvl2cut = [0., 13., 4., 2.5]
#PythiaB.lvl2cut = { 0., 11., 6., 2.5};
# ----- Offline cuts 0=OFF 1=ON ------
PythiaB.offcut = [1., 0.5, 2.5, 4., 2.5, 0.5, 2.5]
# ------ Number of repeated hadronization mhadr ------
PythiaB.mhadr = 1.
# End of job options file
```

APPENDIX 3

JOB OPTION CODE FOR ANALYZING $J/\psi \pi^+\pi^-$ EVENTS

Part 1

```
# BPhysAnalysisMasterAuto.py
# These are the master job options for running your analysis
# Include your own job options as shown below ensuring you
# do not overwrite things set here
# RUNS AUTOCONFIG - no need to set tags
from AthenaCommon.AthenaCommonFlags import athenaCommonFlags
athenaCommonFlags.FilesInput = [ "AOD.509237. 000001.pool.root.1" ]
#athenaCommonFlags.PoolInputQuery.set_Value_and_Lock("") # Needed for TAG jobs (as is)
from RecExConfig.RecFlags import rec
rec.doTrigger.set_Value_and_Lock(False) # leave false; nothing to do with trigger analysis
# include your algorithm job options here
rec.UserAlgs.set_Value_and_Lock("RunEarlyOnia.py")
# Output log setting; this is for the framework in general
# You may over-ride this in your job options for your algorithm
rec.OutputLevel.set Value and Lock(INFO);
# Write settings; keep all of these to false.
# Control the writing of your own n-tuple in the alg's job options
rec.doCBNT.set Value and Lock(False)
rec.doWriteAOD.set_Value_and_Lock (False)
rec.doWriteTAG.set Value and Lock (False)
rec.doHist.set Value and Lock (False)
# These 2 lines are needed for the AODFix mechanism
rec.readRDO=False
rec.doESD=False
# main jobOption - must always be included
#include("RecJobTransforms/UseOracle.py") # DB access
include ("RecExCommon/RecExCommon topOptions.py")
# Following 3 lines needed for TAG jobs (as is)
#svcMgr.EventSelector.RefName= "StreamAOD"
#svcMgr.EventSelector.CollectionType="ExplicitROOT"
```

```
#svcMgr.EventSelector.Query = ""

theApp.EvtMax = -1 # number of event to process

# Stops writing of monitoring ntuples (big files)
from PerfMonComps.PerfMonFlags import jobproperties as jp
jp.PerfMonFlags.doMonitoring = False
jp.PerfMonFlags.doFastMon = False
```

Part II

```
# -----
# RunEarlyOnia.py
# Good run selection mechanism
#-----
## Configure the goodrunslist selector tool
#from GoodRunsLists.GoodRunsListsConf import *
#ToolSvc += GoodRunsListSelectorTool()
#GoodRunsListSelectorTool.GoodRunsListVec = [ 'data11_7TeV.periodAllYear_DetStatus-v30-
pro09_CoolRunQuery-00-04-00_Muon.xml' ]
## This Athena job consists of algorithms that loop over events;
## here, the (default) top sequence is used:
from AthenaCommon.AlgSequence import AlgSequence, AthSequencer
job = AlgSequence()
job += AthSequencer("ModSequence1")
## GRL selector
#from GoodRunsListsUser.GoodRunsListsUserConf import *
#job.ModSequence1 += GRLTriggerSelectorAlg('GRLTriggerAlg1')
#job.ModSequence1.GRLTriggerAlg1.GoodRunsListArray = ['Muon']
#### NOTE - variable above MUST match name inside GRL xml file
# ESD or AOD
job.doESD = False
job.doAOD = False
from RecExConfig.InputFilePeeker import inputFileSummary
if 'EventStreamInfo#StreamESD' in inputFileSummary['metadata_itemsList']:
  print "Running on ESD"
  job.doESD = True
if 'EventStreamInfo#StreamAOD' in inputFileSummary['metadata_itemsList']:
  print "Running on AOD"
  job.doAOD = True
#-----
# MuonRoiWithExtendedBunches Alg:
```

```
# Settings for periods B,C,D with out-of-time triggers:
if iob.doESD:
  from TrigEffJpsiTools.TrigEffJpsiToolsConf import MuComm MuonRoiWithExtendedBunches
  ebc = MuComm MuonRoiWithExtendedBunches()
  ebc.OutputLevel = INFO#VERBOSE
  ebc.AllowedBCs = [-2, -1, 0]
                                                # specify the BCs to be used for matching
  ebc.L1PtNames = [ "MU0", "MU6", "MU10", "MU0_COMM", "MU15", "MU20" ]
  ebc.L1PtValues = [ 4000., 6000., 10000., 11000., 15000., 20000. ]
  ebc.Lvl1 RoiName = "LVL1 ROI extendedBCs"
  iob.ModSequence1 += ebc
#-----
# User analysis steering algorithm
from JpsiUpsilonTools.JpsiUpsilonToolsConf import JpsiAlg
from JpsiUpsilonAlgs.JpsiUpsilonAlgsConf import EarlyOnia
job.ModSequence1 += JpsiAlg('JpsiAlg')
job.ModSequence1 += EarlyOnia('EarlyOnia')
# GetTriggerObject tool:
#-----
from BPhysAnalysisTools.BPhysAnalysisToolsConf import BPhys GetTriggerObject
getTrigObj = BPhys__GetTriggerObject()
getTrigObj.OutputLevel = INFO
if job.doESD:
# Line below should be used for B,C,D
  getTrigObj.L1_trigObjs = [ "LVL1_ROI_extendedBCs" ]
  getTrigObj.L1_trigObjs = [ "LVL1_ROI" ]
else:
  getTrigObj.L1 trigObjs = [ "LVL1 ROI" ]
getTrigObj.L2_trigObjs = [ "L2_mu4", "L2_mu6", "L2_mu10", "L2_2mu4", "L2_2mu6", "L2_mu4_DiMu",
"L2_2mu4_DiMu", "L2_mu4_Jpsimumu", "L2_2mu4_Jpsimumu", "L2_mu4_Bmumu",
"L2 2mu4 Bmumu", "L2 mu6 DiMu", "L2 2mu6 DiMu", "L2 mu6 Jpsimumu", "L2 2mu6 Jpsimumu",
"L2 mu6 Bmumu", "L2 2mu6 Bmumu", "L2 MU4 DiMu FS noOS" ]
getTrigObj.EF_trigObjs = [ "EF_mu4", "EF_mu6", "EF_mu10", "EF_mu13", "EF_mu15", "EF_2mu4",
"EF_2mu6", "EF_mu4_DiMu", "EF_2mu4_DiMu", "EF_mu4_Jpsimumu", "EF_2mu4_Jpsimumu",
"EF_mu4_Bmumu", "EF_2mu4_Bmumu", "EF_mu6_DiMu", "EF_2mu6_DiMu", "EF_mu6_Jpsimumu",
"EF_2mu6_Jpsimumu", "EF_mu6_Bmumu", "EF_2mu6_Bmumu", "EF_mu4_MSonly_MB2_noL2_EFFS",
"EF mu4 MB2 noL2 EFFS", "EF MU4 DiMu FS noOS", "EF mu4 MSonly",
"EF_mu4_Upsimumu_FS", "EF_2mu4_Upsimumu", "EF_mu4_DiMu_FS", "EF_mu4_Jpsimumu_FS",
"EF_mu4_Trk_Jpsi", "EF_mu6_Trk_Jpsi"]
ToolSvc += aetTriaObi
print getTrigObj
# -----
# User's analysis requirements here:
# -----
# Configure inner detector tools and track selection settings
include("JpsiUpsilonTools/configureServices.py")
```

```
# Configure trigger decision tool - must be available if trigger is being used
include("trigger.py")
# Muon collection name - change once here
MuonCollectionName = "StacoMuonCollection"
# TrigEffJpsiTools
from TrigEffJpsiTools.TrigEffJpsiToolsConf import TrigEffJpsiTools
trigEffJpsiTools = TrigEffJpsiTools("TrigEffJpsiTools")
trigEffJpsiTools.OutputLevel = INFO
if iob.doESD:
# Line below should be uncommented for B,C,D
  trigEffJpsiTools.Lvl1 RoiName = "LVL1 ROI extendedBCs"
# trigEffJpsiTools.Lvl1 RoiName = "LVL1 ROI"
else:
  trigEffJpsiTools.Lvl1_RoiName = "LVL1_ROI"
trigEffJpsiTools.EndcapPivotPlaneMaximumRadius = 20000.
trigEffJpsiTools.BarrelPivotPlaneHalfLength = 16000.
trigEffJpsiTools.appendEFIfExists = True
trigEffJpsiTools.appendL2lfExists = True
trigEffJpsiTools.appendL1lfExists = True
#trigEffJpsiTools.useManualHypoCuts = False
ToolSvc += trigEffJpsiTools
print trigEffJpsiTools
#-----
# TGCcablingServerSvc
from MuonCablingServers.MuonCablingServersConf import TGCcablingServerSvc
ServiceMgr += TGCcablingServerSvc()
theApp.CreateSvc += [ "TGCcablingServerSvc" ]
ServiceMgr.TGCcablingServerSvc.Atlas=True
ServiceMgr.TGCcablingServerSvc.forcedUse=True
ServiceMgr.TGCcablingServerSvc.useMuonTGC_CablingSvc=True
from TGC CondCabling.TGC CondCablingConf import TGCCablingDbTool
ToolSvc += TGCCablingDbTool()
from IOVDbSvc.CondDB import conddb
conddb.addFolderSplitMC('TGC','/TGC/CABLING/MAP_SCHEMA','/TGC/CABLING/MAP_SCHEMA')
import MuonCnvExample.MuonCablingConfig
# Jpsi Finder
from JpsiUpsilonTools.JpsiUpsilonToolsConf import Analysis__JpsiFinder
ExampleJpsiFinder = Analysis__JpsiFinder(name
                                                              = "JpsiFinderName",
                         OutputLevel = INFO,
                         OutputLevel = INFO,
muAndMu = True,
muAndTrack = False,
TrackAndTrack = False,
assumeDiMuons = True, # True: uses PDG value
track1Mass = 105.66, # Ignored if above is True
track2Mass = 105.66,
thresholdPt = 0.0,
higherPt = 0.0,
                                                 = True, # True: uses PDG values
```

```
invMassUpper
                                             = 3800.0.
                       invMassLower
                                             = 2400.0,
                       collAngleTheta
                                            = 0.0.
                       collAnglePhi
                                           = 0.0.
                       Chi2Cut
                                          = 10000.
                       oppChargesOnly
                                              = True.
                       sameChargesOnly
                                               = False,
                       allChargeCombinations
                                                = False,
                       allMuons
                                          = True.
                       combOnly
                                           = False.
                       atLeastOneComb
                                              = False,
                       useCombinedMeasurement
                                                   = False.
                       muonCollectionKey
                                              = MuonCollectionName,
                       TrackParticleCollection = "TrackParticleCandidate",
                       V0VertexFitterTool
                                             = TrkV0Fitter.
                                                                  # V0 vertex fitter
                       useV0Fitter
                                                        # if False a TrkVertexFitterTool will be used
                                           = False.
                       TrkVertexFitterTool
                                             = TrkVKalVrtFitter,
                                                                   # VKalVrt vertex fitter
                       #TrkVertexFitterTool
                                               = InDetFullVxFitterTool, # Full Billoir vertex fitter
                                               = InDetFastVxFitterTool, # Fast Billoir vertex fitter
                       #TrkVertexFitterTool
                       TrackSelectorTool
                                              = InDetTrackSelectorTool,
                       ConversionFinderHelperTool = InDetConversionHelper,
                       VertexPointEstimator
                                              = VtxPointEstimator,
                       useMCPCuts
                                               = True)
ToolSvc += ExampleJpsiFinder
       ExampleJpsiFinder
job.ModSequence1.JpsiAlg.JpsiFinderName = ExampleJpsiFinder
job.ModSequence1.EarlyOnia.TrackSelectorTool = InDetTrackSelectorTool
job.ModSequence1.EarlyOnia.TrackCollection = "TrackParticleCandidate"
job.ModSeguence1.EarlyOnia.VertexCollection = "VxPrimaryCandidate"
job.ModSequence1.EarlyOnia.MuonCollection = MuonCollectionName
job.ModSequence1.EarlyOnia.UseTriggerDecision = True
job.ModSequence1.EarlyOnia.UseTruth = True
job.ModSequence1.EarlyOnia.JpsiCandidates = "JpsiCandidates"
job.ModSequence1.EarlyOnia.OutputFileName = "ntupleDXtruek120.root"
job.ModSequence1.EarlyOnia.TrackPtCut = 500.
job.ModSequence1.EarlyOnia.TrackPrCut = 2.5
job.ModSequence1.EarlyOnia.MuonMass = 105.66
job.ModSequence1.EarlyOnia.PionMass = 139.57
job.ModSequence1.EarlyOnia.KaonMass = 493.6
job.ModSequence1.EarlyOnia.JpsiPDGMass = 3096.916
job.ModSequence1.EarlyOnia.YJpsiMassUpperCut = 3216.916
iob.ModSequence1.EarlyOnia.YJpsiMassLowerCut = 2976.916
job.ModSequence1.EarlyOnia.YPDGMass = 3872.0
job.ModSequence1.EarlyOnia.YMassUpperCut = 5800.
job.ModSequence1.EarlyOnia.YMassLowerCut = 3000.
job.ModSequence1.EarlyOnia.SlimNTuple = False
```

Runtime settings

APPENDIX 4

THE ROOT MACRO OF FITTING $J/\psi \pi^+\pi^-$ MASS

```
#include <vector>
#ifndef __CINT_
#include "RooGlobalFunc.h"
#endif
#include "RooRealVar.h"
#include "RooDataSet.h"
#include "RooGaussian.h"
#include "RooPolynomial.h"
#include "RooAddPdf.h"
#include "RooFitResult.h"
#include "RooFFTConvPdf.h"
#include "TCanvas.h"
#include "RooPlot.h"
#include "TAxis.h"
#include "TH1.h"
using namespace RooFit;
//Reset ROOT and connect tree file
 gROOT->Reset();
 f = new TFile("ntuple.root");
 TTree *CollectionTree = (TTree*)gDirectory->Get("CollectionTree");
                 = new TH1F("hp2","", 100,3500.0, 4000.0); // Jpsi pipi mass
 hp2->GetXaxis()->SetTitle("J/#psi #pi#pi invariant mass (MeV/c^{2})");
 hp2->GetYaxis()->SetTitle("Events / 5 (MeV/c^{2})");
                 = new TH1F("hp8","", 100,3500.0, 4000.0); // Jpsi pipi mass
 hp8->GetXaxis()->SetTitle("J/#psi #pi#pi invariant mass (MeV/c^{2})");
 hp8->GetYaxis()->SetTitle("Events / 5 (MeV/c^{2})");
// hp8->SetFillColor(33);
 hp8->SetMarkerStyle(21);
// hp8->SetMarkerColor(kRed);
//Declaration of leaves types
 vector<double> *BsMass;
 vector<double> *BsJpsiMass;
 vector<double> *BsMassKfit;
```

```
vector<double> *SignalBsMass;
 // Set branch addresses.
 CollectionTree->SetBranchAddress("BsMass",&BsMass);
 CollectionTree->SetBranchAddress("BsJpsiMass",&BsJpsiMass);
 CollectionTree->SetBranchAddress("BsMassKfit",&BsMassKfit);
 CollectionTree->SetBranchAddress("SignalBsMass",&SignalBsMass);
 CollectionTree->SetBranchStatus("*",1); // enable all branches
// Double t jpsimass, jpsipt, lxy;
 Long t nbytes = 0:
 Long t nentries = CollectionTree->GetEntries();
 Int tnY, nYLast=0, nSignal, nSignal Last;
 double one_YMass, one_YMassFit, one_YJpsiMass, one_Dm;
 Long_t nYMassFit = 0;
 for (Long_t i=0; i<nentries; i++) {
  CollectionTree->GetEntry(i):
  nbytes += CollectionTree->GetEntry(i);
  nSignal_Last = nSignal; nSignal = SignalBsMass.size(); // number of reconstructed Yc signal Mass
  nYLast
             = nY;
                           = BsMassKfit.size(); // number of kinematic fitted Yc Mass
                     nΥ
  if (nSignal > 0) {
   for (Int_t kJpsi = 0; kJpsi < nSignal; kJpsi++) {
    one YMassFit = SignalBsMass.at(kJpsi);
    hp8->Fill(one_YMassFit);
    nYMassFit++;
   } // make histogram of reconstructed Yc signal Mass
  if (nY > 0) { // number of kinematic fitted Yc Mass
   for (Int_t inY = 0; inY < nY; inY++)
                    = BsMass.at(inY);
                                         // make histogram of Yc Mass
    one YMass
    one_YJpsiMass = BsJpsiMass.at(inY); // make histogram of YcJpsi Mass
    one_Dm
                   = one_YMass - one_YJpsiMass;
    if(one_YJpsiMass > 2970.4 && one_YJpsiMass < 3248.0){
        hp2->Fill(one_Dm+3097.6);
                                          // one_Dm + 3097.6 Mpdg(Jpsi)
   } //for loop
  } //nY
} // for(i) loop
 cout << "Total Number of YMassFit = " << nYMassFit << endl;
gStyle->SetOptStat(0000);
gStyle->SetOptFit(0000);
gStyle->SetLabelSize(0.03,"x");
gStyle->SetLabelSize(0.03,"y");
```

```
gStyle->SetCanvasColor(10);
// Declare variables x,mean,sigma with associated name, title, initial value and allowed range
 RooRealVar x("x","",3500,4000);
 RooRealVar mean("mean", "mean of 2 gaussians", 3872.0, 3852.0, 3892.0);
 RooRealVar sigma1("sigma1","width of gaussian1",20.0,0.0,25.0);
 RooGaussian gauss1("gauss1", "gaussian1 PDF", x, mean, sigma1);
 RooRealVar sigma2("sigma2","width of gaussian2",20.0,0.0,80.0);
 RooGaussian gauss2("gauss2", "gaussian2 PDF", x, mean, sigma2);
 RooRealVar g1frac("g1frac", "g1frac", 0., 1.);
 RooRealVar g2frac("g2frac", "g2frac", 0., 1.);
 // Construct px = 1 (flat in x)
 RooRealVar a0("a0","a0",0.0,0.0);
 RooPolynomial px("px","px",x,RooArgList(a0));
 RooAddPdf sum("sum", "sum", RooArgList(gauss1, gauss2, px), RooArgList(g1frac, g2frac));
 RooDataHist dh("dh", "dh", x, Import(*hp8));
//Fit model to data
 // -----
  // Fit gxlx to data
 sum.fitTo(dh);
// Plot data, gauss1 + gauss2 pdf
 RooPlot* xframe = x.frame();
 dh.plotOn(xframe);
 sum.plotOn(xframe);
 sum.paramOn(xframe,Layout(0.2,0.55,0.9));
 // Draw all frames on a canvas
 new TCanvas("RooFit 2 Gaussians", "RooFit 2 Gaussians");
 qPad->SetLeftMargin(0.15); xframe->GetYaxis()->SetTitleOffset(1.4); xframe->Draw();
 xframe->GetXaxis()->SetTitle("J/#psi #pi#pi invariant mass (MeV/c^{2})");
 xframe->GetYaxis()->SetTitle("Events / 5 (MeV/c^{2})");
// Show the chi^2 of the curve w.r.t. the histogram
// If multiple curves or datasets live in the frame you can specify
// the name of the relevant curve and/or dataset in chiSquare()
 cout << "chi^2 = " << xframe->chiSquare() << endl;
}
```

REFERENCES

- [1] David Griffiths, Introduction to Elementary Particles, Second, Revised Edition (WILEY-VCH, 2008)
- [2] Donald H. Perkins, Introduction to High Energy Physics, Forth Edition (CAMBRIDGE, 2000)
- [3] W. M. Yao et al. [Particle Data Group], J. Phys. G 33 (2006) 1 (http://pdg.lbl.gov/)
- [4] Bruce Yabsley, (Belle Collaboration) eprint arxiv:hep-ex/0507028v2 (2005) http://arxiv.org/abs/hep-ex/0507028
- [5] S.K Choi et al, (The Belle Collaboration) Phys. Rev. Lett. 91, 262001 (2003) http://prola.aps.org/abstract/PRL/v91/i26/e262001
- [6] The BABAR Collaboration, B. Aubert, et al, Phys.Rev.Lett.95:142001 (2005) http://arxiv.org/abs/hep-ex/0506081
- [7] L Maiani and A.D. Polosa, eprint arXiv0708 3997v1 [hep-ph], (2007) http://arxiv.org/abs/0708.3997
- [8] The CLEO collaboration, T E Coan et al, Phys. Rev. Lett. 96, 162003 (2006) http://arxiv.org/abs/hep-ex/0602034
- [9] The Belle Collaboration S. K. Choi et al, Phys. Rev. Lett. 100, 142001 (2008)
- [10] M. Kramer, "Quarkonium production at high-energy colliders," Prog. Part. Nucl. Phys. 47 (2001) 141 [arXiv:hep-ph/0106120] http://arxiv.org/abs/hep-ph/0106120
- [11] P. Braun-Munzinger, K. Redlich, et al. "Charmonium production from secondary collisions at LHC energy" (2000) http://www.springerlink.com/content/9f0hw2hullgka7ln/
- [12] K. Sridhar et al. "Charmonium Production at the LHC" eprint arxiv:hep-ex/9602329v1 (1996) http://arxiv.org/abs/hep-ph/9602329

- [13] T. Sjostrand, S. Mrenna and P. Skands, "PYTHIA 6.4: Physics and manual," JHEP 0605 (2006) 026 [arXiv:hep-ph/0603175].
- [14] ATLAS Collaboration, G. Aad et al., "Measurement of the differential cross-sections of inclusive, prompt and non-prompt J/ψ production in proton-proton collisions at $\sqrt{s}=7$ TeV," Nucl. Phys. B 850 (2011) 387-444 http://dx.doi.org/10.1016/j.nuclphysb.2011.05.015 http://arxiv.org/abs/1104.3038
- [15] LHCb Collaboration, R. Aaij et al., "Measurement of J/ψ production in pp collisions at \sqrt{s} = 7 TeV," Eur.Phys.J.C71 (2011) 1645 http://dx.doi.org/10.1140/epjc/s10052-011-1645-y http://arxiv.org/abs/1103.0423
- [16] LHCb Collaboration, R. Aaij et al., "Observation of X(3872) production in pp collisions at $\sqrt{s} = 7$ TeV" LHCb-PAPER-2011-034; CERN-PH-EP-2011-216 http://arxiv.org/abs/1112.5310
- [17] CMS Collaboration, D. Fasanella, "Observation of *X*(3872) state at CMS" CMS-CR-2011-258 http://cdsweb.cern.ch/record/1395469
- [18] L. Evans and P. Bryant, "LHC Machine," JINST 3 (2008) S08001
- [19] ATLAS Collaboration, "ATLAS: Detector and physics performance technical design report, Vol. I," CERN-LHCC-99-014, ATLAS-TDR-14, (1999)

 http://atlas.web.cern.ch/Atlas/GROUPS/PHYSICS/TDR/access.html
- [20] The ATLAS Collaboration, ATLAS Inner Detector Technical Design Report vol.1 CERN/LHCC/97-16, (1997)
- [21] ATLAS Collaboration, G. Aad et al., "The ATLAS Experiment at the CERN Large Hadron Collider," JINST 3 (2008) S08003

 https://twiki.cern.ch/twiki/pub/Atlas/AtlasTechnicalPaper/Published_version_jinst8_08_s08

 003.pdf
- [22] ATLAS Collaboration, "The Expected Performance of the ATLAS Inner Detector," [ATLCOM-PHYS-2008-105] and in "Expected Performance of the ATLAS Experiment Detector, Trigger and Physics," CERN-OPEN-2008-020, Geneva (2008) http://cdsweb.cern.ch/record/1125884
- [23] ATLAS Magnet System (http://atlas-bt.web.cern.ch/atlas-bt/)

- [24] ATLAS Central Solenoid TDR (http://atlas.kek.jp/solenoid/solenoid-TDR.html)
- [25] The ATLAS Calorimeter Community, ATLAS Liquid Argon Calorimeter Technical Design Report, ATLAS TDR-2 CERN/LHCC/96-41, (1996) http://atlas.web.cern.ch/Atlas/GROUPS/LIQARGON/Util/tdr.html
- [26] The ATLAS Calorimeter Community, ATLAS Tile Calorimeter Technical Design Report, ATLAS TDR-2 CERN/LHCC/96-42, (1996)
- [27] ATLAS Muon Spectrometer (https://twiki.cern.ch/twiki/bin/view/Atlas/MuonSpectrometer)
- [28] The ATLAS Muon Collaboration, ATLAS Muon Spectrometer Technical Design Report, ATLAS TDR-10 CERN/LHCC/97-22, (1997)
- [29] ATLAS Collaboration, "The ATLAS high-level trigger, data acquisition and controls: Technical design report," LHCC 2003-022, CERN, 2003
- [30] ATLAS Collaboration, "The ATLAS Level-1 Trigger: Technical Design Report," LHCC 1998-14, ATLAS-TDR-12, CERN, 1998
- [31] G. Duckeck et al. [ATLAS Collab.], "ATLAS computing: Technical design report," (Section 3.3), CERN-LHCC-2005-022 http://atlas-proj-computing-tdr.web.cern.ch/atlas-proj-computing-tdr/Html/Computing-TDR-21.htm#pgfId-1019542
- [32] The Athena Framework (https://twiki.cern.ch/twiki/bin/view/Atlas/AthenaFramework)
- [33] G. Duckeck et al. [ATLAS Collab.], "ATLAS computing: Technical design report," CERN-LHCC-2005-022
- [34] CASTOR (CERN Advanced STORage manager) (http://castor.web.cern.ch/castor/)
- [35] ATLAS Distributed Computing (https://twiki.cern.ch/twiki/bin/view/Atlas/AtlasDistributedComputing)
- [36] ATLAS Metadata Interface (AMI) (https://twiki.cern.ch/twiki/bin/view/Atlas/AtlasMetadataInterface)
- [37] The PanDA Production and Distributed Analysis System (https://twiki.cern.ch/twiki/bin/view/Atlas/PanDA)

- [38] P. Reznicek, "CDF vertex-fitting package in ATHENA," 2005

 http://atlas-sw.cern.ch/cgi-bin/viewcvs-atlas.cgi/offline/Reconstruction/Vertexing/CtvmftVertexFit/doc/CtvmftVertexFit.pdf?view=co

 =co
- [39] ATLAS Collaboration, "VKalVrt package for vertex reconstruction in ATLAS," ATL-PHYS-2003-031, CERN, 2003. http://cdsweb.cern.ch/record/685551
- [40] VkalVrt fitting package (https://twiki.cern.ch/twiki/bin/view/Atlas/VKalVrt)
- [41] Geant4 (http://geant4.web.cern.ch/geant4/)
- [42] ATLAS Good Run List Generator (https://atlasdqm.cern.ch/grl/)
- [43] ATLAS Luminosity Calculator (https://atlas-lumicalc.cern.ch/)
- [44] ATLAS Collaboration, G. Aad et al., "Measurement of the $\Upsilon(1S)$ Production Cross-Section in pp Collisions at $\sqrt{s} = 7$ TeV in ATLAS," Phys.Lett.B 705 (2011) 9-27 http://dx.doi.org/10.1016/j.physletb.2011.09.092 http://arxiv.org/abs/1106.5325
- [45] ATLAS Collaboration, Luminosity determination in pp collisions at $\sqrt{s} = 7$ TeV using the ATLAS detector at the LHC, Eur. Phys. J. C 71 (2011) 1630, doi:10.1140/epjc/s10052-011-1630-5, arXiv:1101.2185 [hep-ex]; ATLAS Collaboration, Updated luminosity determination in pp collisions at $\sqrt{s} = 7$ TeV using the ATLAS detector, ATLAS-CONF-2011-011, CERN, Geneva, Mar. 2011.
- [46] LHC Performance Workshop Chamonix 2012, LHC experiments upgrade and maintenance (https://indico.cern.ch/conferenceOtherViews.py?view=standard&confId=164089) CERN - Press Releases, "LHC to run at 4 TeV per beam in 2012" http://press.web.cern.ch/press/PressReleases/Releases2012/PR01.12E.html

VITA

Wei-Cheng Wong was born in Taipei, Taiwan. After completing his schoolwork at The Affiliated Senior High School of National Taiwan Normal University in Taipei in 1992, Wei-Cheng entered National Tsing Hua University in Hsinchu, Taiwan. During 1995 and 1997, he attended Fu-Jen Catholic University in Hsinchuang, Taiwan. He received a Bachelor of Science with a major in physics from Fu-Jen Catholic University in May 1997. He entered National Tsing Hua University in 1997, from which he received a Master of Science with a major in physics in May 2000. During the period 1997 - 2000, he did research in the Light Source Division of National Synchrotron Radiation Research Center in Hsinchu, Taiwan. After finishing the obligation of military service, he was employed as an engineer at Winbond Electronics Corporation in Hsinchu, Taiwan, from June 2002 to August 2004. He was then employed as a patent engineer at Top Team International Patent & Trademark Office in Taipei, Taiwan, from January 2005 to July 2005. In August 2005, he entered the graduate school at The University of Texas at Dallas.